**Application of Direction-based Techniques on Overlapping Nuclei Segmentation**

**Yunyong Surut**

**A Thesis Submitted in Partial Fulfillment of the Requirements for the Degree of Doctor of**

**Philosophy in Electrical Engineering**

**Prince of Songkla University**

**2014**

| | |
|---|---|
| **Thesis Title** | Application of Direction-based Techniques on Overlapping Nuclei Segmentation |
| **Author** | Mr. Yunyong Surut |
| **Major Program** | Doctor of Philosophy Program in Electrical Engineering |

**Major Advisor**

P. Phukpattaranont
..................................................

(Assoc. Prof. Dr. Pornchai Phukpattaranont)

**Examining Committee:**

Montri Karjanadecha .......................Chairperson

(Assoc. Prof. Dr. Montri Karnjanadecha)

P. Phukpattaranont
..................................................

(Assoc. Prof. Dr. Pornchai Phukpattaranont)

..................................................

(Dr. Somchai Limsiroratana)

..................................................

(Asst. Prof. Dr. Nikom Suvonvorn)

..................................................

(Dr. Chatchai Suppitaksakul)

The Graduate School, Prince of Songkla University, has approved this thesis as partial fulfillment of the requirements for the Doctor of Philosophy in Electrical Engineering

..................................................

(Assoc. Prof. Dr. Teerapol Srichana)

Dean of Graduate School

This is to certify that the work here submitted is the result of the candidate's own investigations. Due acknowledgement has been made of any assistance received.

.................... P. Phukpattaranont .................... Signature

(Assoc. Prof. Dr. Pornchai Phukpattaranont)

Major Advisor

.................................................... Signature

(Yunyong Surut)

Candidate

I hereby certify that this work has not been accepted in substance for any degree, and is not being currently submitted in candidature for any degree.

.............................................. Signature

(Yunyong Surut)

Candidate

**Thesis Title**      Application of Direction-based Techniques on Overlapping

Nuclei Segmentation

**Author**      Mr. Yunyong Surut

**Major Program**      Doctor of Philosophy Program in Electrical Engineering

**Academic Year**      2013

## ABSTRACT

Overlapping nuclei segmentation employs image information to extract boundaries or pixel group of individual nucleus. Shape, edge and intensity of nuclei are applied to image preprocessing to prepare required conditions for segmentation algorithms. Direction is the information that can yield the segmented objects when it holds the smoothing and contrasting direction abilities before direction-based segmentation. This work proposes technique consisting of two steps, direction generation and direction segmentation. The preprocessing named direction generator operates to construct direction from nuclei shape based on the desired direction abilities. Three direction segmentation techniques are proposed to determine the boundaries or pixel group. Direction-based splitting and merging technique (DSMT) exploits grouping and re-grouping the direction field based on smoothing direction ability. In contrast, direction-based classification technique (DBCT) uses the contrasting direction ability to locate the boundaries between overlapping nuclei. Finally, direction-based flow tracking technique (DBFT) moves pixels using path from direction information to the same area or nearby in each individual nucleus. The recovery of these pixels to the original position after label process results the individual nucleus. The performance to these techniques are compared to the tradition watershed (TWS) and marker-controlled watershed (MCWS) on overlapping nuclei images. On the classifier performance measurement, DBFT provides the highest number of ACC and $F_1$-measure. This shows that the direction-based techniques can achieve the segmentation task. Also, the proposed segmentation techniques operate on relation, difference, and path of direction field. They are the essential characteristics of these segmentation approaches.

**Thesis Title**     Application of Direction-based Techniques on Overlapping

Nuclei Segmentation

**Author**     Mr. Yunyong Surut

**Major Program**     Doctor of Philosophy Program in Electrical Engineering

**Academic Year**     2013

## ABSTRACT

Overlapping nuclei segmentation employs image information to extract boundaries or pixel group of individual nucleus. Shape, edge and intensity of nuclei are applied to image preprocessing to prepare required conditions for segmentation algorithms. Direction is the information that can yield the segmented objects when it holds the smoothing and contrasting direction abilities before direction-based segmentation. This work proposes technique consisting of two steps, direction generation and direction segmentation. The preprocessing named direction generator operates to construct direction from nuclei shape based on the desired direction abilities. Three direction segmentation techniques are proposed to determine the boundaries or pixel group. Direction-based splitting and merging technique (DSMT) exploits grouping and re-grouping the direction field based on smoothing direction ability. In contrast, direction-based classification technique (DBCT) uses the contrasting direction ability to locate the boundaries between overlapping nuclei. Finally, direction-based flow tracking technique (DBFT) moves pixels using path from direction information to the same area or nearby in each individual nucleus. The recovery of these pixels to the original position after label process results the individual nucleus. The performance to these techniques are compared to the tradition watershed (TWS) and marker-controlled watershed (MCWS) on overlapping nuclei images. On the classifier performance measurement, DBFT provides the highest number of ACC and $F_1$-measure. This shows that the direction-based techniques can achieve the segmentation task. Also, the proposed segmentation techniques operate on relation, difference, and path of direction field. They are the essential characteristics of these segmentation approaches.

**ACKNOWLEDGEMENT**

# CONTENT

# LIST OF TABLES

# LIST OF FIGURES

**LIST OF ABBREVIATIONS**

DSMT                  Direction-based splitting and merging technique

DBCT                  Direction-based classification technique

DBFT                  Direction-based flow tracking technique

TWS                   Tradition watershed

MCWS                  Marker-controlled watershed

TP                    True positive

FN                    False negative

FP                    False positive

TN                    True negative

SS                    Sensitivity

PPV                   Positive predictive value

ACC                   Accuracy

# Chapter 1

# Introduction

## 1.1 Image Characteristics

Immunohistochemistry is a technique used for detecting in situ a tissue antigen by a specific antibody. An antigen-antibody reaction is visualized by the color development of specific dye and can be seen by light microscope. The tissue antigen is presented at any part of the cell, i.e., cell membrane, cytoplasm or nucleus. Therefore, it is a useful technique to demonstrate the protein markers including cancer cell. Estrogen receptor (ER) and progesterone receptor (PR) are prognostic markers for breast cancer detected by this method. Evaluation of ER and PR positive cells are useful for hormonal therapy.

Figure 1.1 shows an example of stained cancer cell image from microscope with a magnification of 40x. This staining procedure is utilized to demonstrate the existing of estrogen or progesterone receptors in the breast cancer cells. In other words, stained cancer cells are classified into two categories according to their nucleus color contents, i.e. brown and blue. The brown color indi-
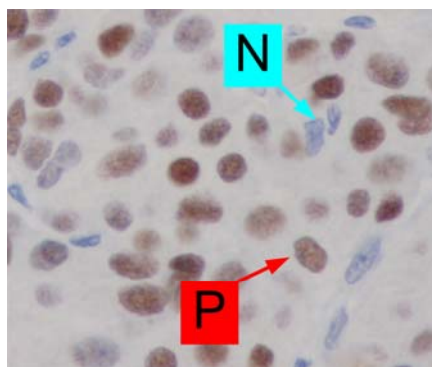
Fig. 1.1: An example of a stained cancer cell image. The brown and blue nuclei with the added labels are representative samples of positive and negative staining of estrogen receptor of breast cancer cells, respectively.

cates a positive (P) staining while the blue one demonstrates a negative (N) result. The brown and blue cells with the added labels shown in Figure 1.1 are representative samples of positive and negative staining of estrogen receptor of cancer cells, respectively. The ratio of the total number of positive cancer cells to the total number of cancer cells in the whole image is used by a doctor for medical planning and treatment.

Traditionally, the percentage of positive cells of those markers is semi-quantitatively counted. However, it is time consuming, costly, subjective and tedious. To overcome these problems, an automation of image analysis that previously requires manual operations is performed on the basis of the developments in computer capabilities and image processing algorithms [1]-[3]. There are a number of benefits that result from an automated analysis. These include an acceleration of the process, a reduction in cost for image analysis, as well as a decrement in a false inspection due to fatigue. Additionally, the automated analysis provides a quantitative description. Based on this quantitative measurement, the analysis result is objective. Further-more, the correlation of the quantitative categorization with patient symptoms may allow for an automated diagnostic system [4]. However, it is not expected that automated image analysis will replace pathologist's experience. It is only an aid to the pathologist for the repeated routine work and yields quantitative results that complement and enhance interpretations by pathologists. Visual examination by the pathologist is still required where the objects that the method is not trained to deal with are encountered.

## 1.2 Review of Literature

Literatures relating the overlapping nuclei segmentation can be categorized into intensity-based and direction-based algorithms. Based on intensity determination, the watershed algorithm is popular technique by its simple adaptation to various nuclei in hand. Such combination with the other components, these further improvements answer their requirement as well. To organize their proposed approaches clearly, pre-processing and post-processing can be used to represent the similarity among them. On the one hand, the pre-processing is the preparation of catchment basin that is before provided to flooding process of watershed algorithm. Under utilizing the binary

image nuclei from image preprocessing, the accurate catchment basin can be produced by marking function [5]. Based on the distance transformation applied to catchment basin preparation, its improvement by marking function [6] generates the contrast distance among overlapping nuclei. In addition, novel distance transformation is proposed as the reverse fuzzy distance transform [7] and radial symmetry decomposition technique [8]. These techniques alternatively propose distance transformation in more complexity process. In case of irregular nuclei surface, the harmonic cut and regularized centroid transform [9] reconstructs the nuclei surface yielding more smoothing catchment basin. Moreover, marker-controlled watershed which builds catchment basin by marker [6], [10]-[12] achieves the over segmentation reduction. Based on initial marker identification, this technique attempts to guarantee an extracted marker to represent an individual nucleus. Then, the obtained marker will be used to build the catchment basin provided to watershed algorithm later. On the other hand, the post-processing of watershed algorithm is subsequently action to handle the obtained undesired results as over-and-under segmentation. The decision function applied by selected features of segmented nuclei [12]-[14] determines merging decision among connected objects. In addition, the modified application of hole-filling, basically morphology operator, is proposed to support this task.

On the other side of intensity-based technique, there are the deformable contour methods which are classified into the direction-based technique. The combination of edge-and-region-based operations preferably makes precise segmentation line. Two families of medical application of this technique are snakes and level set methods [15]. They are firstly introduced by Kass et al. [16] and Malladi et al. [17] respectively. On overlapping nuclei segmentation, the implement-tations can be entirely adapted to all steps in process. In pre-processing step, preparing of external force field is the popular strategy, for instance, contrasting external force field among individual nucleus simply approaches the accurate contour [18]-[20]. Furthermore, the exact contour can be otherwise derived by the initial contour identification similar to marker in the watershed algorithm [21]. Next, in-processing of the deformable contour methods is also opened to accommodate to desired application. The modified process and parameterization are the example of this agreement to the specific case of overlapping nuclei [22]-[24]. For post-processing, in some deformable contour methods, their functions do not involve to overlapping object segmen-

Fig. 1.2: The elliptic-like shape (approximated by red line) of breast cancer nuclei.

tation. The extra operation is required to support this task such determination of knot's contour [25].

In spite of the mentioned techniques, other alternative approaches have been proposed continuously in various significant objectives. Adaptation, improvement, and modification are selected applying to achieve their goal. Such the neuron network theorem, it can be fully applied to overlapping nuclei segmentation [26]. Also, basically nuclei structure, the morphology calculation succeeds the segmentation task when the concave shape of overlapping nuclei is obviously observed [27]. Moreover, curve fitting technique, and gradient flow tracking also involve the various theorem on the overlapping nuclei segmentation [28]-[29]. Even though there are the continuous developments, the segmentation issue of overlapping nuclei is still opened. This absolutely indicates the significance of this topic impacting to knowledge application of digital image processing to biomedical engineering. Reversely, knowledge from this application might be also extended to the others.

## 1.3 Image Information from Overlapping Nuclei Image

Before the image analysis process, the consideration of image information is usually determined initially since it is essential value which influences to segmentation scheme. Similar to this work, overlapping nuclei segmentation, the individual nucleus will be initially analyzed and then selected the property and/or characteristic to prepare input to the direction application. This

TABLE 1.1: The conclusion of image information applied on overlapping nuclei segmentation.

| No. | Image information | Segmentation approaches | References |
|-----|-------------------|-------------------------|------------|
| 1 | Nuclei shape | Watershed | [5]-[8], [10]-[14], [30]-[31] |
| 2 | Nuclei shape | Deformable contour methods | [21] |
| 3 | Nuclei edge | Deformable contour methods | [18]-[19], [20], [22], [25] |
| 4 | Nuclei intensity | Watershed | [9] |
| 5 | Nuclei intensity | Gradient flow tracking | [29] |

requirement is called "image information". From the fact that the nuclei are usually elliptic-like shape [28], for instance, breast cancer nuclei as shown in Fig. 1.2. Most researchers in this filed give the priority to nuclei shape as the summary of the approaches shown in Table 2.1. This shows the majority in nuclei shape information applied to segmentation approach while following by nuclei intensity and nuclei edge is less employment. Clearly, the mentioned items are further described as following:

**Nuclei shape:** Since the nuclei can be described as elliptic-like shape, its description prefers the morphological image operator. For instance, the distance transformation is performed to prepare the nuclei intensity for watershed algorithm as shown in Fig. 1.3. It shows that the transformation generates the separated minimum of overlapping nuclei using the concave shape.

**Nuclei edge:** There is the image edge application which corresponds to the segmentation algorithm. As deformable contour methods, this manner generally exploits this information but the complex solution of overlapping nuclei problem is also required extremely.

**Nuclei intensity:** Because it is primary image information, the image noise from nuclei image acquisition and nucleus type usually reduce image quality, for example, the breast cancer nuclei
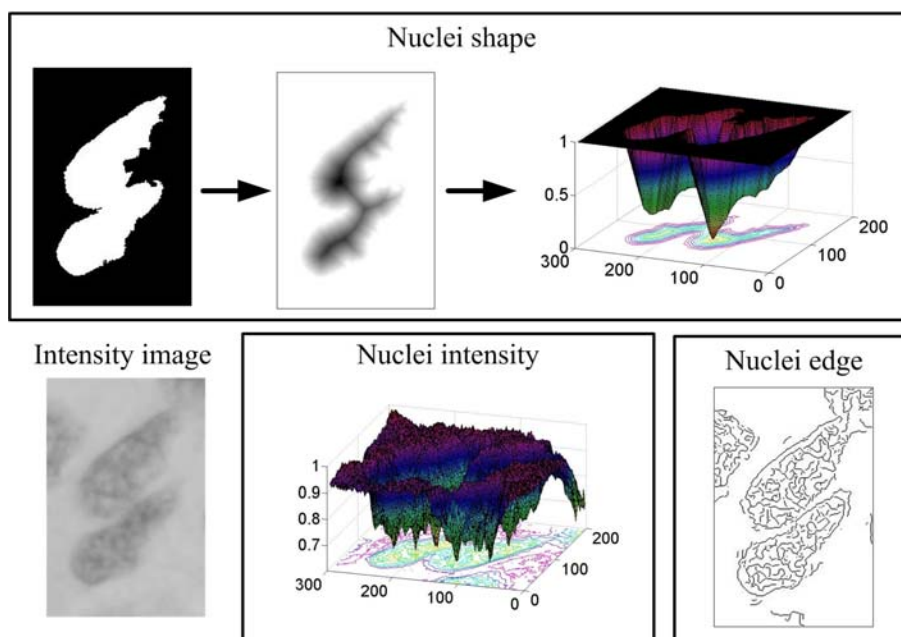
Fig. 1.3: The example of the application of image information on the overlapping nuclei

image.

illustrated as surface plot in Fig. 1.3. To hold its employment, the image preprocessing must be performed hardly when the image noise disturbs strongly.

From the image information implementation, the nuclei shape is mostly employed, especially applying to the distance transformation. The concave shape strongly yields advantage by more smoothed nuclei surface, maintaining the separated minimum, adaptation, and simple implementation. Thus, on the overlapping nuclei task, the most application on it in the initial information is represented obviously.

## 1.4 Original Contribution

From the literatures, the segmentation approaches require image information to build prepared information before segmentation. For instance, the specific pre-processing of watershed algorithm and deformable contour methods build catchment basin and external force field respectively. Also, the in-processing of deformable contour methods can be made parameter adjustments to

achieve this task. Moreover, the post-processing of them also determines the segmented nuclei to more correct result. However, these schemes have a trade-off on complexity, cost, and processing time. Thus, this work attempts to employ the alternative image information to maintain accuracy with less complexity, cost, and processing time.

## 1.5 Objective

(1) To propose novel algorithm of overlapping nuclei segmentation for breast cancer nuclei.

(2) To study and assess the proposed algorithm comparing to the existed algorithm in overlapping nuclei segmentation.

(3) To study factors affecting to overlapping nuclei segmentation for breast cancer nuclei.

# Chapter 2

# Overview of Direction-based Application

# on Overlapping Nuclei Segmentation

## 2.1 Introduction

In this chapter, the contents present the introduction of principle in direction-based application on overlapping nuclei segmentation. First, the Section 2.2 carries out the description of direction information in the traditional physics involved mathematics and the characteristics when it is on the 2D space. Furthermore, this section will also illustrate its possibility on segmentation task in 2D space. Consequently, in Section 2.3, the segmentation approach based on direction application will be deal with the image information from nuclei. This yields the general scheme in Section 2.4 which is based to other proposed approaches in this dissertation. Finally, the discussion to all obtained outcome will be expressed in Section 2.5 involved the relationship to next Chapter.

## 2.2 Direction Information

In applied mathematics and physics, the direction information is usually included to quantities formed as vector. Velocity, force, movement, and acceleration, for instance, are some examples which can be described its characteristic by a vector [32]. Based on its principle, the arrow direction of a vector represents its action where its length indicates the magnitude in selected scale. Let $\overline{AB}$ showed in Fig. 2.1(a) represents the vector, where the line from point $A$ to point $B$ is the line of action, and the point $B$ is the terminus of the vector. To accommodate the vector format, this dissertation uses the notation to denote a vector as $\mathbf{a}$ showed in Fig. 2.1(a). Furthermore, where $\mathbf{a}$ is only represented to direction information, the normalized vector is used to transform by
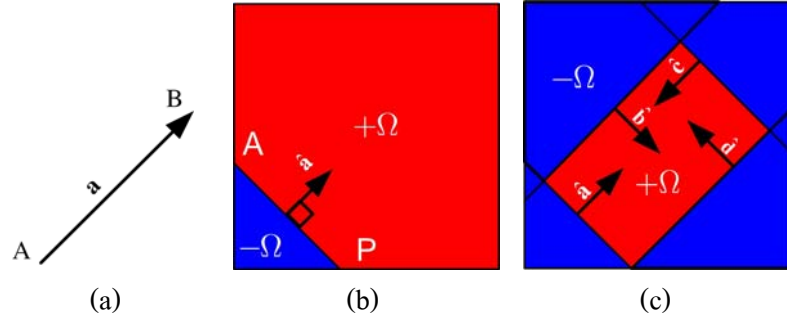
Fig. 2.1: Vector (a) and unit vector in 2D space (b)-(c).

$$\hat{\mathbf{a}} = \frac{\mathbf{a}}{\|\mathbf{a}\|}, \tag{2.1}$$

where $\|\mathbf{a}\|$ is norm of $\mathbf{a}$. $\hat{\mathbf{a}}$ is the unit vector that set the magnitude to one. In other words, the direction of $\hat{\mathbf{a}}$ is transformed to the rectangular coordinate that can be estimated the direction difference.

In 2D space, the existed $\hat{\mathbf{a}}$ can describe the segmented area by the definition of decision function $\left(D(\;)\right)$ which inputs the direction information of $\hat{\mathbf{a}}$. For instance, the $\hat{\mathbf{a}}$ in Fig. 2.1(b) can be extracted the decision line for segmented area by

$$D(\hat{\mathbf{a}}) = \begin{cases} +\Omega, & \angle\left(\overline{AP},\hat{\mathbf{a}}\right) \le \phi \\ -\Omega, & \angle\left(\overline{AP},\hat{\mathbf{a}}\right) > \phi \end{cases}, \tag{2.2}$$

where $\pm\Omega$ is the segmented area, $p$ is a point in 2D space, and $\phi$ is the reference angle that classifies the angle difference from $\angle\left(\overline{AP},\hat{\mathbf{a}}\right)$ to $\pm\Omega$. In the example, identifying $\phi$ to $90°$ sets the segmented area represented by the red and blue area for $+\Omega$ and $-\Omega$, respectively. In addition, the decision line can be varied by the difference $\phi$. Here, it is the result from a vector only which can make more information in 2D space. Definitely, increasing unit vector to 2D space yields more complete segmented area. As showing in Fig. 2.1(c), $\pm\Omega$ are restricted over only one vector. The cooperation of $\hat{\mathbf{a}}$, $\hat{\mathbf{b}}$, $\hat{\mathbf{c}}$, and $\hat{\mathbf{d}}$ is based on the intersection of $+\Omega$ of them. This shows direction information advantage to segmentation in 2D space. The operation of
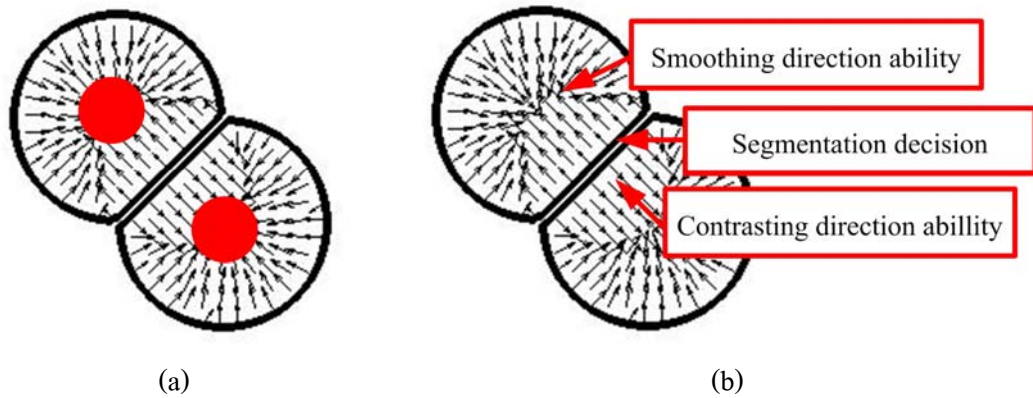
Fig. 2.2: Direction behaviors on overlapping nuclei.

direction and $D(\ )$ as the simple demonstration in Fig. 2.1(c) indicates to possibility of segmentation estimation in 2D space. In this dissertation, its application to overlapping nuclei segmentation is used to make value in practice. The correspondence of direction information and image segmentation is represented latter section which image information meets direction information.

## 2.3 Proposed Direction Form on Overlapping Nuclei Segmentation

In previous works, there are deformable contour methods and gradient flow tracking which utilized the direction application. They apply the direction to extract the segmentation line to separate the overlapping nuclei. Similar to intensity-based segmentation, the characteristic of application can be observed. Let synthesized-separated-nuclei image in Fig. 2.2 is determined the direction using $\nabla\left[f(i,j)\right]$ where $f(i,j)$ is its distance transformation. This shows direction behavior when the red mark is put on. Obviously, all direction in the individual nucleus tries to direct to the same area or same red mark. This behavior can be analyzed to ability of direction when the direction among them is considered.

**Smoothing direction ability:** This ability indicates that all direction in the individual nucleus tries to direct to the same area or nearby. This factor plays as the unity indication to all pixels in
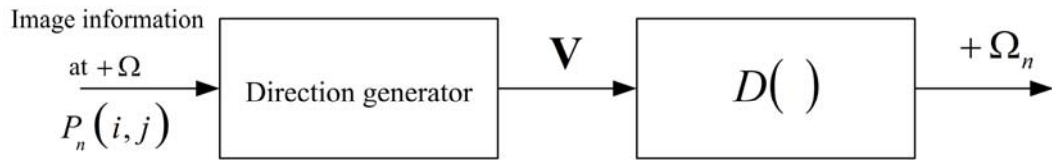
Fig. 2.3: Basic concept of direction application on image segmentation.

the individual nucleus. In other words, smoothing direction is the movement guideline that gathers them together.

**Contrasting direction ability:** From the smoothing direction ability, the further behavior occurs when the direction among the connected nuclei areas are determined. It is contrasting direction ability which separates the overlapping nuclei on the direction environment.

**Segmentation decision:** Co-operation of the smoothing and contrasting direction abilities originate the boundaries which prevent the connected nuclei, namely segmentation decision. This is the result of the decision function $(D(\ ))$ which is respectively judged $+\Omega_n$.

From the above description, the direction application on overlapping nuclei segmentation should be earned the smoothing and contrasting direction abilities for direction generator. These abilities make the direction field responding to decision function as well because its behavior has the unity in the individual nuclei. In addition, the decision function determining the segmentation boundary must perform based on two abilities employment.

## 2.4 General Scheme of Direction Application on Overlapping Nuclei Segmentation

This section describes the implementation of image information to overlapping nuclei segmentation based on direction determination. This basic process uses the nuclei shape as the
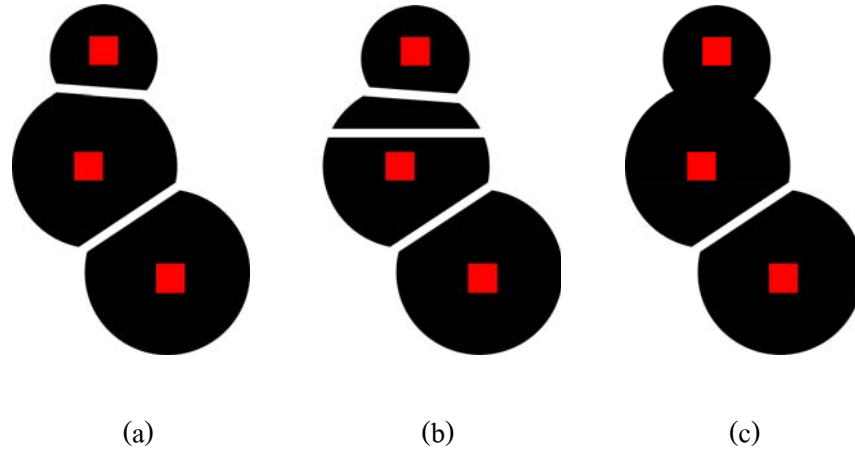
Fig. 2.4: (a) Correct segmentation. (b) Over segmentation. (c) Under segmentation.

image information, which is used to provide to direction application process. Therefore, the general scheme in this section will be the master process that is based to other chapters.

On the image information, discrete signal is formed by spatial coordinate. Let $P(i, j)$ represents pixel position which contains the image information such as intensity, color space value, etc. Assuming, at a $P(i, j)$, the image information at $+\Omega$ is inputted initially to the workflow as shown in Fig. 2.3 to perform the direction generator, where $+\Omega$ is foreground that includes the overlapping objects. At the output of direction generator, the image information is transformed to the vector matrix $\mathbf{V}$ where the magnitude of $\mathbf{V}$ at $P(i, j)$ illustrates its direction by vertical and horizontal values. In this concept, the direction generator is required to build some characteristic that can reveal its unity in the individual object. For example, all direction in it totally directs to the same area or nearby. Next, the direction in $\mathbf{V}$ is classified to $+\Omega_n$ where $+\Omega_n$ is the individual object area at object number $n$. This manner is called decision function $\left(D(\ )\right)$ because of its operation on classifier. From this, the target object is extracted its pixels in the image and also $n^{th}$. Thus, $+\Omega_n$ is an extracted object which is visualized by labeling number $n$ on the image. Finally, the $+\Omega_n$ will be compared to the expert marker to determine the segmentation accuracy as shown in Fig. 2.4. From the example, the correct segmentation is $+\Omega_n$ labeled with one marker (red dot). The over segmentation is $+\Omega_n$ which does not have the marker. The under segmentation is $+\Omega_n$ which contains more than one marker.

## 2.5 Discussion

This chapter proposes the overview of direction-based segmentation approach applied to overlapping nuclei segmentation problem. The contents flow subsequently from the basic theory to application. They consist of direction mathematics, applying the direction to segmentation approach in 2D space, the image information from overlapping nuclei image, and the overlapping nuclei segmentation using direction information. However, because this is only the overview and basic concept, the description does not illustrate the scheme, experiment, and result. These will be responded by later chapters which are a part of the basic workflow in Fig. 2.3. Hence, the proposed computations in this dissertation are in the two steps as direction generator and decision function $\left(D\left(\ \right)\right)$. Also, the obtained results will be $\mathbf{V}$ and $+\Omega_n$ respectively.

# Chapter 3

# Direction Generator

## 3.1 Introduction

The primary step to direction application on overlapping nuclei segmentation is the direction preparing as the direction generator shown in general workflow in Chapter 2. The provided information to this approach is required based on the selected image information from the overlapping nuclei image. From Chapter 2, when it responds by the nuclei shape, this is further calculated to obtain this information. The image pre-processing in Section 3.2 is set to achieve this task. It contains the minor steps formed as workflow which extracts the nuclei shape from nuclei color image. Subsequently, the obtained nuclei shape will be provided to the direction generator in Section 3.3. Now, the nuclei shape information is transformed to the direction field. The derived results from the experiment are reported in Section 3.4. These show the characteristic of the obtained direction field and parameter response, which are discussed in this section. Finally, the conclusions are given in Section 3.5.

## 3.2 Image Pre-processing on Overlapping Nuclei Segmentation

The image pre-processing step consists of image transformation and background elimination. This scheme prepares the image information extracted from the overlapping nuclei image. In overlapping nuclei segmentation, the image information is set to nuclei shape which is outstanding among the other image information as described in Section 2.2. Fig. 3.1 shows the workflow of all steps that takes initially the original source as color image to the end of process by the determined binary image. In each step, the operation is detailed as following:

**Color space transformation:** Because the various image data can be transformed among color image type, the application can select one that approaches the objective best. In this case, the
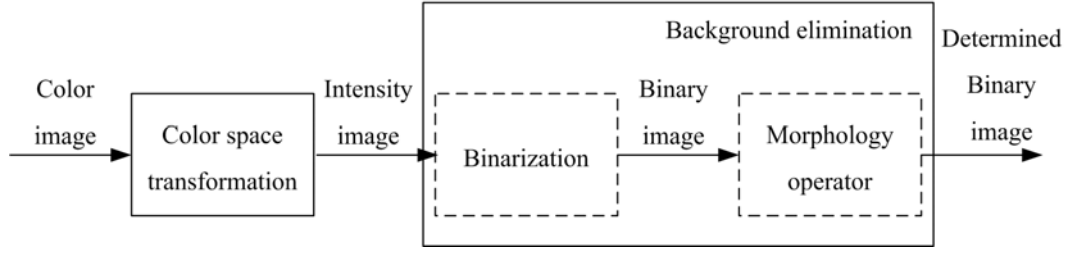
Fig. 3.1: Image pre-processing workflow.

intensity image is selected because it yields the contrasting between foreground referred to $+\Omega$ and background referred to $-\Omega$ as the example in Fig. 3.2(a).

**Binarization:** To prepare nuclei shape information, the binary image is the popular form in which the overlapping-and-individual nuclei appear exactly as the concave shape and elliptic-like shape respectively. The binarization is performed by the classification of a pixel to $\pm\Omega$. By the threshold value ($TH$), the binarization is calculated by

$$B(i,j) = \begin{cases} +\Omega & , I(i,j) \le TH \\ -\Omega & , I(i,j) > TH \end{cases}, \tag{3.1}$$

where $I(i,j)$ is the intensity value at $P(i,j)$. From high contrasting of the nuclei image intensity, it also yields the contrasting of the intensity histogram as shown in Fig 3.2(b). From this, the Otsu's thresholding performs well when the histogram acts as the two valleys. Moreover, the simplification and cost are also derived from this approach. Its threshold value can be calculated by

$$\sigma_B^2(TH^*) = \max_{1 \le TH < L} \sigma_B^2(TH), \tag{3.2}$$

where, the threshold value is $TH$ giving the maximum-between-class variance ($\sigma_B^2$). In the example, the obtained binary image still has some un-designed nuclei area. The morphology operator is needed to manage it.

(a)

(b)

(c)
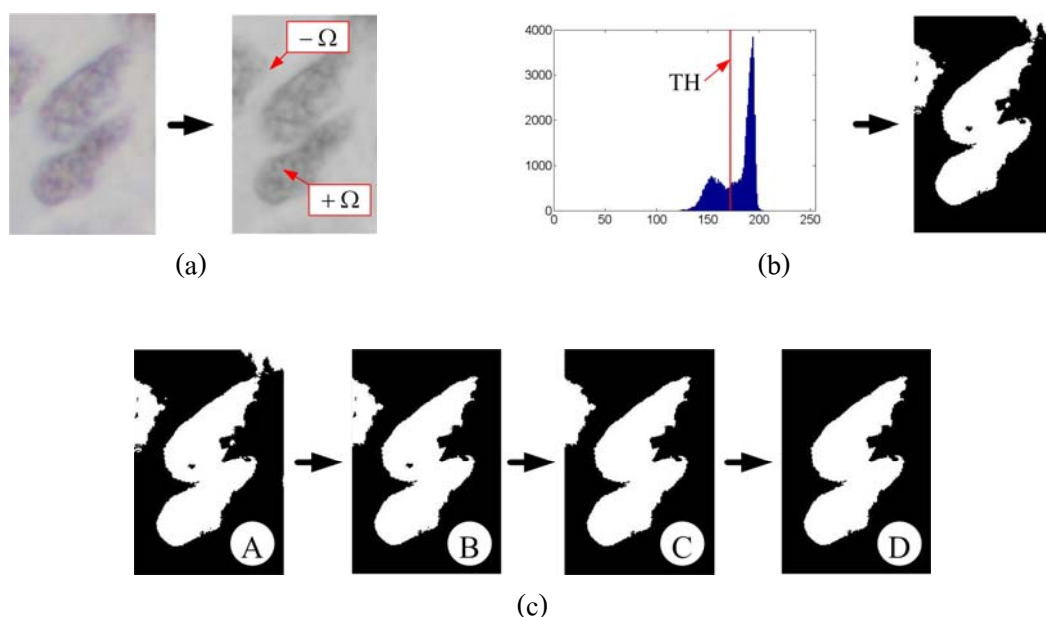
Fig. 3.2: (a) Color space transformation. (b) Binarization. (c) Morphology operator.

**Morphology operator:** Fig. 3.2(c) illustrates respectively results of selected morphology operator supporting each requirement. Firstly, the binary image (A) is determined the area (pixel number) that excludes the tiny piece, showing in the binary image (B). Then, the un-completed area by hole is filled as showed in the binary image (C). Finally, the un-completed area by attaching the image window is also released as showed in the binary image (D).

Note that the binarization and the morphology operator are considered to be the component of the background elimination from the foreground extraction. Here, the prepared image information by nuclei shape through the binary image is achieved. Thus, desired image information and the image in hand should be initially considered in the scheme construction.

## 3.3 Direction Generator

The direction generator is a step which builds the direction in the foreground $(+\Omega)$ of the overlapping nuclei image. It engages to response the requirement of direction application on overlapping nuclei segmentation. The accomplishment on smoothing-and-contrasting direction abilities is needed significantly when the image information on nuclei shape is selected. From
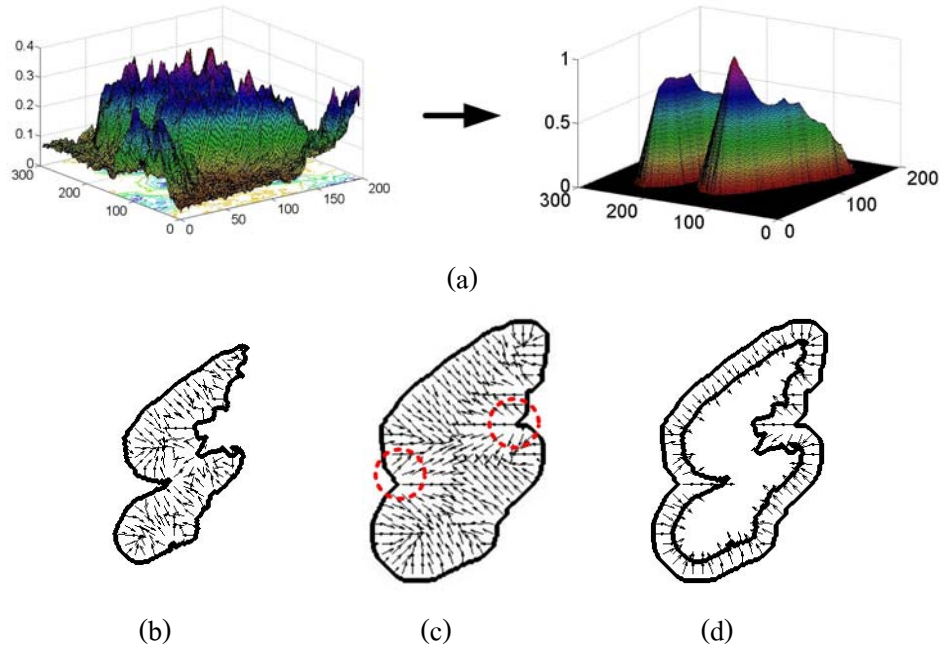
Fig. 3.3: (a) Smoothed image surface of reconstructed intensity after distance transformation. (b) The $\mathbf{V}$ of (a). (c) The $\mathbf{V}$ of dilated nuclei image. (d) $\mathbf{V}_{local}$.

previous works, the nuclei shape generally applies to $d(B)$, where $d(\ )$ is distance transformation function and $B$ is a binary image. It yields reconstructed intensity value which is more smoothing surface by the nuclei shape information. The demonstration is illustrated in Fig. 3.3. However, the irregular shape of overlapping nuclei makes roughly the reconstructed intensity. It respectively makes the error such the over-segmentation in watershed application.

To solve this problem and hold direction requirement, let the primary step to generate the initial direction by

$$\mathbf{V} = \frac{\nabla(d(B))}{\|\nabla(d(B))\|}, \tag{3.3}$$

where $\nabla$ is the image gradient estimation. The obtained direction field ($\mathbf{V}$) is illustrated in Fig. 3.3(b). There is confusing direction generated from local minima intensity by distance transformation of the irregular shape. Also, it misses the direction requirement and remains the
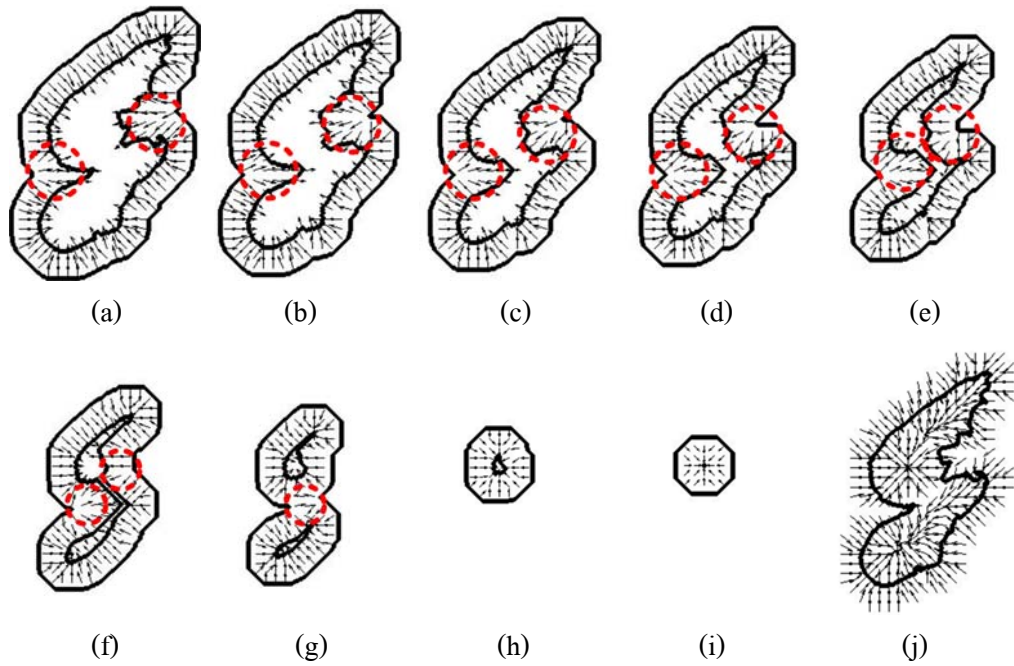
Fig. 3.4: (a)-(i) illustrate the local direction field at $iter$ = 1, 5, 10, 15, 20, 25, 30, 35, 40, and the final direction field (j).

problem. Thus, the direction field in hand is analyzed using observation of direction field structure. It reveals two points concerning the solution.

First, the irregular shape should be reduced before distance transformation. Fig. 3.3(c) shows the dilation operator, basic morphology operator, which sets the nuclei shape to more smoothness and then **V** is computed. The smoothing direction ability is more over the first distinctly but the contrasting direction ability is still lost. However, some potential remains for able observation. This is shown by the red dash circles in Fig. 3.3(c). The contrasting direction is at the concave shape of overlapping area. To utilize it, the second solution must take this direction along the segmentation boundary. This task can be achieved by the local distance transformation.

From the designed solution above, the direction generator will be combined by the morphology operator and the local distance transformation. By this, Eq. 3.3 for global estimation is transformed to

$$\mathbf{V}_{local} = \frac{\nabla \left( d \left( B \oplus E_d \right) \right)}{\left\| \nabla \left( d \left( B \oplus E_d \right) \right) \right\|} \cdot \overline{B},$$ (3.4)

where $E_d$ is a structure element for dilation operator, and $\dfrac{\nabla \left( d \left( B \oplus E_d \right) \right)}{\left\| \nabla \left( d \left( B \oplus E_d \right) \right) \right\|}$ the initial direction field from dilation operator. From Eq. 3.4, the improved direction field is illustrated in Fig. 3.3(d). To take the contrasting direction covering the segmentation boundary, the shrinking process by erosion operator is selected to perform in an iterated process, which is given by: [33]

**Direction generator:**

**Define** $E_d$ , $E_{sh}$

$\mathbf{V} = 0$

$iter = 0$

**While** $B$ **is not empty**

      **Find** $\mathbf{V}_{local}^{iter}$

      $\mathbf{V} = \left( \mathbf{V} + \mathbf{V}_{local}^{iter} \right) / 2$

      $B = B \ominus E_{sh}$

      $iter = iter + 1$

**End while**

**End**

where $V_{local}^{iter}$ is a local direction field at loop $iter$ , and $E_{sh}$ is the structuring element of erosion operator in the shrinking process. At a loop $iter$ , the direction generator yields $\mathbf{V}_{local}$ as shown in Fig. 3.4(a)-(i). The contrasting direction presented by the red dash circle attaches to the $\mathbf{V}_{local}$ as possible. Finally, in Fig. 3.4(j), the average of all $\mathbf{V}_{local}$ produces the desired direction field which keeps the smoothing-and-contrasting direction abilities.

## 3.4 Experimental Results

This section shows the results from the experiment where the actual overlapping nuclei image is applied to proposed direction generator. The obtained direction field ( $\mathbf{V}$ ) will be analyzed based

(a)



(b)
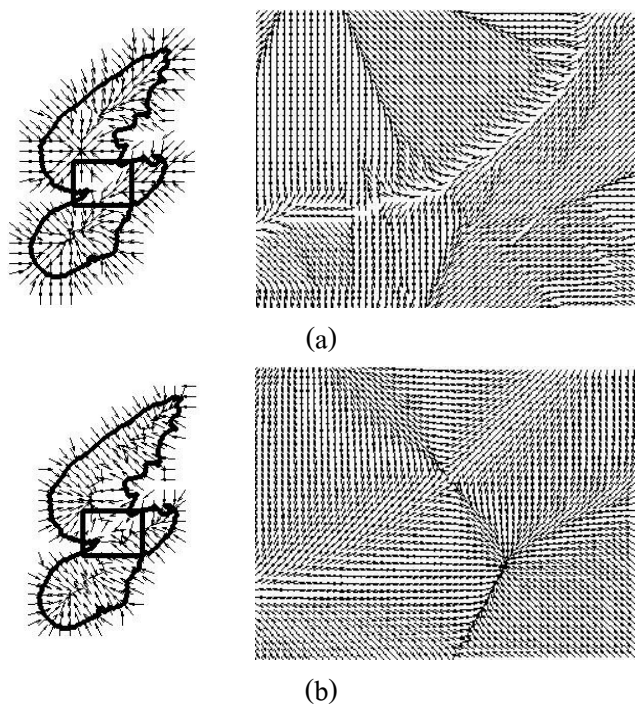
Fig. 3.5: (a) Direction field from the proposed direction generator. (b) Direction field from gradient direction of smoothed distance image.

on the direction requirement. Furthermore, its parameter setting will be also varied to present its characteristic under this situation.

**Direction Characteristic:** According to the direction requirement, the smoothing-and-contrasting direction abilities are the keys that determine the segmentation boundary. In direction environment, both abilities are obviously observed by direction field shown in Fig. 3.5. The direction field from the proposed direction generator in Fig. 3.5(a) is compared to that from the gradient direction of smoothed distance image in Fig. 3.5(b) on both abilities. The decision area for the segmentation of overlapping objects is located in the rectangular box. In addition, it is zoomed out and shown in the right image.

For smoothing direction ability, the direction field of the proposed direction generator seems to be more confusing than the gradient direction of smoothed distance image. Nevertheless, it can be still observed a pixel tracking to the area representing the individual nucleus. This means that the
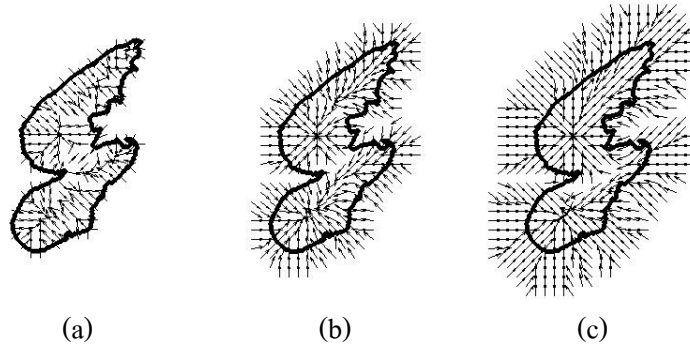
Fig. 3.6: The direction field from varying radius of disk-shaped structuring element in which

(a) $r=10$, (b) $r=30$, and (c) $r=50$.

direction smoothness from the proposed approach can maintain the tracking ability that guides all pixels in an individual nucleus to the same area or nearby. This occurring behavior illustrates the characteristics of direction field corresponding to the definition of proposed concept sufficiently. On the other hand, the direction field from the gradient direction of smoothed distance image cannot achieve the correct tracking because of the large of destination area that cannot judge the individual nucleus.

In case of contrasting direction ability, it is important for segmentation process since the segmentation decision is initially formed by this factor. From Fig. 3.5(a), our approach responds to this requirement very well as can be seen by distinct divergent directions. Its contrast directions are throughout on the segmentation decision continuously. This ensures that the initial segmentation process can extract the segmentation line. In the other one, low contrasting direction ability is odiously observed. It is risk to be the incomplete segmentation in decision function $\left(D(\ )\right)$.

**Parameter Response:** In this factor, the reaction of the direction generator is depended on two parameters, $E_d$ and $E_{sh}$. Since the $E_{sh}$ is in shrinking process, the erosion to all pixel in $B$ takes it to set structure element to one in radius. The remained parameter, $E_d$, can present the responsibility by variation of its radius. Let $E_d$ is defined to disk shape. The responsibility can be revealed as the example in Fig. 3.6. Where $r$ is the radius value, $r=10$ is not enough to hold

smoothing-and-contrasting direction abilities. In contrast, the over radius of $E_d$ in Fig. 3.6(c) performs the missed contrasting direction ability in segmentation boundary. At final definition, the obtained direction field covers completely on both direction abilities. These show the application of proposed approach in practice, which the parameter definition by the user is required.

## 3.5 Discussion

In this chapter, the direction field ($\mathbf{V}$) accomplishes the direction field requirement as contrasting-and-smoothing direction abilities. The outcome impacts certainly to segmentation approach where the individual nucleus has only the smoothing direction and the overlapping nuclei boundary has the contrasting direction between them. The proposed approach uses the local calculation to maintain the contrasting direction ability and also exploits the average of these local calculations to keep the smoothing direction ability. These abilities will support the decision function $\left( D(\ ) \right)$ to make the segmentation boundary, which will be described in later chapters. Hence, the success of overlapping nuclei segmentation begins when those direction abilities are in the nuclei area correctly which is the ambition of direction generator.

# Chapter 4

# Direction-based Spitting and Merging Technique

## 4.1 Introduction

In this chapter, the decision function as the basic concept in Fig. 2.3 will be proposed as a segmentation technique which employs the observable direction characteristics. This is shown as the principle in Section 4.2. Then, the numerical calculation will be initially described for the first step as Direction-based splitting in Section 4.3. The final step named Direction-based merging is performed to segment the overlapping nuclei as the description in Section 4.4. From the mentioned manner, the actual overlapping nuclei images will be experimented on this approach as the materials and methods in Section 4.5. The obtained results shown in Section 4.6 will be discussed in Section 4.7.

## 4.2 Principle

According to the synthesized overlapping nuclei surface in Fig. 4.1(a), the observation on it reveals the mountain range similarly. To separate it out, each side of mountain range can be considered the relationship among them. By visualization, where the relationship of a side group is extracted, the individual mountain will be discovered. The mentioned definition is clearly illustrated as demonstration in Fig. 4.1(b) where each side of mountain range is cut into smaller parts. Derived smaller pieces substitute for the each side of mountain range that will be determined the relationship. In this step, when the direction of each piece is presented as the white arrows as shown in Fig. 4.1(b), the relationship can be easily calculated by their direction destinations. The decision can group the surface pieces to the separated mountain when their directions are determined decision rule. It can be defined that the individual mountain consists of the surface pieces having the direction trying to direct to the same area or nearby. Therefore, from

(a)                                                    (b)



(c)
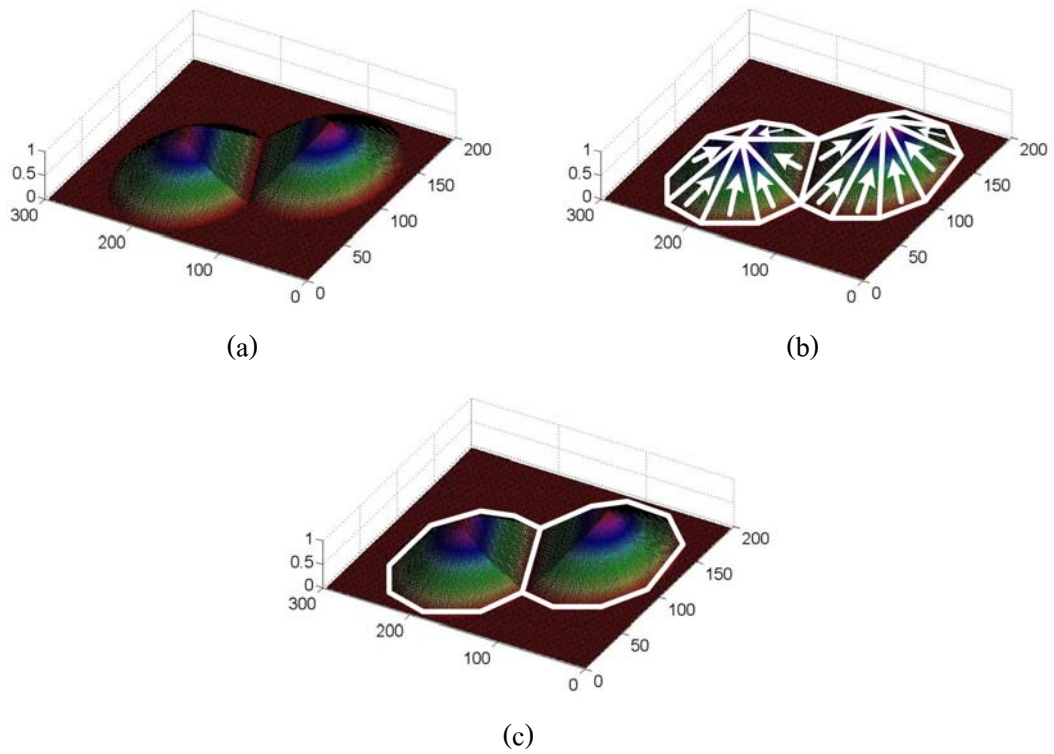
Fig. 4.1: The principle of splitting and merging technique. (a) Surface plot of synthesized

overlapping nuclei. (b) Split surface. (c) Merged surface.

this ideal, the proposed strategy can be summarized to splitting and merging approaches in which

their demonstrations are illustrated in Fig. 4.1(b)-(c) respectively.

## 4.3 Direction-based Splitting

Let $\mathbf{V}$ is the direction field from direction generator, the measurement of direction in $\mathbf{V}$ can be

made the split direction field. According to this, angle measurement is well responsibility where

the reference line is set to initial measurement. Clearly, the example in Fig. 4.2 illustrates the

angle measurement in a direction in $\mathbf{V}$. To calculate angle, arc tan of magnitude of $\mathbf{V}$ is used to

apply to
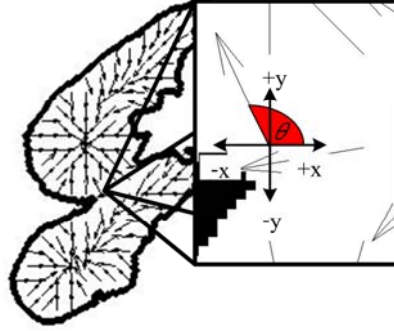
Fig. 4.2: Angle calculation at a direction in $\mathbf{V}$.

$$\theta(i,j) = \begin{cases} \mathrm{abs}\left[\tan^{-1}\langle \mathbf{V}(i,j)\rangle\right], & \text{If } Q(i,j)=1 \\ \mathrm{abs}\left[\tan^{-1}\langle \mathbf{V}(i,j)\rangle\right]+\pi/2, & \text{If } Q(i,j)=2 \\ \mathrm{abs}\left[\tan^{-1}\langle \mathbf{V}(i,j)\rangle\right]+\pi, & \text{If } Q(i,j)=3 \\ \mathrm{abs}\left[\tan^{-1}\langle \mathbf{V}(i,j)\rangle\right]+3\pi/2, & \text{If } Q(i,j)=4 \\ 3\pi/2, & \text{If } \mathrm{sign}\langle G(i,j)\rangle=0 \text{ and } \mathrm{sign}\langle H(i,j)\rangle<0 \\ \pi/2, & \text{If } \mathrm{sign}\langle G(i,j)\rangle=0 \text{ and } \mathrm{sign}\langle H(i,j)\rangle>0 \\ \pi, & \text{If } \mathrm{sign}\langle G(i,j)\rangle<0 \text{ and } \mathrm{sign}\langle H(i,j)\rangle=0 \\ 0, & \text{If } \mathrm{sign}\langle G(i,j)\rangle>0 \text{ and } \mathrm{sign}\langle H(i,j)\rangle=0 \end{cases} \tag{4.1}$$

where $\theta(i,j)$ is angle value at $P(i,j)$, $Q(i,j)$ is quadrant number addressed a direction, and the magnitude of $\mathbf{V}(i,j)$ represented by $G(i.j)$ and $H(i,j)$. From Eq. 4.1, a derived $\theta(i,j)$ is in range $0$ to $2\pi$. This is employed to splitting function where splitting range is defined as split region number ($q$). For instance, if $q=4$, the splitting function will divide $\theta$ to 4 groups with increasing range $2\pi/4$.

To illustrate the approach function, the example in Fig. 4.3 prepares $\theta$ from $\mathbf{V}$ using Eq. 4.1, and defines $q$ to 2, 4, 6, and 8. The reference line is set to $+x$ axis in 2D Cartesian coordination. The derived split regions of $\mathbf{V}$ are represented using different color on labeled region. The proposed approach achieves the object although, some cases, there is the interference of split region and tiny region such as $q=6$ from the unabsolute $\mathbf{V}$. However, these concerns can be compensated by the merging approach and morphology operator respectively.
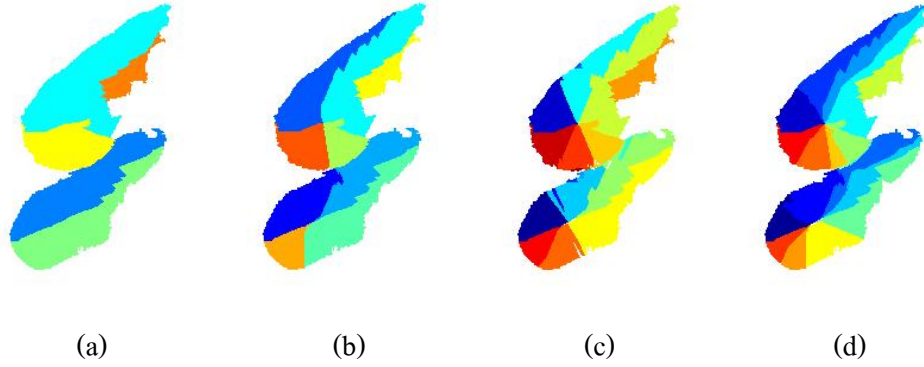
Fig. 4.3: Split region using (a) $q = 2$, (b) $q = 4$, (c) $q = 6$, and (d) $q = 8$.

## 4.4 Direction-based Merging

**Introduction to Direction-based Merging:** This step aims to extract $+\Omega_n$, which utilizes the split region to be inputted information. Let $\rho_k$ is a split region at $k^{th}$ from Section 4.3. The region $\rho_k$ must provide information in order to be used to extract the individual nuclei in decision function of merging process. Certainly, the direction in $\rho_k$ is correspondingly proper to this requirement. According to the smoothing direction ability provided by direction generator, this ability is useful to find out the relationship for individual nucleus extraction. It is the behavior that the directions in the individual nucleus try to direct to the same area or nearby. The application just calculates the direction agent of each $\rho_k$, and then groups them if these agents converge together. It is similar to the example of ideal shown in Fig. 4.1(b) and the following presents the computation of the direction agent of each $\rho_k$.

For the first step, the direction agent of each $\rho_k$ can be calculated by

$$V_k' = \left\| \left\langle \frac{\sum\limits_{(i',j') \in \rho_k} G(i', j')}{\mathrm{all}(\rho_k)}, \frac{\sum\limits_{(i',j') \in \rho_k} H(i', j')}{\mathrm{all}(\rho_k)} \right\rangle \right\|, \tag{4.2}$$
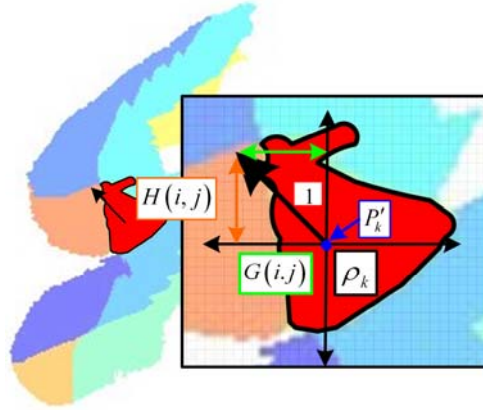
Fig. 4.4: The illustration of $V_k'$ and $P_k'$ in a $\rho_k$.

where $\mathrm{all}(\rho_k)$ yields all pixel number in $\rho_k$. Continuously, obtained $V_k'$ is next estimated using $\mathbf{r}_k = \begin{bmatrix} r_1 & r_2 & r_3....r_n \end{bmatrix}^T$ and $\mathbf{c}_k = \begin{bmatrix} c_1 & c_2 & c_3....c_n \end{bmatrix}^T$ to find the position of $V_k'$, where $\mathbf{r}_k$ and $\mathbf{c}_k$ keep the position of $V_k'$ in Cartesian coordinate. From this, the calculation is given by

$$P_k' = \left( \mathbf{r} \left\langle \mathrm{median}\left[\,\mathrm{size}(\mathbf{r})\,\right]\right\rangle, \mathbf{c} \left\langle \mathrm{median}\left[\,\mathrm{size}(\mathbf{c})\,\right]\right\rangle\right). \tag{4.3}$$

From Eq. 4.3, $P_k'$ is set to hold the position of $V_k'$ to be inside $\rho_k$ certainly. From those estimations, the split region in Fig. 4.2 can be further calculated to $V_k'$ and $P_k'$ as illustrated in Fig. 4.4. The vector shows the direction information from $V_k'$ while its origin locates at $P_k'$. Moreover, the direction agents on $n = 2, 4, 6,$ and $8$ are shown in Fig. 4.5.

Secondly, the $V_k'$ and $P_k'$ from the first step will be investigated characteristic to individual object extraction. Based on prior knowledge about vector on 2D space in Chapter 2, the relationship between them can be illustrated as Fig. 4.6. Let $V_a'$, $V_b'$, and $V_c'$ are the direction agent of three split region. The relationship among them is described to two cases by numerical computation. First case, the convergent characteristic between $V_a'$ and $V_b'$ can be estimated by perpendicular lines of $V_a'$ and $V_b'$ as shown in Fig. 4.6(a). There are boundaries between blue and red area. Also, these areas present over-and-under perpendicular lines. The convergent characteristic explicitly reveals through three operators as illustrated in Fig. 4.6(c). There are the cutting point which is obtained from the linear equation of $V_a'$ and $V_b'$, and terminus points of $V_a'$ and $V_b'$.
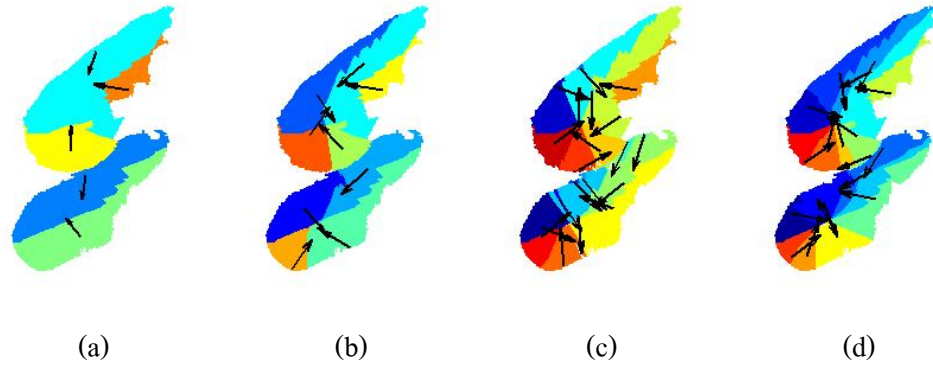
Fig. 4.5: Direction agent of each split region where (a) $q=2$, (b) $q=4$, (c) $q=6$, and (d) $q=8$.

The action of them yields the convergence measurement of two vectors. It is true when they are in the same area (blue area). On the other hand, the direction characteristic illustrating in Fig. 4.6(b) is obviously opposite together of $V_b'$ and $V_c'$. Similar to convergent characteristic, the perpendicular lines of the other case can be shown in Fig. 4.6(b). The cutting point and terminus points of $V_b'$ and $V_c'$ is on the different area as illustrated in Fig. 4.6(d). This factor will be measured to evaluate that it is divergent characteristic.

Here, there are two measurements for revealing $V_k'$ characteristic. To implement them to overlapping nuclei segmentation, it just estimates between connected split regions to convergent or divergent characteristic. From decision making, where the characteristic decision is judged to convergent result, the considered regions will be merged together. Thus, in the other side, the decision marking will avoid merging process due to the divergent characteristic. This rule can achieve the overlapping nuclei segmentation when all $V_k'$ in individual nucleus try to direct to the same area or nearby.

**Numerical Direction-based Merging:** From convergent-and-divergent characteristic measurement, the computation must initially provide the cutting point and the terminus point of a $V_k'$, and then judges the direction characteristic to merge or not. To accomplish this task, in each $V_k'$, the scheme must be obtained two operators such as linear equation and perpendicular linear equation of $V_k'$. There are respectively $y = mx + b$ and $y = -mx + b$, where $m$ and $b$ are the slope constant
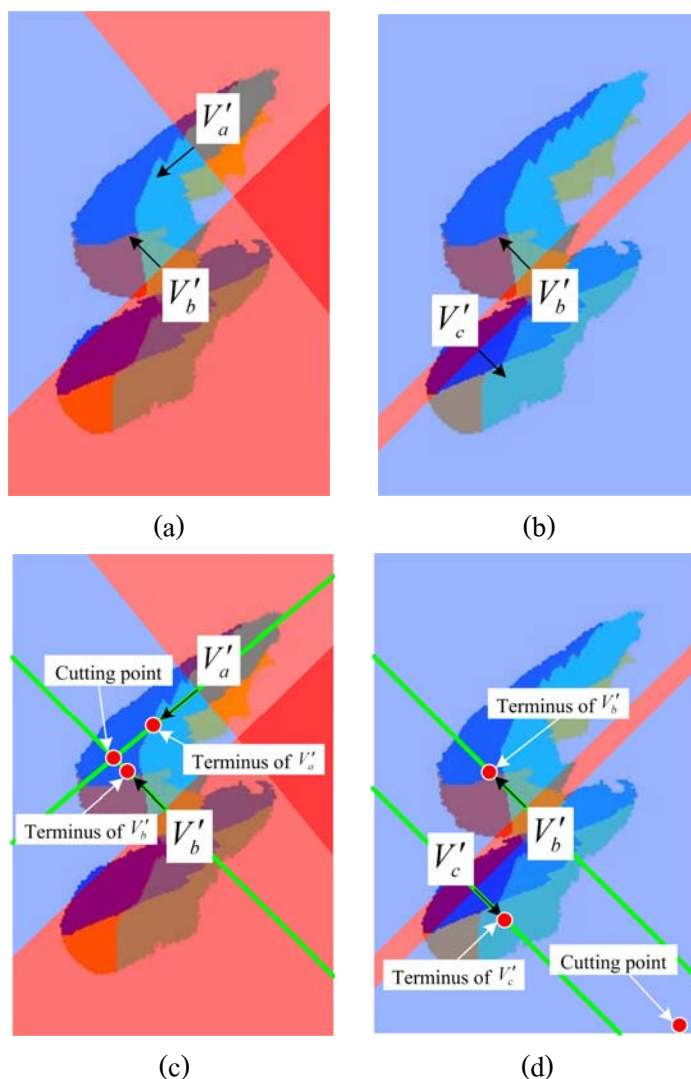
Fig. 4.6: Direction characteristics of two $V_k'$ where (a) and (c) are the convergent characteristic, (b) and (d) are divergent characteristic.

and the y-intercept. Let $V_a'$ and $V_b'$ be the $V_k'$ of connected region $a$ and $b$. The cutting point will be calculated from $V_a'$ and $V_b'$ linear equation as demonstrated in Fig. 4.6. In case of terminus point of $V_a'$ and $V_b'$, they are obtained from the summary of $P_k'$ and $V_k'$.

Here, the calculation already provides cutting point and terminus points. These positions will be applied to decide the direction characteristic. By approving these points that they are in the same area of both perpendicular line, it can judge their characteristic to convergent. Otherwise, the
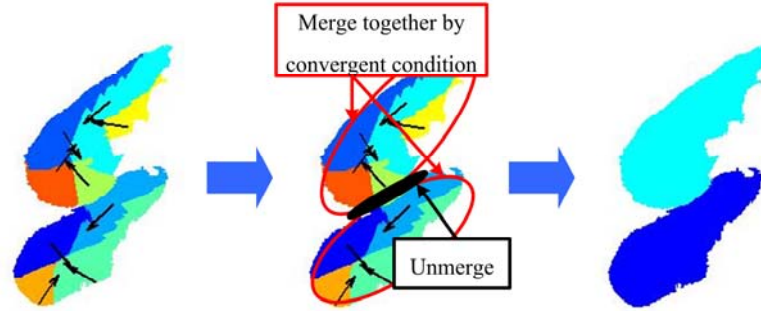
Fig. 4.7: Completely overlapping nuclei segmentation.

characteristic will be divergent. To implement this rule, the existed points will be placed to both perpendicular linear equations by the following: [34]

$$
\begin{aligned}
s_1 &= \text{sign}\left\langle b_a - \left(y_1 - m_a x_1\right)\right\rangle, \\
s_2 &= \text{sign}\left\langle b_a - \left(y_2 - m_a x_2\right)\right\rangle, \\
s_3 &= \text{sign}\left\langle b_b - \left(y_1 - m_b x_1\right)\right\rangle, \\
s_4 &= \text{sign}\left\langle b_b - \left(y_3 - m_b x_3\right)\right\rangle,
\end{aligned}
\tag{4.4}
$$

where $\left(x_1, y_1\right)$, $\left(x_2, y_2\right)$, and $\left(x_3, y_3\right)$ are positions of cutting point, terminus point of $V_b'$, and terminus point of $V_a'$ respectively. The $m_a$ and $b_a$ are the slope constant and the y-intercept of $V_a'$, which are also in $m_b$ and $b_b$ of $V_b'$. The results from $s_1$ to $s_4$ will be applied to following algorithm:

**Direction-based splitting and merging:**

Calculate split region

Find $V_k'$ and $P_k'$

Loop all connected region

        Calculate cutting point, terminus points

        Find $s_1$, $s_2$, $s_3$, and $s_4$

        If $s_1 = s_2$ and $s_3 = s_4$

            Merge these split regions

        End

End loop
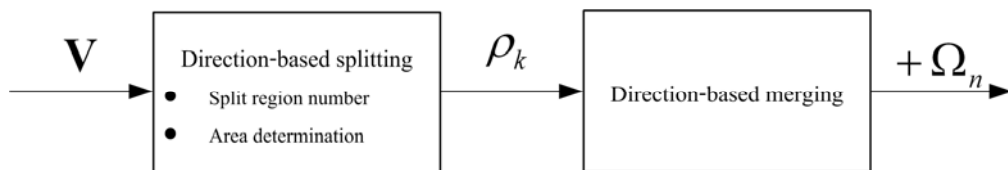
Fig. 4.8: Workflow of the proposed scheme.

Fig. 4.7 shows the complete merging region which represents the segmented overlapping nuclei. The process just re-labels the pixel number after judging to merge together.

## 4.5 Materials and Methods

From prepared direction field by direction generator in Chapter 3, the experiment will be set the parameter for the split region number and area determination as the workflow in Fig. 4.8. For the

| No. | Split region number | Correct | Over | Under |
|-----|---------------------|---------|------|-------|
| 1 | 2 | 190 | 112 | 8 |
| 2 | 4 | 196 | 25 | 15 |
| 3 | 6 | 199 | 8 | 12 |
| 4 | 8 | 201 | 9 | 12 |
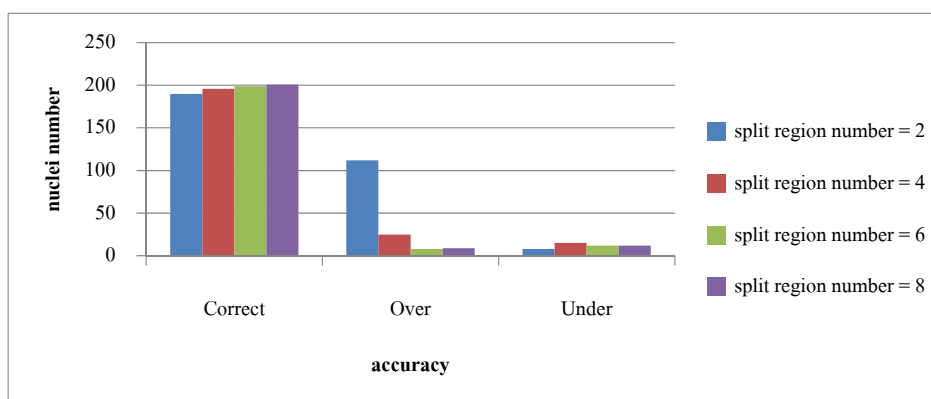


Fig. 4.9: Segmentation results from varying split region number.
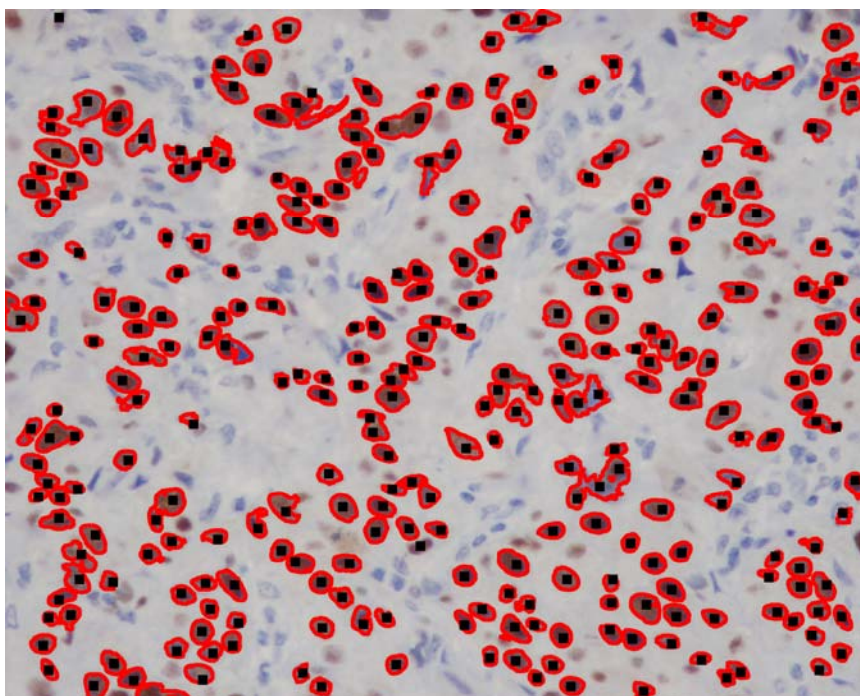
Fig. 4.10: Segmentation results (red line) with expert markers (black dot).

first, varying the split region number is performed to present the performance response to the merging process. The 2, 4, 6, 8 are the varied of $q$. The objects which are smaller than 50 are released. The best one to the expert in correct-over-and-under segmentation results will be selected to all experimented images.

Fig. 4.9 shows segmentation results from the varying split region number. Summary table and graph distinctly indicates that eight split region is best. It gives the highest correct segmentation and low on both over-and-under segmentations. Therefore, this value will be thoroughly used to entire experimented images.

## 4.6 Results

The twenty nine images provided to the proposed approach are evaluated the performance using comparison to the expert. The correct-over-and-under segmentation yields the algorithm performance as shown in Table. 4.1 and the segmentation results in Fig. 4.10. Let all items in

summary be formed in percent. The performance measurements are 92.08 %, 3.12 %, and 6.49 % for correct, over, and under segmentation respectively. Over 90 % of correct segmentation is achieved from the proposed approach. Less than 10 % of undersigned performance from over-and-under segmentation is also succeeded. These are preliminary results and discussions. However, the performance validation will be deeply argued in Chapter 7 in which the comparison to other direction-based techniques and tradition overlapping nuclei algorithm is provided.

## 4.7 Discussion

In this chapter, $D(\ )$ is performed on the obvious direction characteristic based on group and re-group direction strategy. It is called direction-based splitting and merging technique (DSMT) which is respectively explained from basic concept to numerical implementation on the existed direction field. The parameter setting is only required on $q$ which controls the split region number. The varied $q$ yields the selected $q$ to eight with best segmentation accuracy. The provided $q$ is applied to the experiment on the actual nuclei image. The segmentation results shown in Table 4.1 are reported through the correct, over, and under segmentation in quantification value. However, for performance validation in deeply, these results will be compared with other direction-based techniques in Chapter 7.

TABLE 4.1: Quantification accuracy.

| No. | Image name | Expert | Correct | Over | Under |
|-----|------------|--------|---------|------|-------|
| 1 | T51-1549A1 | 215 | 201 | 9 | 12 |
| 2 | T51-1549A2 | 243 | 228 | 9 | 11 |
| 3 | T51-1549A3 | 269 | 243 | 1 | 21 |
| 4 | T51-1549A4 | 250 | 226 | 2 | 22 |
| 5 | T51-1549A5 | 192 | 177 | 11 | 14 |
| 6 | T51-1549A9 | 265 | 251 | 5 | 13 |
| 7 | T51-1549A12 | 229 | 219 | 2 | 7 |
| 8 | T51-1549A17 | 230 | 219 | 3 | 9 |
| 9 | T51-1549A21 | 207 | 186 | 5 | 19 |
| 10 | T51-1549A23 | 294 | 268 | 7 | 22 |
| 11 | T51-1549A36 | 204 | 194 | 4 | 7 |
| 12 | T51-1549A37 | 242 | 221 | 8 | 15 |
| 13 | T51-1549A39 | 205 | 185 | 6 | 17 |
| 14 | T51-1549A40 | 233 | 218 | 6 | 14 |
| 15 | T51-1549A41 | 167 | 140 | 7 | 23 |
| 16 | T51-1549A42 | 210 | 191 | 9 | 14 |
| 17 | T51-1549A44 | 268 | 252 | 3 | 13 |
| 18 | T51-1549A53 | 283 | 237 | 9 | 35 |
| 19 | T51-1549A54 | 259 | 238 | 7 | 15 |
| 20 | T51-1549A59 | 176 | 162 | 17 | 10 |
| 21 | T51-1549A60 | 225 | 210 | 10 | 12 |
| 22 | T51-1549A73 | 168 | 151 | 3 | 14 |
| 23 | T51-1549A78 | 201 | 185 | 6 | 14 |
| 24 | T51-1549A92 | 173 | 162 | 10 | 9 |
| 25 | T51-1549A97 | 140 | 126 | 4 | 12 |
| 26 | T51-1549A-78 | 241 | 232 | 2 | 7 |
| 27 | T51-1549A-134 | 252 | 239 | 12 | 12 |
| 28 | T51-1549A-135 | 227 | 212 | 9 | 11 |
| 29 | T51-1549A-149 | 107 | 97 | 13 | 10 |
| | Sum | 6375 | 5870 | 199 | 414 |

# Chapter 5

# Direction-based Classification Technique

## 5.1 Introduction

Outcome of direction-based application is not only in splitting and merging technique as the previous chapter. In general, the newer strategy is usually discovered by the improvement or solution of the older technique. Also in this chapter, the new one is proposed by the observation of the direction characteristics in alternated idea to approach the object on nuclei segmentation. In Fig. 5.1(a), the direction field illustrated visually the convergent behavior on the individual nucleus area while the divergent behavior locates at the boundary of overlapping nuclei area. The segmented line can be accomplished by classifying a pixel to boundary area or overlapping nuclei. Then, segmented line will be extracted from the divergent area using morphology operator. As shown in Fig 5.1(b), the example shows the divergent area (blue) which is applied the morphology operator to build single pixel of segmented line.



(a)            (b)
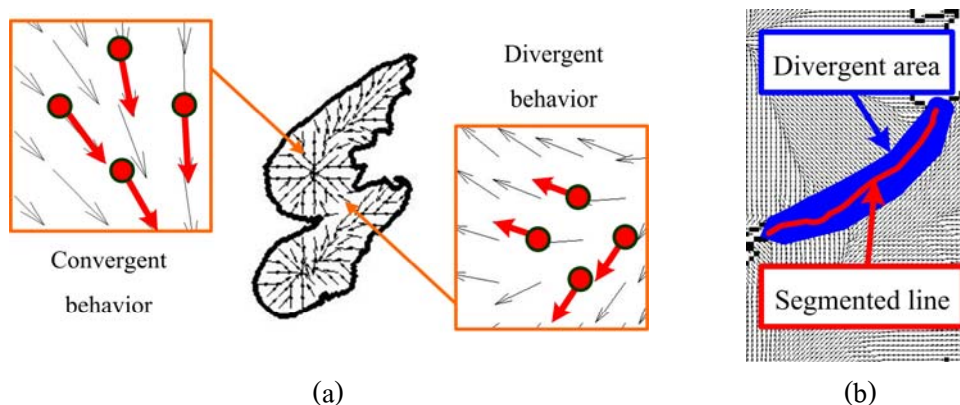
Fig. 5.1: (a) The principle of divergent-and-convergent direction characteristics. (b) The extraction of segmented line from divergent area.

From the mentioned principle of this concept, the process can be mainly derived in two steps. There are pixel classification and boundary extraction. The pixel classification is performed the decision of a pixel into the convergent-and-divergent direction characteristics. The obtained results are two classes that can be transformed to binary form. Subsequently, the boundary extraction process containing the basic morphology operators will make the single pixel construction on the divergent area [35].

The remainder of this chapter is as follows. In Section 5.2, the two main steps are described simultaneously on their theory and the application direction field of overlapping nuclei. Then, the implementation on actual overlapping nuclei is presented in Section 5.3 as materials and methods. The parameter setting, workflow, and reinforce process are also contained in this section. The results from segmentation evaluation are in Section 5.4 in which discussions of the results are included finally.

## 5.2 Theory

Figure 5.1 shows the directions of two overlapping objects. One can see that the directions can be divided into two groups: convergent and divergent characteristics. While the direction in the object region is convergent, the direction in the boundary region is divergent. Based on this observation, we propose a direction-based classification technique (DBCT) which is the method aiming to divide a direction into two groups based on its direction characteristics. Subsequently, the classification results can be employed on separating overlapping objects by boundary extraction method. Therefore, this section will be expressed *principle*, *numerical DBCT*, and *boundary extraction* which are represented based on $\mathbf{V}$ in Fig. 5.1.

**Principle:** The objective in extraction of direction behavior is based on utilization of neighbor directions in a $\mathbf{V}(i, j)$. As the example in Fig. 5.2(a)-(b), a $\mathbf{V}(i, j)$ cannot perform this task alone. It requires four neighbor directions to indicate the direction behaviors. Therefore, this computation will use them through angle summation into $\theta^{+}$ and $\theta^{-}$ as shown in Fig. 5.2(b)-(c).
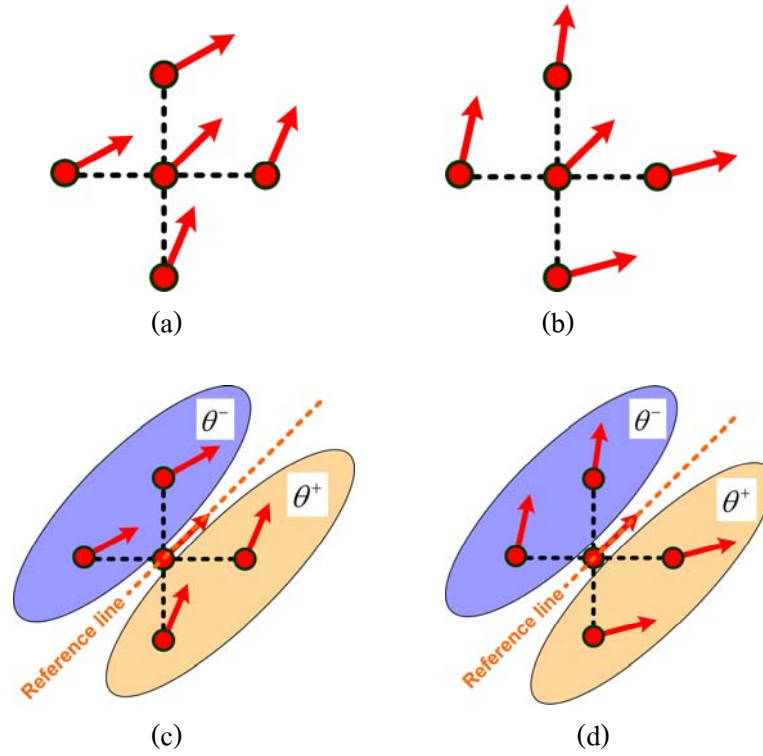
Fig. 5.2: (a)-(b) are the appearances of convergent-and-divergent characteristics indicating by neighbor directions. (c)-(d) show the grouping of neighbor angles.

The $\theta^+$ is on the right side and $\theta^-$ is on the left side of reference line, which is indicated by the dash line. Let $\omega$ be the angle difference. The measurement of direction behavior can be

$$\omega = \theta^+ - \theta^-. \tag{5.1}$$

To show its performance, let assuming the neighbor angles of $\mathbf{V}(i, j)$ be 60, 60, 45, and 45 degree for north, west, south and east position to the $\mathbf{V}(i, j)$. The $\theta^+$ will be 120 degree and the $\theta^-$ will be 90. Therefore, the $\omega$ equals to 30. In other case, the assumed neighbor angles are 30, 30, 80, and 80. The results are 60 and 160 degree of $\theta^+$ and $\theta^-$ respectively. The $\omega$ of this case will become to -100 degree. The 30 and -100 degrees can be used to classify a $\mathbf{V}(i, j)$ to divergent-or-convergent behaviors using threshold method.

**Numerical DBCT:** To illustrate the DBCT in numerical calculation, we employ the direction field through the gradient to prepare $\theta^{+}$ and $\theta^{-}$. First, we estimate $\theta$ which uses the reference line $v$ by

$$\theta(i,j,v) = \begin{cases} \text{abs}\left[\tan^{-1}\langle \mathbf{V}(i,j)\rangle\right], & \text{If } Q(i,j)=1 \\ \text{abs}\left[\tan^{-1}\langle \mathbf{V}(i,j)\rangle\right]+\pi/2, & \text{If } Q(i,j)=2 \\ \text{abs}\left[\tan^{-1}\langle \mathbf{V}(i,j)\rangle\right]+\pi, & \text{If } Q(i,j)=3 \\ \text{abs}\left[\tan^{-1}\langle \mathbf{V}(i,j)\rangle\right]+3\pi/2, & \text{If } Q(i,j)=4 \\ 3\pi/2, & \text{If sign}\langle G(i,j)\rangle=0 \text{ and sign}\langle H(i,j)\rangle<0 \\ \pi/2, & \text{If sign}\langle G(i,j)\rangle=0 \text{ and sign}\langle H(i,j)\rangle>0 \\ \pi, & \text{If sign}\langle G(i,j)\rangle<0 \text{ and sign}\langle H(i,j)\rangle=0 \\ 0, & \text{If sign}\langle G(i,j)\rangle>0 \text{ and sign}\langle H(i,j)\rangle=0 \end{cases} \tag{5.2}$$

where $\theta(i,j)$ is angle value at $P(i,j)$, $Q(i,j)$ is quadrant number addressed a direction, and the magnitude of $\mathbf{V}(i,j)$ represented by $G(i.j)$ and $H(i,j)$.
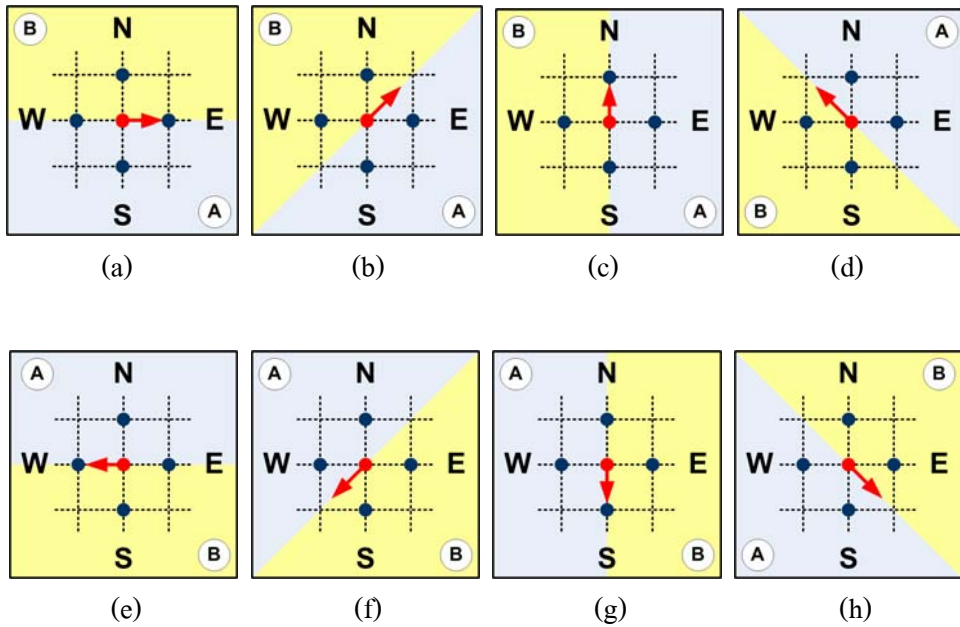


Fig. 5.3: The possible cases of sign operators are identified by $\mathbf{V}(i,j)$ or central direction, where areas A are the positive side; areas B are the negative side.

Consequently, the angle from neighborhood pixels at the north, east, south, and west in vector form can be given by

$$\mathbf{p}(i,j,v) = \begin{bmatrix} \theta_{North} & \theta_{East} & \theta_{South} & \theta_{West} \end{bmatrix}. \qquad (5.3)$$

Then, the reference line as example shown in Fig. 5.2(c)-(d) will group those neighbor $\theta$ into two groups. There are $\theta^+$ and $\theta^-$ where $\theta^+$ is on the right side and $\theta^-$ is on the left side of reference line as the possible cases in Fig. 5.3. Thus, the grouped $\theta$ can be achieved by sign identification as

$$\mathbf{s}(i,j) = \begin{cases} \begin{bmatrix} -1 & 1 & 1 & -1 \end{bmatrix}^T, & G(i,j) > 0 \text{ and } H(i,j) > 0 \\ \begin{bmatrix} 1 & 1 & -1 & -1 \end{bmatrix}^T, & G(i,j) < 0 \text{ and } H(i,j) > 0 \\ \begin{bmatrix} -1 & 1 & 1 & -1 \end{bmatrix}^T, & G(i,j) < 0 \text{ and } H(i,j) < 0 \\ \begin{bmatrix} -1 & -1 & 1 & 1 \end{bmatrix}^T, & G(i,j) > 0 \text{ and } H(i,j) < 0 \\ \begin{bmatrix} 0 & -1 & 0 & 1 \end{bmatrix}^T, & G(i,j) = 0 \text{ and } H(i,j) < 0 \\ \begin{bmatrix} 0 & 1 & 0 & -1 \end{bmatrix}^T, & G(i,j) = 0 \text{ and } H(i,j) > 0 \\ \begin{bmatrix} 1 & 0 & -1 & 0 \end{bmatrix}^T, & G(i,j) < 0 \text{ and } H(i,j) = 0 \\ \begin{bmatrix} -1 & 1 & 1 & 0 \end{bmatrix}^T, & G(i,j) > 0 \text{ and } H(i,j) = 0 \end{cases} \qquad (5.4)$$

Based on $\mathbf{p}$ and $\mathbf{s}$, the $\omega$ can be expressed as

$$\omega(i,j,v) = \mathbf{p}(i,j,v) \times \mathbf{s}(i,j). \qquad (5.5)$$

Finally, the threshold method will be applied to classify the $\omega(i,j,v)$ to binary image, which is given by

$$B(i,j,v) = \begin{cases} 0, & \omega(i,j,v) < TH \\ 1, & \text{Otherwise} \end{cases}, \qquad (5.6)$$

where $TH$ is threshold value. In some cases, for example, if $\theta^+$ and $\theta^-$ consist of the neighbor $\theta$ from positive x-axis in the first or the fourth quadrant, the $\omega$ value is not in the range of $-\pi < \omega < +\pi$. This is the wrong angle difference causing the error in binary image from threshold
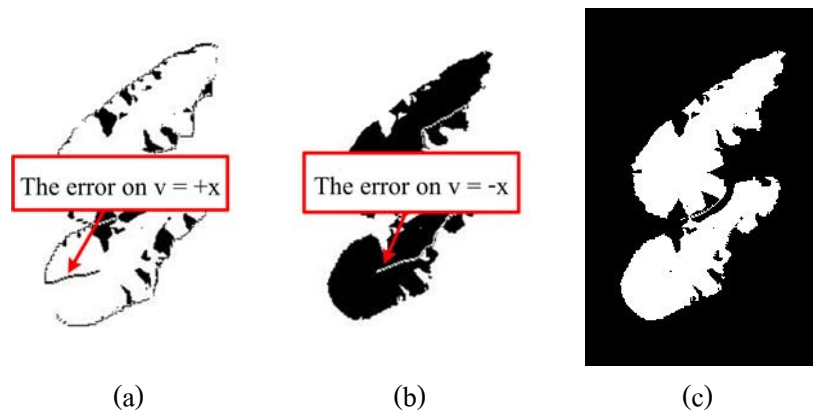
Fig. 5.4: (a)-(b) The errors occurring from crossing quadrant. (c) Corrected $B$ .

method. To solve this problem, the twice calculated $\omega$ on v = +x and v = -x can be used for compensation. Let consider the $B$ obtained from v = +x and v = -x as illustrated in Fig. 5.4(a)-(b). The errors show difference in location, which can be healed by

$$B = B(i, j, v = +x) \text{ or } \overline{B(i, j, v = -x)}. \tag{5.7}$$

Fig. 5.4(c) shows the corrected $B$ which remains the area of boundary of overlapping nuclei. To complete the single pixel boundary, this task will be forwarded to the next step called boundary extraction.

**Boundary Extraction:** To extract single pixel boundary, this step provides the combination of morphology operators that are performed respectively as following.

Erosion operator: Fig. 5.4(c) shows the obtained binary image comprising the local minima (white line in black area). It is eliminated using morphological erosion operator with a $3 \times 3$ square structuring element as shown in Fig. 5.5(a).

Hole filling: Also, the local maxima (black dot in white area) is another characteristic obtained from the DBCT as shown in Fig. 5.5(a). The solution employs the hole filling algorithm to eliminate the hole as shown in Fig. 5.5(b).
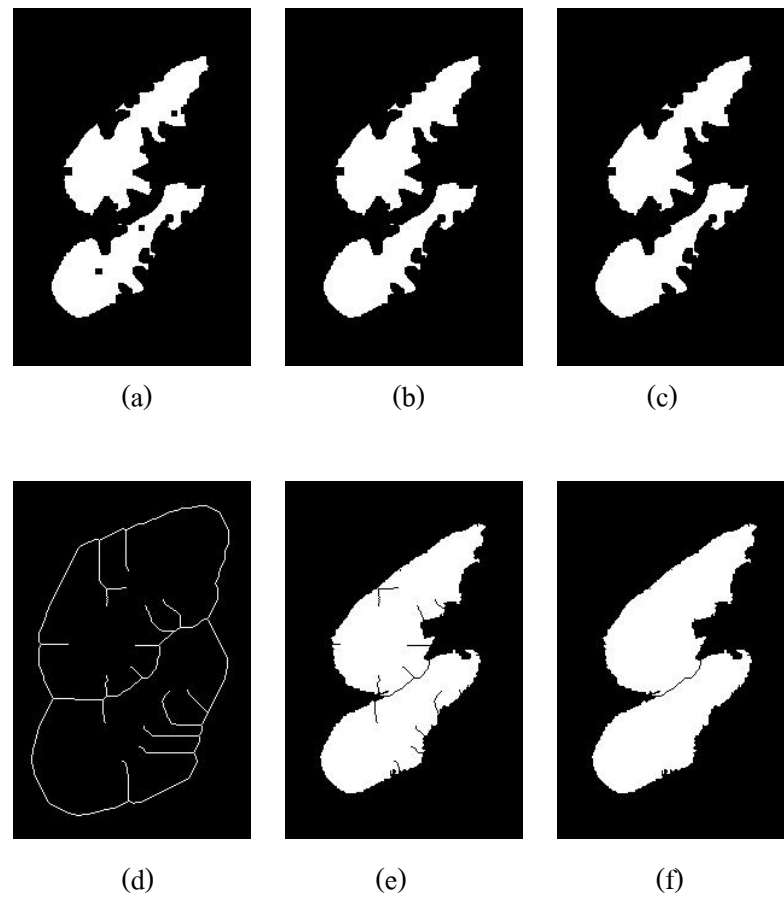
Fig. 5.5: (a) Obtained result from erosion operator. (b) The filled hole result. (c) Fragmental elimination. (d) Single pixel boundary from thinning process. (e) The single pixel boundary superimposed on binary image. (f) Branch pixels are released using de-branch operator.

Fragment elimination: In this stage, the small-size objects, considered as noises, are removed as shown in Fig. 5.5(c).

Thinning: From the boundary requirement, the single pixel boundary must be extracted to show the real boundary. This is conducted by the thinning operator, which operates under the binary environment as shown in Fig. 5.5(d).

De-branch: In this stage, the provided binary image has the single pixel boundaries as shown in Fig. 5.5(d). In some cases, the obtained boundaries have branches caused from the thinning operator. To eliminate them, this scheme proposes an uncomplicated method

to solve this problem. It is called the de-branch operator. Let $B$ be the obtained binary image, and $W$ be $3 \times 3$ square matrix superimposed on the labeled $B$, with the center of $W$ located at any position of $W$, the decision function used to determine the existing branch is:

$$B = \begin{cases} 0, & \sum_{i=1}^{3} \sum_{j=1}^{3} \left( W_{i,j} - m \right) = 0 \\ 1, & \text{Otherwise} \end{cases}, \tag{5.8}$$

where $m$ is the average of $W$ excluding $W_{i,j} = 0$. The result gives $B$ which is replaced with zero when that pixel is the branch component. From the example, the complete boundary excluding branches in the final step is illustrated in Fig. 5.5(f).

## 5.3 Materials and Methods

The algorithm for overlapping object segmentation based on the DBCT consists of three steps: direction preprocessing, direction-based classification technique (DBCT), and boundary extraction. The additional step, direction preprocessing, applies filter to smooth $\mathbf{V}$ in magnitude, and complete the reference direction. The threshold value is set to zero in DBCT process. The provided $\mathbf{V}$ from the calculation in Chapter 2 are provided to the proposed process in Fig. 5.5. Finally, the quantification evaluation is illustrated, where the gold standard by expert is compared to.

## 5.4 Results

The experimented images are provided to the proposed algorithm by prepared $\mathbf{V}$. The obtained results are evaluated in correct, over, and under segmentation compared with marker from expert as the example in Fig. 5.6. They are represented as the summarized results in Table 5.1. There are 96.83 %, 8.14 %, and 1.69 % for correct, over, and under segmentation in percent. For error segmentation, over and under, they show the error lower than 10 % similar to the previous
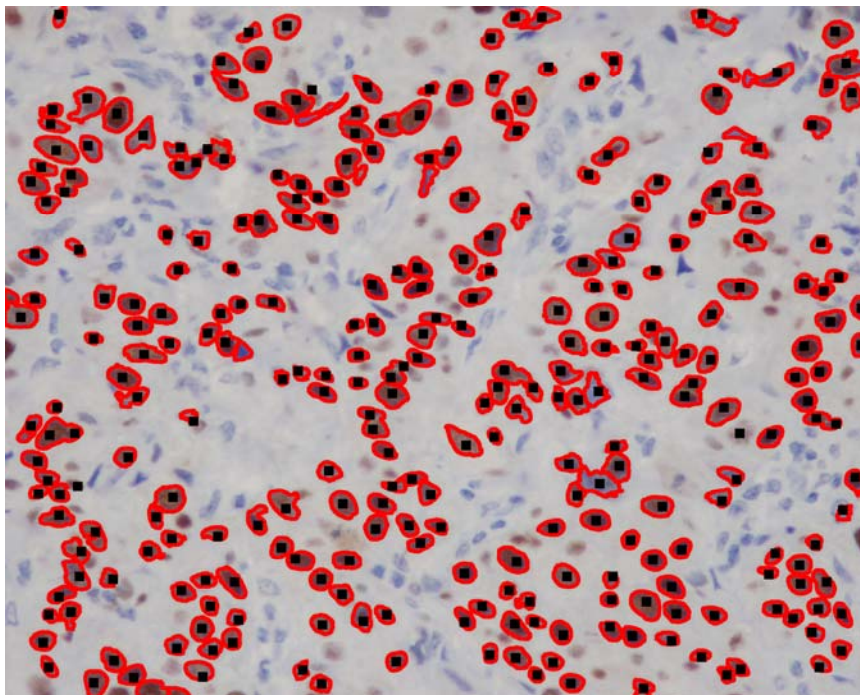
Fig. 5.6: Segmentation results (red line) with expert markers (black dot).

technique in Chapter 4. In addition, the correct segmentation shows the accuracy performance that can achieve over 90 %.

## 5.5 Discussion

The direction-based classification technique (DBCT) is a pixel-based calculation utilizing direction characteristics. It is simple when this technique depends on such fundamental computation. The angle difference received from determination of direction characteristics yields the classifying-able value using defined threshold. Where the individual nucleus is formed to one of direction characteristics, the obtained result from this classification will locate the existed individual nucleus in binary image. Finally, the boundary extraction is performed to achieve single pixel boundary and complete individual nucleus area. The experiment on actual nuclei images which are provided the direction field gives the segmented results on correct-over-and-under segmentation in quantification value. However, this results and discussions only describe its performance in general. It needs to compare with other techniques, and validated by other

factors. This will be provided in Chapter 7. For direction-based segmentation in this dissertation, next chapter will propose a alternated technique which the existing direction will be acted as the moving pixel.

TABLE 5.1: Quantification accuracy.

| No. | Image name | Expert | Correct | Over | Under |
|---|---|---|---|---|---|
| 1 | T51-1549A1 | 215 | 212 | 19 | 2 |
| 2 | T51-1549A2 | 243 | 236 | 25 | 3 |
| 3 | T51-1549A3 | 269 | 260 | 15 | 5 |
| 4 | T51-1549A4 | 250 | 238 | 16 | 8 |
| 5 | T51-1549A5 | 192 | 186 | 22 | 1 |
| 6 | T51-1549A9 | 265 | 262 | 15 | 3 |
| 7 | T51-1549A12 | 229 | 224 | 11 | 2 |
| 8 | T51-1549A17 | 230 | 225 | 11 | 2 |
| 9 | T51-1549A21 | 207 | 194 | 17 | 6 |
| 10 | T51-1549A23 | 294 | 281 | 22 | 8 |
| 11 | T51-1549A36 | 204 | 199 | 13 | 3 |
| 12 | T51-1549A37 | 242 | 234 | 17 | 3 |
| 13 | T51-1549A39 | 205 | 197 | 15 | 4 |
| 14 | T51-1549A40 | 233 | 231 | 18 | 1 |
| 15 | T51-1549A41 | 167 | 162 | 22 | 3 |
| 16 | T51-1549A42 | 210 | 205 | 16 | 5 |
| 17 | T51-1549A44 | 268 | 262 | 8 | 2 |
| 18 | T51-1549A53 | 283 | 256 | 21 | 14 |
| 19 | T51-1549A54 | 259 | 250 | 17 | 6 |
| 20 | T51-1549A59 | 176 | 174 | 32 | 1 |
| 21 | T51-1549A60 | 225 | 220 | 24 | 4 |
| 22 | T51-1549A73 | 168 | 152 | 13 | 7 |
| 23 | T51-1549A78 | 201 | 197 | 11 | 1 |
| 24 | T51-1549A92 | 173 | 166 | 15 | 3 |
| 25 | T51-1549A97 | 140 | 135 | 11 | 4 |
| 26 | T51-1549A-78 | 241 | 238 | 11 | 1 |
| 27 | T51-1549A-134 | 252 | 250 | 32 | 1 |
| 28 | T51-1549A-135 | 227 | 223 | 20 | 2 |
| 29 | T51-1549A-149 | 107 | 104 | 30 | 3 |
| | Sum | 6375 | 6173 | 519 | 108 |

# Chapter 6

# Direction-based Flow Tracking Technique

## 6.1 Introduction

According to characteristic of $\mathbf{V}$ in smoothing direction ability in Chapter 2, its behavior on all directions in the individual nucleus trying to direct to the same area can be utilized on overlapping nuclei segmentation. This concept is based on moving pixel. When a pixel is assigned to move using the guidance by $\mathbf{V}$, the result can yield the separation of pixel groups of individual nucleus when they finish the movement. These pixel groups will be numbered and then extracted to the original pixel position. There are the labeled pixels which are represented the segmented nuclei later.

From above concept, the principle can be described basically as theory in Section 6.2. Based on the existed scheme, it can support the movement to designed concept with its modification as expressed in Section 6.3. The materials and methods in Section 6.4 show the implementation on the actual overlapping nuclei image when the obtained results and discussion are illustrated in Section 6.5 and 6.6 subsequently.

## 6.2 Principle

From the previous works, the moving pixel on $\mathbf{V}$ as the mentioned idea can be implemented using the simple computation as the "gradient flow tracking" [29]. This scheme moves a pixel by

$$\mathbf{p}' = \mathbf{p} + round\left\{\mathrm{K}(\mathbf{p})\right\}, \tag{6.1}$$

where $\mathrm{K}(\mathbf{p})$ yields the direction through the normalized vector $\mathbf{V}$ at the position $\mathbf{p}$. In practice, the pixel position $\mathbf{p}$ is moved to next position by rounding of its direction and then summed to the

$$\mathbf{p} = (1,1)$$
$$V(\mathbf{p}) = (1,1)$$
$$\therefore \mathbf{p}' = \mathbf{p} + round\{V(\mathbf{p})\}$$
$$= (1,1) + (1,1)$$
$$= (2,2)$$

$$\mathbf{p} = (2,2)$$
$$V(\mathbf{p}) = (-1,1)$$
$$\therefore \mathbf{p}' = \mathbf{p} + round\{V(\mathbf{p})\}$$
$$= (2,2) + (-1,1)$$
$$= (1,3)$$

$$\mathbf{p} = (1,3)$$
$$V(\mathbf{p}) = (-1,1)$$
$$\therefore \mathbf{p}' = \mathbf{p} + round\{V(\mathbf{p})\}$$
$$= (1,3) + (-1,1)$$
$$= (0,4)$$

(a)          (b)          (c)
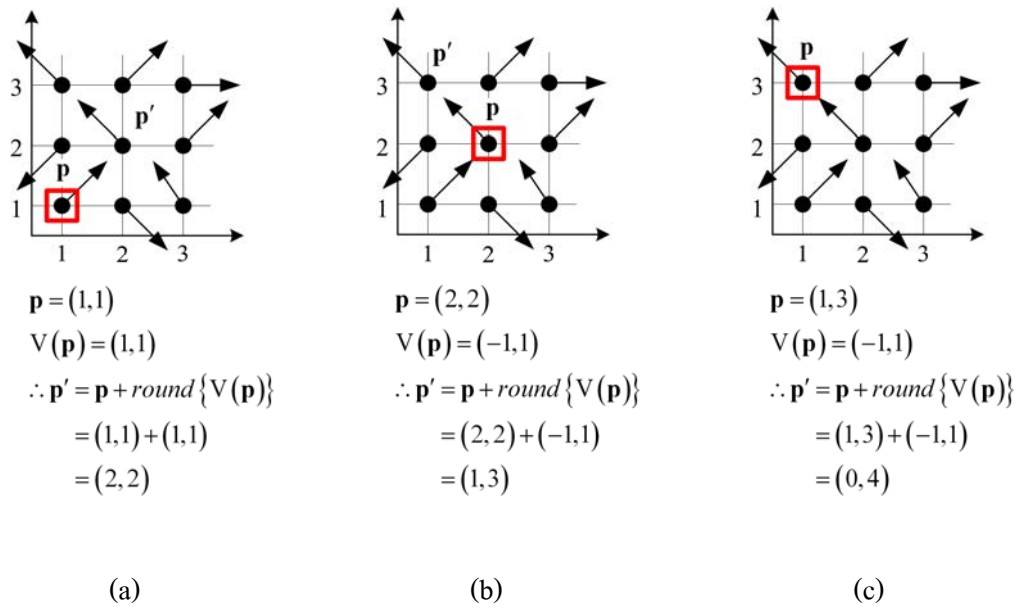
Fig. 6.1: Pixel movement using gradient flow tracking in Eq. 6.1, where the iteration process is sequentially computed from (a) to (c).

previous $\mathbf{p}$ to update the position to $\mathbf{p}'$. For example, Fig. 6.1 illustrates the estimation of position of $\mathbf{p}$ and $\mathbf{p}'$. It shows the pixel movement using red box, which is taken the next move by $\mathbf{p}'$.

However, the designed concept requires the finished movement of moving pixel. This can be achieved by adding the designed ability to Eq. 6.1. Therefore, the next section named "Direction-
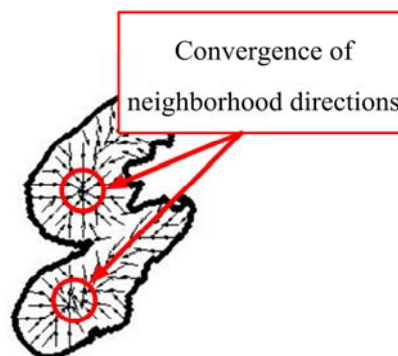


Fig. 6.2: Convergent neighborhood area of directions.

$\mathbf{p} = (2,2)$

$K(\mathbf{p}_N) = (1,0); K(\mathbf{p}_E) = (0,1); K(\mathbf{p}_S) = (1,1); K(\mathbf{p}_W) = (1,1)$

$\mathbf{p}' = \mathbf{p} + round\{\langle K(\mathbf{p}_N) + K(\mathbf{p}_E) + K(\mathbf{p}_S) + K(\mathbf{p}_W)\rangle/4\}$

$= (2,2) + round\{\langle (1,0) + (0,1) + (1,1) + (1,1)\rangle/4\}$

$= (2,2) + round\{\langle (3,3)\rangle/4\}$

$= (2,2) + round\{\langle (0.75, 0.75)\rangle\}$

$= (2,2) + (1,1)$

$= (3,3)$

(a)



$\mathbf{p} = (3,3)$

$K(\mathbf{p}_N) = (0,-1); K(\mathbf{p}_E) = (-1,0); K(\mathbf{p}_S) = (0,1); K(\mathbf{p}_W) = (1,0)$

$\mathbf{p}' = \mathbf{p} + round\{\langle K(\mathbf{p}_N) + K(\mathbf{p}_E) + K(\mathbf{p}_S) + K(\mathbf{p}_W)\rangle/4\}$

$= (3,3) + round\{\langle (0,-1) + (-1,0) + (0,1) + (1,0)\rangle/4\}$

$= (3,3) + round\{\langle (0,0)\rangle/4\}$

$= (3,3) + round\{\langle (0,0)\rangle\}$

$= (3,3) + (0,0)$

$= (3,3)$

(b)



$\mathbf{p} = (3,3)$

$K(\mathbf{p}_N) = (0,-1); K(\mathbf{p}_E) = (-1,0); K(\mathbf{p}_S) = (0,1); K(\mathbf{p}_W) = (1,0)$

$\mathbf{p}' = \mathbf{p} + round\{\langle K(\mathbf{p}_N) + K(\mathbf{p}_E) + K(\mathbf{p}_S) + K(\mathbf{p}_W)\rangle/4\}$

$= (3,3) + round\{\langle (0,-1) + (-1,0) + (0,1) + (1,0)\rangle/4\}$

$= (3,3) + round\{\langle (0,0)\rangle/4\}$

$= (3,3) + round\{\langle (0,0)\rangle\}$

$= (3,3) + (0,0)$

$= (3,3)$
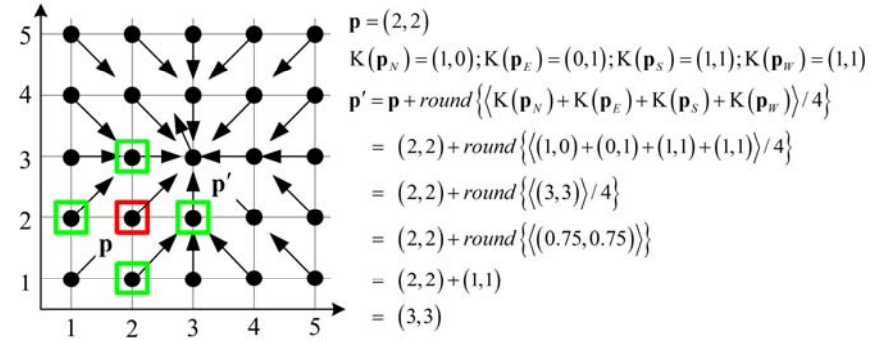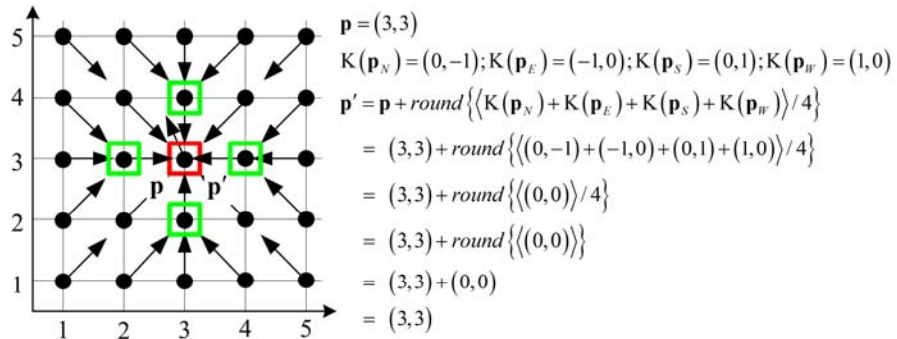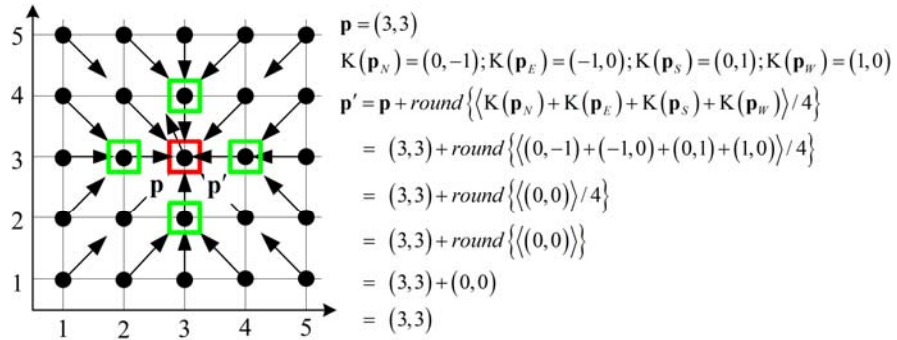
(c)

Fig. 6.3: The moving pixel finishes tracking process on **V**.

based flow tracking (DBFT)" [33] will describe the modified movement process supporting the requirement.

## 6.3 Direction-based Flow Tracking

Fig. 6.2 shows the convergence of neighborhood **V** at the destination as the red circle. It means that a moving pixel must finish the movement at this area or nearby. By measuring the convergent behavior of neighborhood **V** at a **p**, Eq. 6.1 will be modified as

$$\mathbf{p}' = \mathbf{p} + round\left\{\left\langle K\left(\mathbf{p}_N\right) + K\left(\mathbf{p}_E\right) + K\left(\mathbf{p}_S\right) + K\left(\mathbf{p}_W\right)\right\rangle / 4\right\}, \tag{6.2}$$
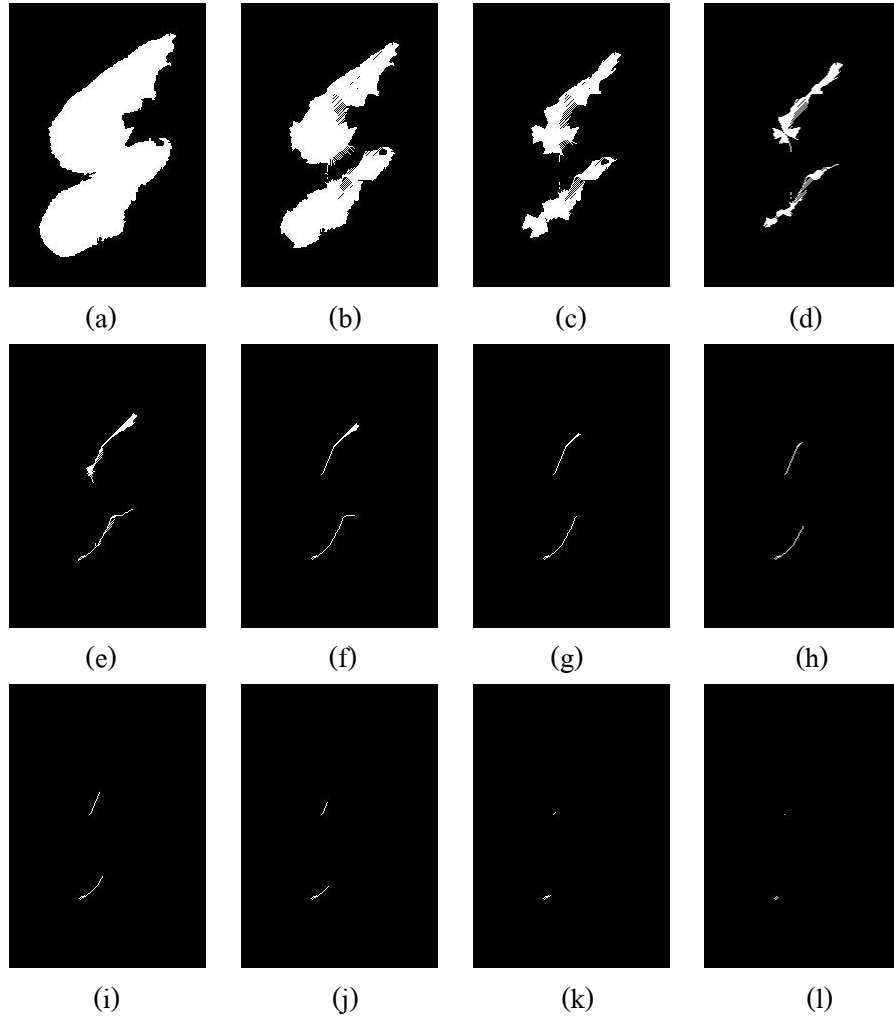


Fig. 6.4: (a)-(l) show the captured scenes of pixel tracking at $m_{loop}$ $i$ = 1, 10, 20, 30, 40, 50, 60, 70, 80, 90, 100, and 107.

where $\mathrm{K}\left(\mathbf{p}_{[N,E,S,W]}\right)$ represents a direction of neighborhood pixel of $\mathbf{p}$ at North, East, South, and West. From this way, the pixel $\mathbf{p}$ will be held when it moves to the position that the round of average $\mathrm{K}\left(\mathbf{p}_{[N,E,S,W]}\right)$ is less than one. Fig. 6.3 demonstrates how a moving pixel finishes its tracking on $\mathbf{V}$ in three times. The calculation attached in this example yields $\mathbf{p}' = \mathbf{p}$ that hold this pixel to stick on the target area. In some cases, $\mathrm{K}\left(\mathbf{p}_{[N,E,S,W]}\right)$ cannot hold $\mathbf{p}$ to finish movement because the over round of average $\mathrm{K}\left(\mathbf{p}_{[N,E,S,W]}\right)$. Therefore, the loop process number $m_{loop}$ is applied to terminate the repeated movement except the holding function from $\mathrm{K}\left(\mathbf{p}_{[N,E,S,W]}\right)$. Thus, the additional step can be expressed as process as:

**DBFT process:**

$n_{loop} = 0$

**Define** $m_{loop}$

**While** $all\left(\mathbf{p} \neq \mathbf{p}'\right)$, $n_{loop} < m_{loop}$

      **Find $\mathbf{p}'$ to all pixels in nuclei**

      **Update $\mathbf{p}$**

      $n_{loop} = n_{loop} + 1$

**End while**

**Label grouping pixel**

**Retrieve labeled pixel to original $\mathbf{p}$**

**End**

Fig. 6.4 shows the moving pixels on the overlapping nuclei where the nuclei are shown in the white area. Based on implementation of DBFT process, the pixels flow to the destination in scene by scene. It shows that when the number of iteration increases, grouped pixels are attracted to the area where the directions are convergent. At last scene in Fig. 6.4(l), it indicates the finished movement that the all pixels of an individual nucleus are grouped inside.

Subsequently, the final step of DBFT uses these pixel groups to extract the individual nuclei. By labeling and then retrieving the grouped pixels, the labeled pixels in the white dash circles of Fig.

(a)                                          (b)
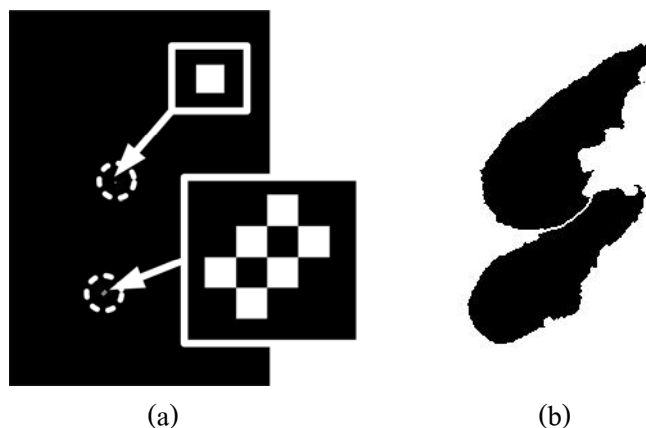
Fig. 6.5: (a) Pixel groups after tracking process. (b) Separation of nuclei after retrieving pixel

position.

6.5(a) are retrieved to the original position. Thus, the final results of the proposed algorithm are formed in the labeled image which indicates the individual nucleus by labeling number as the example shown in Fig. 6.5(b).



(a)



(b)
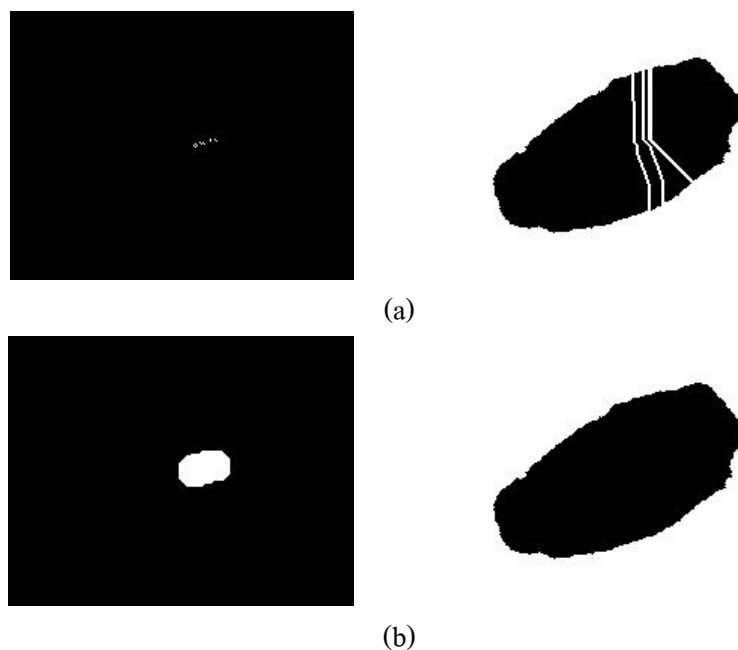
Fig. 6.6: Incomplete tracking pixel solution using dilation operator where (a) is the result of

incomplete tracking pixels and (b) is the results from applying dilation process to eliminate this

defect.
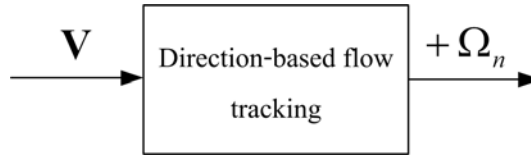
Fig. 6.7: Workflow of the proposed scheme.

However, in some cases, the incomplete tracking pixels as showed in Fig. 6.6(a)-right causes the over-segmentation. Because of unconnected pixels in the final moving step, the retrieving process will label those pixels to the individual objects illustrated in Fig. 6.6(a)-left. This defect can be simply eliminated using the basic morphology operator. It is dilation operator applying to the unconnected pixels. The achievement on this task can be showed in Fig. 6.6(b) where the results of dilation process are the left image and its retrieved pixels are the right image. Therefore, in final step of the proposed approach, the identification of the dilation structure element must be initially defined.

## 6.4 Materials and Methods

The DBFT implementation on the nuclei segmentation is only required one parameter, $m_{loop}$. It is the loop process number which is identified by $m_{loop} = 1000$. Fig. 6.7 shows the workflow of DBFT implementation on overlapping nuclei segmentation. Simply, the process has alone determination by DBFT, where the provided direction field, $\mathbf{V}$, is inputted, and the $+\Omega_n$ yields the segmented nuclei at a $m_{loop}^{th}$. To validate the performance, the experimented images are set from twenty nine nuclei images which are a variety of shapes on both individual and overlapping nuclei, and have 3600 * 2880 pixels formed in JPEG color image format. By applying the images to direction field generator as Chapter 3, the direction field, $\mathbf{V}$, is provided. Finally, the obtained $+\Omega_n$ will be compared to the gold standard from the expert. The evaluated values as corrected-over-and-under segmentation are initial factor to validate the performance when it is compared to other approaches.
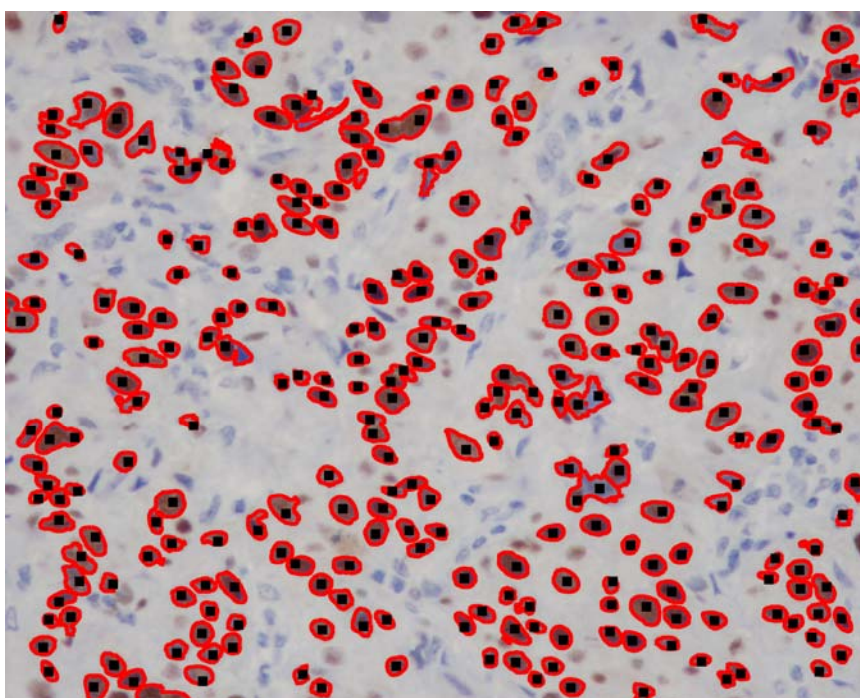
Fig. 6.8: Segmentation results (red line) with expert markers (black dot).

## 6.5 Results

From Section 6.4, the resultants under correct, over, and under segmentation are illustrated in Table 6.1 and the segmentation results in Fig. 6.8. By expert quantification, the percents of segmentation performance are calculated as 97.29 %, 5.38 %, and 1.90 %. The correct segmentation accuracy is over 90 %. The over segmentation accuracy is less than 10 %. The under segmentation accuracy is less than 5 %.

## 6.6 Discussion

The segmentation approach described in this chapter attempts to utilize essential information from direction. This is instruction that can be applied in movement of an object. As the provided direction information, a pixel will be tracked on the direction field. This operation takes a pixel in the individual nuclei to the same area or nearby. With labeling and retrieving the obtained pixel

group, the segmented nuclei can be completed as shown in the example. To validate its performance, the implementation applied to the actual nuclei images yields the results compared with the segmentation marker from the expert. The correct-over-and-under segmentations are derived from that validation. For deep analysis, the obtained results will be determined to other performance validation techniques. Also, the comparison among direction-based segmentation techniques and the traditional segmentation approaches gives more performance validation which is presented in Chapter 7.

TABLE 6.1: Quantification accuracy.

| No. | Image name | Expert | Correct | Over | Under |
|-----|------------|--------|---------|------|-------|
| 1 | T51-1549A1 | 215 | 212 | 13 | 3 |
| 2 | T51-1549A2 | 243 | 236 | 16 | 4 |
| 3 | T51-1549A3 | 269 | 261 | 10 | 5 |
| 4 | T51-1549A4 | 250 | 240 | 10 | 9 |
| 5 | T51-1549A5 | 192 | 188 | 13 | 3 |
| 6 | T51-1549A9 | 265 | 262 | 11 | 2 |
| 7 | T51-1549A12 | 229 | 224 | 4 | 2 |
| 8 | T51-1549A17 | 230 | 225 | 7 | 3 |
| 9 | T51-1549A21 | 207 | 196 | 10 | 6 |
| 10 | T51-1549A23 | 294 | 284 | 15 | 8 |
| 11 | T51-1549A36 | 204 | 198 | 8 | 2 |
| 12 | T51-1549A37 | 242 | 237 | 12 | 3 |
| 13 | T51-1549A39 | 205 | 196 | 13 | 5 |
| 14 | T51-1549A40 | 233 | 231 | 11 | 2 |
| 15 | T51-1549A41 | 167 | 162 | 12 | 4 |
| 16 | T51-1549A42 | 210 | 204 | 13 | 6 |
| 17 | T51-1549A44 | 268 | 263 | 4 | 2 |
| 18 | T51-1549A53 | 283 | 260 | 10 | 15 |
| 19 | T51-1549A54 | 259 | 250 | 11 | 7 |
| 20 | T51-1549A59 | 176 | 175 | 25 | 1 |
| 21 | T51-1549A60 | 225 | 219 | 16 | 6 |
| 22 | T51-1549A73 | 168 | 158 | 4 | 7 |
| 23 | T51-1549A78 | 201 | 200 | 7 | 1 |
| 24 | T51-1549A92 | 173 | 168 | 12 | 3 |
| 25 | T51-1549A97 | 140 | 134 | 9 | 5 |
| 26 | T51-1549A-78 | 241 | 239 | 6 | 2 |
| 27 | T51-1549A-134 | 252 | 251 | 19 | 1 |
| 28 | T51-1549A-135 | 227 | 224 | 11 | 2 |
| 29 | T51-1549A-149 | 107 | 105 | 31 | 2 |
| | Sum | 6375 | 6202 | 343 | 121 |

# Chapter 7

# Performance Comparisons

## 7.1 Introduction

According to nuclei segmentation task, the segmentation accuracy is usually represented as the quantification value, correct, over, and under segmentation. In evaluation, the marker marked by the expert is set to be the gold standard compared to the results from segmentation approach. However, this assessments show the conclusion roughly and indistinctly under the basic calculation. This may cause the lack of performance comparison with the traditional techniques. To overcome this problem, some previous works [1], [36]-[39] propose deep analysis for measuring of performance comparisons. From the fact that the segmentation approach performs as the classifier in detecting the individual nucleus, the derived correct, over, and under values can be applied to measure performance comparisons correspondingly as following descriptions in this chapter.

The organization of this chapter is as follows. Section 7.2 describes the basic of performance measurement for validating the segmentation accuracy. The experiment method in Section 7.3 explains the procedure to obtain the segmentation value from proposed segmentation algorithms in Chapter 4-6 (DSMT, DBCT, and DBFT), tradition watershed (TWS), and marker-controlled watershed (MCWS). The performance evaluations as sensitivity (SS), positive predictive value (PPV), accuracy (ACC) and $F_1$-measure are calculated based on the basic segmentation evaluations as correct, over, and under segmentation value. The results are shown in Section 7.4 where the discussion is also given.

TABLE 7.1: A confusion matrix from two classifiers.

| | | Predicted Class | |
|---|---|---|---|
| | | Positive (+) | Negative (-) |
| Actual Class | Positive (+) | True Positive (TP) | False Negative (FN) |
| | Negative (-) | False Positive (FP) | True Negative (TN) |

## 7.2 Classifier Performance Measurement

Table 7.1 shows the possible cases of classifier results, where the predicted class is defined to classifier results compared to the actual class which is the gold standard from the expert. The table details the comparison results between two classifiers to four possible cases. First, when the sample is decided to positive by expert (actual class) and also in the classifier (predicted class), this same decision is called true positive (TP). If both operators decide a sample to be the negative, it is called true negative (TN). If the expert and the classifier make the opposite, false positive (FP) and false negative (FN) are applied in these situations.

Based on the descriptions of the basic measurements above, the correct, over, and under segmentation are equivalent to TP, FP, and FN, respectively. However, the performance can be measured distinctly to specific validation based on these items as shown in Table 7.2. The specific validations give more description of classifier performance and can be explain to some characteristic as following.

TABLE 7.2: The description of classifier performance item.

| Performance measurement | Solution | Description |
|---|---|---|
| True positive rate<br><br>or Hit rate<br><br>or Recall<br><br>or Sensitivity or TP rate | $\dfrac{TP}{P}$ | The ratio of the corrected-segmentation by classifier to positive marker by expert |
| False positive rate<br><br>or False alarm rate<br><br>or FP rate | $\dfrac{FP}{N}$ | The ratio of the over - segmentation by classifier to negative marker by expert |
| False negative rate<br><br>or FN rate | $\dfrac{FN}{P}$ | The ratio of the under - segmentation by classifier to positive marker by expert |
| Precision<br><br>or Positive predictive value | $\dfrac{TP}{(TP+FP)}$ | The probability that the classifier yields really positive |
| $F_1$-measure | $2/\left(\dfrac{1}{TP\ rate}+\dfrac{1}{Precision}\right)$ | The combination of TP rate and Precision |
| Accuracy<br><br>or Predictive accuracy | $\dfrac{TP+TN}{TP+TN+FP+FN}$ | The probability that the classifier yields correctly segmentation |

**The complete classifier:** It describes the classifier that can similarly perform as the expert. The errors are zero. It will subsequently yield $TP = P$ and $TN = N$. The results calculated later are found SS = 1, FP Rate = 0, PPV = 1, $F_1$-measure = 1, and ACC = 1.

**The worst classifier:** This case yields $TP = 0$ and $TN = 0$. The calculated performance measurements are SS = 0, FP Rate = 1, PPV = 0, $F_1$-measure does not exist, and ACC = 0.

TABLE 7.3: A confusion matrix from two classifiers.

| Confusion matrix values | | |
|---|---|---|
| Case 1 | Case 2 | Case 3 |
| TP = 8,000 | TP = 80,000 | TP = 8,000 |
| FN = 2,000 | FN = 20,000 | FN = 2,000 |
| TN = 7,000 | TN = 7,000 | TN = 70,000 |
| FP = 3,000 | FP = 3,000 | FP = 30,000 |
| Measurements | | |
| TP rate = 0.8 | TP rate = 0.8 | TP rate = 0.8 |
| FN rate = 0.2 | FP rate = 0.2 | FP rate = 0.2 |
| TN rate = 0.7 | TN rate = 0.7 | TN rate = 0.7 |
| FP rate = 0.3 | FN rate = 0.3 | FN rate = 0.3 |
| Acc = 0.75 | Acc = 0.7909 | Acc = 0.7091 |

**The ultra-liberal classifier:** This characteristic emerges when the classifier only yields the positive class. This gives $SS = 1$ and FP Rate $= 1$ in the same time. The subsequent results from this characteristic are PPV $= P/(P+N)$, $F_1$-measure $= 2 \times P/(2 \times P + N)$, and ACC $= P/(P+N)$.

**The ultra-conservative classifier:** In case of the classifier that only the negative class is deter-mined, this characteristic will result both $FP = 0$ and $TP = 0$. Moreover, other measurements are $SS = 0$, FP rate $= 0$, PPV and $F_1$-measure do not exist, and ACC $= N/(P+N)$.

Other interesting characteristic is the calculated measurement values that have their variation based on samples. It is obviously concluded as following example shown in Table 7.3 where the case 1 is the initial value from the confusion matrix. Case 2 increases ten times of TP and FN and, also, case 3 for TN and FP. The variation of measurement values of these three cases are demonstrated with the true and false positive rates, the true and false negative rates, and the accuracy. Results show that the TP and FP rates and the TN and FN rates do not change in second
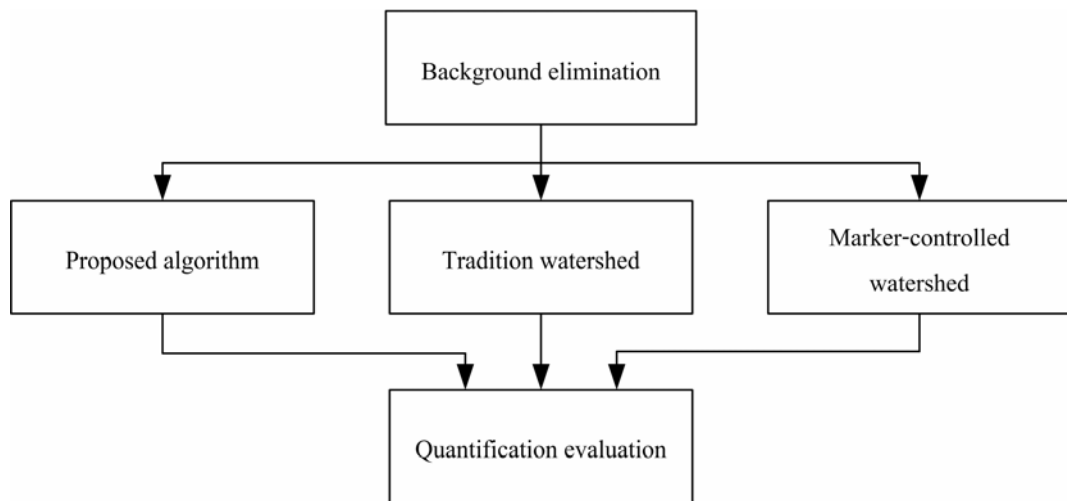
Fig. 7.1: Experimental work flow.

and third cases. In other words, the rates on TP, FP, TN and FN are independent from the number of samples. This is different from the accuracy when it varies from 0.7091 to 0.75.

## 7.3 Experiments

**Materials:** To validate the performance of the proposed algorithms, this experiment applied the DSMT, DBCT, and DBFT to the nuclei images and evaluated the quantification accuracy compared to the TWS and MCWS. Their appearances obviously present a variety of shapes on both individual and overlapping nuclei. The twenty nine images applied to this task have size 3600 x 2880 pixels formed in JPEG color image format.

**Methods:** The experimental methodology is set as the workflow shown in Fig. 7.1. The background elimination in the initial step is assigned to prepare the binary image to extract the nuclei area. This step uses the Otsu thresholding [40] which is performed on the intensity image from color space transformation. The tiny pieces in the obtained binary image are removed. Then, the resulting objects are performed with a fill hole operation to complete nuclei area. To avoid the segmentation error from the background elimination, the binary images provided to segmentation

algorithms will not consider the binary nuclei which are not marked by the expert. This terminates the error of the incorrect foreground from the background elimination step.

For assessment, we choose the TWS [41] for comparing with our algorithm. Even its over-segmentation problem mainly reduces the segmentation accuracy; it is usually implemented due to its simple adaptation. By preparing the catchment basin accurately, the over-segmentation can be reduced. In this experiment, the Euclidean distance transformation is initially performed to build the catchment basin. Certainly, the local minima from the irregular shape of nuclei are the source of over-segmentation. To alleviate this problem, the intensity image filter is assigned to wipe out local minima before its operation. Moreover, the MCWS [42] is another selection to be compared to our approach from its advantage in over-segmentation controlling. Its marker identification is performed based on the cooperation of morphology operators. It yields the markers, which are adopted to build the catchment basins for watershed process.

The final step of this experiment is the quantification evaluation. This assessment yields the correct, over, and under segmentation resulting from the comparisons with the markers from an expert. In addition to the general assessment, we validate the performance of DSMT, DBCT, DBFT, TWS, and MCWS using sensitivity (SS) [1], [36]-[39] positive predictive value (PPV) [1], [36]-[39], accuracy (ACC) [43], and $F_1$-measure [1]. These values are used to describe the performance outcome in detection system. The SS indicates the possibility that the system can correctly detect nuclei compared with the gold standard. The SS calculation is given by

$$SS = TP/(TP + FN) \tag{7.1}$$

where TP is number of correct segmentation by the algorithm, and FN is the number of nuclei, which are not marked by an algorithm but marked by the gold standard. On the other hand, the PPV is the probability that the detection of a nucleus is actually associated with a nucleus marked by the expert, which is given by

$$PPV = TP/(TP + FP) \tag{7.2}$$

where FP is the number of nuclei which are not marked by the gold standard but are detected in the segmented nuclei from the algorithm. Furthermore, the combination of SS and PPV yields the summarized performance evaluation where the accuracy and $F_1$-measure are determined in the following forms:

$$\text{ACC} = \frac{\text{TP+TN}}{\text{TP+TN+FP+FN}}$$  (7.3)

and

$$F_1 = 2 \Big/ \left( \frac{1}{\text{PPV}} + \frac{1}{\text{SS}} \right).$$  (7.4)

Note that the TN is set to zero when ACC is determined.

## 7.4 Results and Discussion

In this section, we firstly describe the characteristics of derived direction field resulting from the direction generator. The description on smoothing-and-contrasting direction abilities is observed from the direction fields compared with the gradient direction of smoothed distance image. Moreover, the segmented nuclei are extracted from these direction fields using DBFT. Secondly, the segmentation accuracy is presented to validate the performance of the direction-based approaches (DSMT, DBCT, and DBFT) compared to other techniques, i.e., the TWS and MCWS.

**Direction Characteristics:** According to the direction requirement, the smoothing-and-contrasting direction abilities are the keys that determine the segmentation boundary. In direction environment, both abilities are obviously observed by direction field shown in Fig. 7.2. The direction field from the direction generator in Fig. 7.2(a) is compared to that from the gradient direction of smoothed distance image in Fig. 7.2(b) on both abilities. The decision area for the segmentation of overlapping objects is located in the rectangular box. In addition, it is zoomed out and shown in the right image.
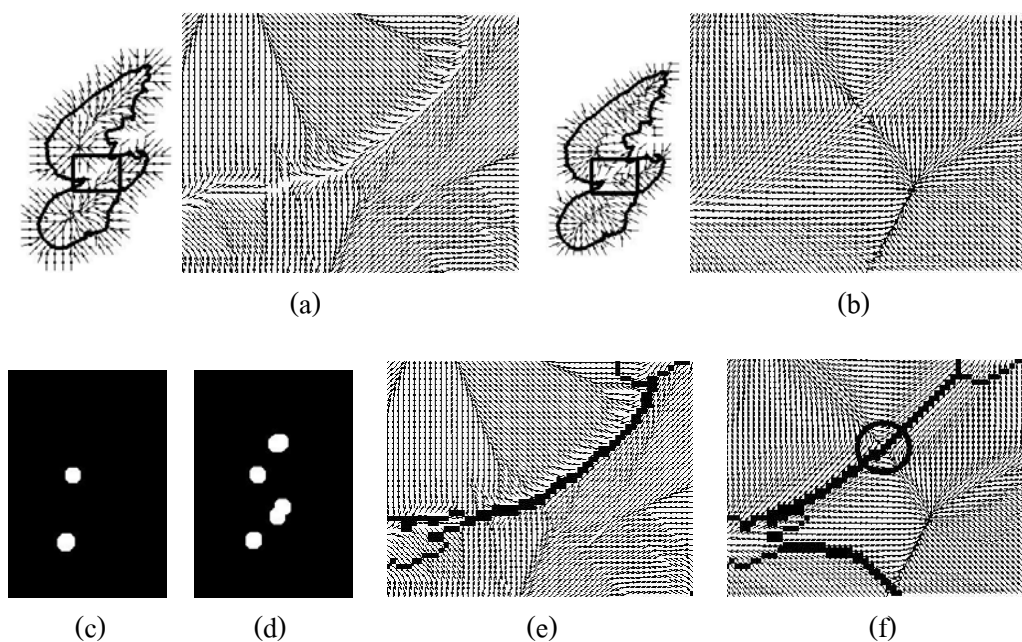
Fig. 7.2: Comparisons of direction field characteristics from the direction-based approaches (DSMT, DBCT, and DBFT) with those of the gradient direction of smoothed distance image. (a) Direction field from the direction generator. (b) Direction field from gradient direction of smoothed distance image. (c) Pixel groups using direction field in (a) from DBFT approach. (d) Pixel groups using direction field in (b) from DBFT approach. (e) Segmentation boundary from DBFT approach of (a). (f) Segmentation boundary from DBFT approach of (b).

For smoothing direction ability, the direction field of the direction generator seems to be more confusing than the gradient direction of smoothed distance image. Nevertheless, it can be still tracked by a pixel to the area representing the individual nucleus as shown in Fig. 7.2(c). This means that the direction smoothness from the direction-based approaches can maintain the tracking ability that guides all pixels in an individual nucleus to the same area or nearby. This occurring behavior illustrates the characteristics of direction field corresponding to the definition of proposed concept sufficiently. On the other hand, the direction field from the gradient direction of smoothed distance image cannot achieve the correct tracking as illustrated in Fig. 7.2(d).

In case of contrasting direction ability, it is important for tracking process since the segmentation decision is initially formed by this factor. From Fig. 7.2(a), our approach responds to this

requirement very well as can be seen by distinct divergent directions. Its contrast directions are throughout on the segmentation decision continuously. This ensures that the initial tracking process can extract the segmentation line. Fig. 7.2(e) shows the boundary pixels after completing segmentation on the direction field. The segmentation boundary throughout appears at the contrasting direction. Fig. 7.2(f) shows the segmentation boundary resulting from the direction field of the gradient direction of smoothed distance image. Although it looks similar to the result from direction generator, some are yield local-convergent-and-divergent direction field as shown in the black dash circle of Fig. 7.2(f). This may cause wrong tracking pixels.

**Quantitative evaluation:** Table 7.4 shows the comparison of quantification accuracy among the experimented segmentation algorithms. Twenty nine images consisting of 6,375 nuclei were tested. The nuclei number of TP, FP, and FN are shown and summarized to the total number and the percent in each column. The ideal numbers for TP, FP, and FN percents are 100, 0, and 0, respectively. The percent of correct segmentation from the DSMT, DBCT, DBFT, TWS, and MCWS are 92.08, 96.83, 97.29, 98.89, and 95.97, respectively. The TWS give the highest percent of TP at an expense of significant loss in FP number. In other words, the percent of FP given by the TWS is 20.09, which is worse than the others. The result from the MCWS, which is the watershed improvement for over segmentation problem, is 9.52%. However, the DSMT provides the best FP percent at 3.12. The TWS gives the best FN percent at 0.97 due to it's over segmentation characteristics. The FN percent from the DBFT is 1.90, which is better than that from the MCWS at 3.34%.

TABLE 7.4: Comparison of segmentation accuracy.

| Image No. | DSMT | | | DBCT | | | DBFT | | | TWS | | | MCWS | | |
|---|---|---|---|---|---|---|---|---|---|---|---|---|---|---|---|
| | TP | FP | FN | TP | FP | FN | TP | FP | FN | TP | FP | FN | TP | FP | FN |
| 1 | 201 | 9 | 12 | 212 | 19 | 2 | 212 | 13 | 3 | 214 | 57 | 1 | 206 | 24 | 7 |
| 2 | 228 | 9 | 11 | 236 | 25 | 3 | 236 | 16 | 4 | 240 | 55 | 3 | 236 | 23 | 6 |
| 3 | 243 | 1 | 21 | 260 | 15 | 5 | 261 | 10 | 5 | 268 | 38 | 1 | 261 | 24 | 7 |
| 4 | 226 | 2 | 22 | 238 | 16 | 8 | 240 | 10 | 9 | 243 | 67 | 6 | 232 | 17 | 17 |
| 5 | 177 | 11 | 14 | 186 | 22 | 1 | 188 | 13 | 3 | 190 | 39 | 0 | 183 | 15 | 7 |
| 6 | 251 | 5 | 13 | 262 | 15 | 3 | 262 | 11 | 2 | 263 | 32 | 2 | 258 | 12 | 6 |
| 7 | 219 | 2 | 7 | 224 | 11 | 2 | 224 | 4 | 2 | 228 | 17 | 1 | 224 | 9 | 2 |
| 8 | 219 | 3 | 9 | 225 | 11 | 2 | 225 | 7 | 3 | 228 | 33 | 2 | 225 | 12 | 4 |
| 9 | 186 | 5 | 19 | 194 | 17 | 6 | 196 | 10 | 6 | 202 | 47 | 4 | 198 | 19 | 8 |
| 10 | 268 | 7 | 22 | 281 | 22 | 8 | 284 | 15 | 8 | 288 | 50 | 5 | 280 | 22 | 13 |
| 11 | 194 | 4 | 7 | 199 | 13 | 3 | 198 | 8 | 2 | 203 | 35 | 1 | 200 | 21 | 3 |
| 12 | 221 | 8 | 15 | 234 | 17 | 3 | 237 | 12 | 3 | 240 | 33 | 2 | 235 | 20 | 6 |
| 13 | 185 | 6 | 17 | 197 | 15 | 4 | 196 | 13 | 5 | 201 | 34 | 2 | 191 | 21 | 13 |
| 14 | 218 | 6 | 14 | 231 | 18 | 1 | 231 | 11 | 2 | 232 | 44 | 1 | 229 | 20 | 4 |
| 15 | 140 | 7 | 23 | 162 | 22 | 3 | 162 | 12 | 4 | 165 | 43 | 2 | 149 | 17 | 17 |
| 16 | 191 | 9 | 14 | 205 | 16 | 5 | 204 | 13 | 6 | 207 | 45 | 3 | 196 | 25 | 11 |

TABLE 7.4: Comparison of segmentation accuracy (Cont.).

| Image | DSMT | | | DBCT | | | DBFT | | | TWS | | | MCWS | | |
|---|---|---|---|---|---|---|---|---|---|---|---|---|---|---|---|
| No. | TP | FP | FN | TP | FP | FN | TP | FP | FN | TP | FP | FN | TP | FP | FN |
| 17 | 252 | 3 | 13 | 262 | 8 | 2 | 263 | 4 | 2 | 264 | 55 | 3 | 258 | 31 | 9 |
| 18 | 237 | 9 | 35 | 256 | 21 | 14 | 260 | 10 | 15 | 280 | 64 | 3 | 267 | 27 | 12 |
| 19 | 238 | 7 | 15 | 250 | 17 | 6 | 250 | 11 | 7 | 258 | 50 | 1 | 246 | 26 | 8 |
| 20 | 162 | 17 | 10 | 174 | 32 | 1 | 175 | 25 | 1 | 174 | 59 | 1 | 170 | 26 | 6 |
| 21 | 210 | 10 | 12 | 220 | 24 | 4 | 219 | 16 | 6 | 221 | 67 | 4 | 213 | 31 | 11 |
| 22 | 151 | 3 | 14 | 152 | 13 | 7 | 158 | 4 | 7 | 162 | 20 | 6 | 154 | 12 | 9 |
| 23 | 185 | 6 | 14 | 197 | 11 | 1 | 200 | 7 | 1 | 201 | 32 | 0 | 196 | 20 | 2 |
| 24 | 162 | 10 | 9 | 166 | 15 | 3 | 168 | 12 | 3 | 173 | 21 | 0 | 166 | 17 | 5 |
| 25 | 126 | 4 | 12 | 135 | 11 | 4 | 134 | 9 | 5 | 137 | 17 | 3 | 135 | 16 | 4 |
| 26 | 232 | 2 | 7 | 238 | 11 | 1 | 239 | 6 | 2 | 239 | 38 | 2 | 240 | 9 | 1 |
| 27 | 239 | 12 | 12 | 250 | 32 | 1 | 251 | 19 | 1 | 251 | 53 | 1 | 248 | 24 | 4 |
| 28 | 212 | 9 | 11 | 223 | 20 | 2 | 224 | 11 | 2 | 226 | 66 | 1 | 223 | 26 | 3 |
| 29 | 97 | 13 | 10 | 104 | 30 | 3 | 105 | 31 | 2 | 106 | 70 | 1 | 99 | 41 | 8 |
| Sum | 5870 | 199 | 414 | 6173 | 519 | 108 | 6202 | 343 | 121 | 6304 | 1281 | 62 | 6118 | 607 | 213 |
| Percent | 92.08 | 3.12 | 6.49 | 96.83 | 8.14 | 1.69 | 97.29 | 5.38 | 1.90 | 98.89 | 20.09 | 0.97 | 95.97 | 9.52 | 3.34 |

TABLE 7.5: Comparison of segmentation accuracy with respect to SS (sensitivity), PPV (positive predictive value), ACC (accuracy), and $F_1$ ( $F_1$-measure).
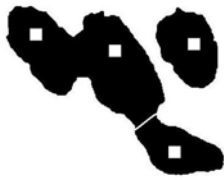
|        | DSMT  | DBCT  | DBFT  | TWS   | MCWS  |
|--------|-------|-------|-------|-------|-------|
| SS     | 0.934 | 0.983 | 0.981 | 0.990 | 0.966 |
| PPV    | 0.967 | 0.922 | 0.948 | 0.831 | 0.910 |
| ACC    | 0.905 | 0.908 | 0.930 | 0.824 | 0.882 |
| $F_1$  | 0.950 | 0.952 | 0.964 | 0.904 | 0.937 |

Table 7.5 shows more quantitative comparisons on SS, PPV, ACC, and $F_1$ values resulting from all algorithms. The DBFT has high detection performances on both SS and PPV values at 0.981 and 0.948, respectively. These values are better than those from the MCWS, which are 0.966 and 0.910, respectively. These values are better than those from the TWS and MCWS, which are over 0.960 and 0.830, respectively. For the TWS, it gives very good SS value at 0.990 with the tradeoff in low PPV value at 0.831. By combination of SS and PPV, the ACC of DBFT is highest at 0.930 while the ACC of DSMT, DBCT, TWS and MCWS are 0.905, 0.908, 0.824, and 0.882 respectively. Similarly, the $F_1$ value of DBFT is also highest at 0.964 compared to those from the DSMT, DBCT, TWS and MCWS at 0.950, 0.952, 0.904 and 0.937, respectively.

Table 7.6 shows the segmentation characteristics of all algorithms using the labeled objects compared to the square dots, which are marked by the expert. Image set No. 1 shows the incomplete segmentation from the MCWS. This under segmentation is the effect of over segmentation controlling under failed marker identification. Image set No. 2 illustrates the over segmentation of the TWS, which is generally caused by the imperfect catchment basin generation. In addition, the segmentation results of irregular shape nuclei in the image set No. 3 represent the disturbance to both the TWS and MCWS.

For the direction-based approaches (DSMT, DBCT, and DBFT) on overlapping nuclei segmentation, the proposed approach requires the direction characteristics that are the smoothing direction ability on individual nucleus area and the contrasting direction ability on overlapping nuclei area.

TABLE 7.6: Comparison of segmented overlapping nuclei.

| No. | Direction-based approach | TWS | MCWS |
|-----|--------------------------|-----|------|
| 1 |  |  |  |
| 2 |  |  |  |
| 3 |  |  |  |

The quantitative results show that the percent of correct, over, and under segmentation from the direction-based approaches are better than those from the MCWS. Based on ACC and $F_1$ values, the DBFT can be considered as the best among five methods because it provides the highest numbers. Moreover, the DBFT is more robust when applied to the irregular shape nuclei.

# Chapter 8

# Conclusions and Future Work

## 8.1 Conclusions

This thesis has proposed the technique based on direction of image data applying to overlapping nuclei segmentation. The advantages of direction are determined thorough in almost aspect. Relation, difference, and path as shown in Fig. 8.1 are keywords of direction utilization in this research. Reasonably, these concepts can perform the connection between direction information and segmentation task as the following definitions:

**Relation:** if the considered directions of any pixels of overlapping nuclei image can be decomposed to a direction group based on any characteristics, these pixels can be possibly merged into the individual nucleus.

**Difference:** if any pixels of overlapping nuclei image have the angle differences over the thresholding value, the segmented boundaries can be extracted from them.
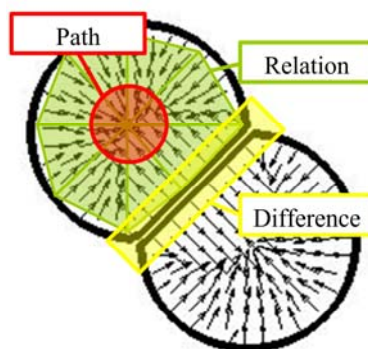


Figure 8.1: Basic concepts of direction-based application to overlapping nuclei segmentation.

**Path:** if any considered directions of overlapping nuclei segmentation guide any pixels to same area or nearby, these directions can be extracted to the individual nucleus.

Fig. 8.1 shows explicitly how the proposed concepts perform on direction information. However, the original image does not prepare the direction information. Hence, similarly to general data signal processing, the pre-processing scheme is set to generate the direction information from overlapping nuclei image. The characteristics of direction are required especially to the perfect direction field in order to handle segmentation accuracy. Thus, this work firstly introduces the pre-processing step, as follows.

**Direction generator:** Two goals of this scheme are how to generate the direction field and how to hold the desirable properties of direction field as much as possible. Before performing to achieve these tasks, the direction generator requires the image pre-processing to prepare binary image yielding nuclei shape. The tradition image processing techniques consisting of color space transformation, binarizations, and morphology operator, are selected due to their effective performance, flexibility, and cost. Then, direction generator will construct the direction field using the gradient calculation from distance transformation. For the second goal, the direction smoothing ability and contrasting direction ability are desirable and significant properties. Hence, in process, the direction generator adapts the distance transformation in global to the distance transformation in local. Using iterative process that shrinks the binary image and then calculates the distance image, the local direction field can be generated and carried out both significant direction abilities from all of this process. The direction field from this process can be subsequently used in segmentation approaches that employ the basic concepts, relation, difference, and path, to succeed overlapping nuclei segmentation. Three segmentation approaches based on the generated direction field are proposed in this thesis. Their details are as follows.

**Direction-based splitting and merging technique (DSMT):** This technique interprets the relation to the direction in the individual nuclei attempting to direct to the same area or nearby in the individual nuclei area. There are two step of this technique as splitting and merging steps. The splitting step separates whole pixels in direction field into tiny pieces using angle range. The

relation among these tiny pieces is calculated. The merging condition can be found using the algorithm based on angle measurement. After merging process, the individual nucleus will be obtained. In other words, the overlapping nuclei are separated into individual nucleus.

**Direction-based classification technique (DBCT):** Difference in direction field is explicitly at the boundaries between the overlapping nuclei under divergent characteristic. It can be estimated using difference angle value of four neighbor directions around a considered direction. The obtained value will be classified to prove that it has divergent characteristic or not. If it is true, whole pixels having this characteristic will be extracted to the single boundaries. By superimposing it on the overlapping nuclei image, the segmented nuclei will be succeeded finally.

**Direction-based flow tracking technique (DBFT):** Path is basically characteristic in direction field. Tracking based on the path can group any pixels in the individual nucleus under direction characteristic produced by direction generator. The derived pixel group will be labeled and then recovered to the original position before tracking. Hence, finally, the separation of overlapping nuclei into the individual nucleus can be achieved.

**Segmentation accuracy:** The results of this research are derived from the experiment on real overlapping nuclei image. The proposed approaches and the tradition segmentation approaches (TWS and MCWS) are tested to yield correct, over, and under segmentation value. This quantification is not sufficient until the deep validations as SS, PPV, ACC and $F_1$ are determined. The high SS and PPV of direction-based algorithms, over 0.9, indicate the significant performance under actual operation. Especially the ACC and $F_1$, show that DBFT is the best among compared approaches.

## 8.2 Future work

In summary, this work gives more viewpoint of direction application on overlapping nuclei segmentation. There are three strategies proposed on segmentation approaches. However, more efficiency on this task can be developed in future until two ideals as following are fulfilled.

**Direction preparing:** The direction generator proposed in this work can be added more individual nucleus information in addition to nuclei shape. Color, texture, and edge are the examples of this. However, problems of this application are how to transform this information to direction field and how to arrange the obtained direction to have the designed characteristic. The solution may be resulted from N-dimension space calculation similar to the direction generator using binary image in direction field estimation.

**Segmentation approach:** The segmentation approaches in this thesis are based on the general computation in a direction. In each step, the computation only uses some ability of direction that is local characteristic of a direction such as relation, difference, and path. Question is that can the computation estimate globally to extract group of direction having same characteristic similar to the frequency domain done in image filter process. If this is succeeded, accuracy, robustness, and cost may be improved.

**Direction-based classification technique (DBCT):** This approach can be improved to achieve better performance by removing correction process of $\omega$. In this case, the $\omega$ determination may use trigonometric function to avoid overflow problem of $\omega$ calculation.

**Direction-based flow tracking technique (DBFT):** The dilation after finished tracking process is employed to connect moving pixel groups together. This step may use marker to indicate area to connect moving pixel groups before finished tracking process.

**Cooperation of DSMT and DBFT:** To reduce processing time of DBFT, the tracking process can use splitting process of DSMT to move only direction agent of each split direction field. Subsequently, DBFT will decide to group split direction field and then extract the individual nucleus using DSMT.

# BIBLIOGRAPHY

[1]     B. Fang, W. Hsu, and M. Lee, "On the accurate counting of tumor cells*," IEEE Trans. Nanobiosci.*, vol. 2, no. 2, pp. 94-103, 2003.

[2]     S. Petushi, C. Katsinis, C. Coward, F. Garcia, and A. Tozeren, "Automated identification of microstructures on histology slides," *IEEE International Symposium on Biomedical Imaging: Macro to Nano*, vol. 1, pp. 424-427, 2004.

[3]     J. P. Thiran and B. Macq, "Morphological feature extraction for the classification of digital images of cancerous tissues," *IEEE Trans. Biomed. Eng.*, vol. 43, no. 10, pp.  1011-1020, 1996.

[4]     L. O'Gorman, A. C. Sanderson, and K. P. Jr., "A system for automated liver tissue image analysis: methods and results," *IEEE Trans. Biomed. Eng.*, vol. 32, no. 9, pp. 696-706, 1985.

[5]     C. Jung and C. Kim, "Segmenting clustered nuclei using h-minima transform-based marker extraction and contour parameterization," *IEEE Trans. Biomed. Eng.*, vol. 57, no. 10, pp. 2600-2604, 2010.

[6]     J. Cheng and J. C. Rajapakse, "Segmentation of clustered nuclei with shape markers and marking function," *IEEE Trans. Biomed. Eng.*, vol. 56, no. 3, pp. 741-748, 2009.

[7]     S. Svensson, "Aspects on the reverse fuzzy distance transform," *Pattern Recognition Letters*. vol. 29, pp. 888-896, 2008.

[8]     O. Schmitta, and M. Hasse, "Radial symmetries based decomposition of cell clusters in binary and gray," *Pattern Recognition*., vol. 41, pp. 1905-1923, 2008.

[9]     Q. Yang and B. Parvin, "Harmonic cut and regularized centroid transform for localization of subcellular structures," *IEEE Trans. Biomed. Eng.*, vol. 50, no. 4, pp. 469-475, 2003.

[10] F. Raimondo, M. A. Gavrielides, G. Karayannopoulou, K. Lyroudia, I. Pitas, and I. Kostopoulos, "Automated evaluation of her-2/neu status in breast tissue from fluorescent in situ hybridization images," *IEEE Trans. Image Process.*, vol. 14, no. 9, pp. 1288-1299, 2005.

[11] K. Z. Mao, P. Zhao, and P.-H. Tan, "Supervised learning-based cell image segmentation for p53 immunohistochemistry," *IEEE Trans. Biomed. Eng.*, vol. 53 no. 6, pp. 1153-1163, 2006.

[12] X. Yang, H. Li, and X. Zhou, "Nuclei segmentation using marker-controlled watershed, tracking using mean-shift, and kalman filter in time-lapse microscopy," *IEEE Trans. Circuits Syst. I, Reg. Papers*, vol. 53, no. 11, pp. 2405-2414, 2006.

[13] X. Chen, X. Zhou, and S. T. C. Wong, "Automated segmentation, classification, and tracking of cancer cell nuclei in time-lapse microscopy," *IEEE Trans. Biomed. Eng.*, vol. 53, no. 4, pp. 762-766, 2006.

[14] X. Zhou, F. Li, J. Yan, and S. T. C. Wong, "A novel cell segmentation method and cell phase identification using markov model," *IEEE Transactions on Information Technology in Biomedicine*, Vol. 13, no. 2, pp. 152-157, 2009.

[15] L. He, Z. Peng, B. Everding, X. Wang, C. Y. Han, K. L. Weiss, and W. G. Wee, "A comparative study of deformable contour methods on medical image segmentation," *Image and Vision Computing*, Vol. 26, pp. 141-163, 2008.

[16] M. Kass, A. Witkin, and D. Terzopoulos, "Snakes: active contour models," *International Journal of Computer Vision*, vol. 1, no. 4, pp. 321-331, 1988.

[17] R. Malladi, J. A. Sethian, and B. C. Vemuri, "Shape modeling with front propagation: a level set approach," *IEEE Trans. Pattern Anal. Mach. Intell.*, vol. 17, no. 2, pp. 158-175, 1995.

[18] C. Zimmer, E. Labruyère, V. Meas-Yedid, N Guillén, and J.-C. Olivo-Marin, "Segmentation and tracking of migrating cells in videomicroscopy with parametric active contours: a tool for cell-based drug testing," *IEEE Trans. Med. Imag.*, vol. 21, no. 10, pp. 1212-1221, 2002.

[19] P.S. Umesh Adiga, "Segmentation of volumetric tissue images using constrained active contour models," *Computer Methods and Programs in Biomedicine*, vol. 71, pp. 91-104, 2003.

[20] H. Cai, X. Xu, J. Lu, J. W. Lichtman, S.P. Yung, and S. T.C. Wong, "Repulsive force based snake model to segment and track neuronal axons in 3d microscopy image stacks," *NeuroImage*, vol. 32, pp. 1608-1620, 2006.

[21] J. Park and J. M. Keller, "Snakes on the watershed," *IEEE Trans. Pattern Anal. Mach. Intell.*, vol. 23, no. 10, pp. 1201-1205, 2001.

[22] C. Zimmer and J.-C. Olivo-Marin, "Coupled parametric active contours," *IEEE Trans. Pattern Anal. Mach. Intell.*, vol. 27, no. 11, pp. 1838-1842, 2005.

[23] G. Xiong, X. Zhou, and L. Ji, "Automated segmentation of drosophila rnai fluorescence cellular images using deformable models," *IEEE Trans. Circuits Syst. I, Reg. Papers*, vol. 53, no. 11, pp. 2415-2424, 2006.

[24] P. Yan, X. Zhou, M. Shah, and S. T. C. Wong, "Automatic segmentation of high-throughput rnai fluorescent cellular images," *IEEE Transactions on Information Technology in Biomedicine*. vol. 12, no. 1, pp. 109-117, 2008.

[25] T. Wurflinger, J. Stockhausena, D. Meyer-Ebrechta, and A. Bocking, "Robust automatic coregistration, segmentation, and classification of cell nuclei in multimodal cytopathological microscopic images," *Computerized Medical Imaging and Graphics*, vol. 28, pp. 87-98, 2004.

[26] T. W. Nattkemper, H. Wersinga, W. Schubertb, and H. Rittera, "A neural network architecture for automatic segmentation of fluorescence micrographs," *Neurocomputing*, vol. 48, pp. 357-367, 2002.

[27] D. Yu, T. D. Pham, and X. Zhou, "Analysis and recognition of touching cell images based on morphological structures," *Computers in Biology and Medicine*, vol. 39, pp. 27-39, 2009.

[28] H.-S. Wu, J. Barba, and J. Gil, "A parametric fitting algorithm for segmentation of cell images," *IEEE Trans. Biomed. Eng.*, vol. 45, no. 3, pp. 400-407, 1998.

[29] G. Li, T. Liu, J. Nie, L. Guo, J. Chen. J. Zhu, W. Xia, A. Mara, S. Holley, and S. T.C. Wong, "Segmentation of touching cell nuclei using gradient flow tracking," *Journal of Microscopy*, vol. 231, no. 1, pp. 47-58, 2008.

[30] C. Jung, C. Kim, S. W. Chae, and S. Oh, "Unsupervised segmentation of overlapped nuclei using bayesian classification," *IEEE Trans. Biomed. Eng.*, vol. 57, no. 12, pp. 2825-2832, 2010.

[31] H. Masmoudi, , S. M. Hewitt, N. Petrick, K. J. Myers, and M. A. Gavrielides, "Automated quantitative assessment of her-2/neu immunohistochemical expression in breast cancer," *IEEE Trans. Biomed.*, vol. 28, no. 6, pp. 916-925, 2009.

[32] A. I. Borisenko and I. E. Tarapov, *Vector and Tensor Analysis with Applications*, New York, Dover Publication, 1979.

[33] Y. Surut and P. Phukpattaranont, "Overlapping nuclei segmentation using direction-based flow tracking," *IEEJ Transactions on Electrical and Electronic Engineering*, vol. 8, no. 4, pp. 387-394, 2013.

[34] Y. Surut, and P. Phukpattaranont, "Overlapping cell image segmentation using surface splitting and surface merging algorithms," in *Proceedings of the Second APSIPA Annual Summit and Conference*, Singapore, 2010, pp. 662-666.

[35] Y. Surut and P. Phukpattaranont, "Preliminary results of connected object segmentation using gradient direction," in *The 2nd International Conference on Information Engineering and Computer Science*, China, 2010.

[36] F. Schnorrenberg, C. S. Pattichis, K. C. Kyriacou, and C. N. Schizas, "Computeraided detection of breast cancer nuclei," *IEEE Trans. Inf. Technol. Biomed.*, vol. 1, no. 2, pp. 128–140, 1997.

[37] C. Primkhajeepong, P. Phukpattaranont, S. Limsiroratana, P. Boonyaphiphat, and K. Kayasut, "Evaluation of color based breast cancer cell image analysis," *Songklanakarin Journal of Science and Technology*, vol. 32, no. 3, pp. 231–239, 2010.

[38] K. Mosaliganti, L. Cooper, R. Sharp, R. Machiraju, G. Leone, K. Huang, and J. Saltz, "Reconstruction of cellular biological structures from optical microscopy data," *IEEE Trans. Vis. Comput. Graphics*, vol. 14, no. 4, pp. 863–876, 2008.

[39] K. Li, E. D. Miller, M. Chen, T. Kanade, L. E. Weiss, and P. G. Campbell, "Cell population tracking and lineage construction with spatiotemporal context," *Medical Image Analysis*, vol. 12, pp. 546–566, 2008.

[40] N. Otsu, "A threshold selection method from gray-level histograms," *IEEE Trans. Syst., Man, Cybern., Syst.*, vol. 9, no. 1, pp. 62–66, 1979.

[41] F. Meyer, "Topographic distance and watershed lines," *Signal Processing*, vol. 38, pp. 113–125, 1994.

[42] P. Phukpattaranont and P. Boonyaphiphat, "Color based segmentation of nuclear stained breast cancer cell images," *ECTI Transactions on Electrical Engineering, Electronics, and Communications*, vol. 5, no. 2, pp. 158–164, 2007.

[43] D. L. Olson and D. Delen, *Advanced Data Mining Techniques*, Berlin: Springer Verlag, 2008.

**APPENDIX A**

**RELATED PAPERS**

**Proceedings of 2009 ECTI International Conference (ECTI-CON 2009), Pattaya,**

**Thailand**

# Preliminary Results of Cell Image Segmentation using Dynamic Force Estimation on a Static Vane

Y. Surut and P. Phukpattaranont

Department of Electrical Engineering, Prince of Songkla University, Thailand

*Abstract*- This paper presents a novel method for cell image segmentation. The approach is based on the application of dynamic force estimation on a static vane (DFESV) to medical image processing problems. The other processes in the approach include smoothing filter using anisotropic diffusion, thresholding using Otsu's algorithm, morphology operation, marking boundary segment, angle image operator, and angle relation merging. Microscopic images from breast cancer tissue are used for evaluation of the approach. Preliminary results show that cell image segmentation based on the DFESV can successfully separate multiple attach cells into distinct single cells.

## I. INTRODUCTION

Pathologists carry out cell image analysis by visual inspection on cell appearances such as sizes, shapes, textures, and colors. However, the task is time consuming, costly, and tedious. In addition, visual inspection yields only subjective results. Recently, a computer-aided image analysis gains more interest due to the developments in computer capabilities and the advancement in image processing algorithms. Benefits resulting from a computer-aided analysis include an acceleration of time, a reduction in cost, and a decrement in a false inspection due to fatigue. Additionally, it provides a quantitative description of each particular cell in the image. Consequently, variations in image analysis resulting from human can be reduced.

An important step in cell image analysis is cell segmentation, the process of separating cell from background. There have been many algorithms aiming to improve performance of automatic cell image segmentation process. Based on geometric point of view, features of cell images are extracted to segment homogenous cell boundary [1]-[6]. Elliptical shape and texture of cell images are utilized to find boundary [1]-[3]. Besides, geometry of cell images is used in segmentation based on active contour and watershed [4]-[6]. Benefit and performance of each algorithm depend on various factors such as cell type, cell image acquisition, cell compactness, and cell image quality.

This paper presents a novel idea on cell image segmentation, which is able to inherently separate overlapping cells. As a result, accurate number of cells and accurate cell boundary in the image can be obtained. The approach is based on the application of dynamic force estimation on a static vane (DFESV) to medical image processing problems.

## II. THEORY

### A. Dynamic Force Estimation on a Static Vane (DFESV)

Dynamic force estimation on a static vane, i.e. a momentum force of fluid flow on the static vane, can be expressed as [8]

$$\sum \mathbf{F} = \rho Q \Delta \mathbf{V}, \qquad (1)$$

where $\mathbf{F}$ is result of all the forces acting on the fluid, $\rho$ is fluid mass density, $Q$ is fluid volume flow rate, and $\Delta \mathbf{V}$ is the difference in fluid velocity. Fig. 1 shows a diagram of forces on the fluid applied to the static vane. Assuming that the flow is in a horizontal and vertical planes, we can rewrite (1) as

$$F_x = \rho Q V_2 \cos(\theta_2) - \rho Q V_1 \cos(\theta_1), \qquad (2)$$
$$F_y = \rho Q V_2 \sin(\theta_2) - \rho Q V_1 \sin(\theta_1), \qquad (3)$$

where $F_x$ is fluid force on horizontal plane, $F_y$ is fluid force on vertical plane, $V_1$ is fluid velocity at inlet vane, $V_2$ is fluid velocity at outlet vane, $\theta_1$ is inlet vane angle, and $\theta_2$ is outlet vane angle.

### B. Implementation of the DFESV

For the implementation of dynamic force estimation on image processing, we define inlet ($\theta_1$) and outlet ($\theta_2$) vane angles based on intensity gradient as shown in Fig. 2(a). The direction of fluid flow in each pixel can be calculated in eight pairs by determining inlet and outlet vane angles from intensity gradient angles of neighborhood intensity pixels. Example of one in eight pairs of the implementation is shown in Fig. 2(b). We define $Q$, $\rho$, $V_1$ and $V_2$ to be one and define a variable $\alpha$ as a varying angle of inlet vane. Thus, we can rewrite force equations into

$$F_x(\theta_1, \theta_2) = \cos(\theta_2) - \cos(\alpha\theta_1),$$
$$F_y(\theta_1, \theta_2) = \sin(\theta_2) - \sin(\alpha\theta_1). \qquad (4)$$

Results of force estimation at each pixel consist of eight force values from eight pairs of fluid flow directions. We normalize force in each direction to the range between 0 and 255 and keep only the minimum value.
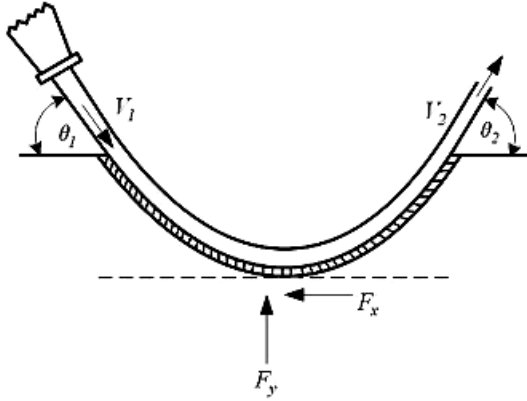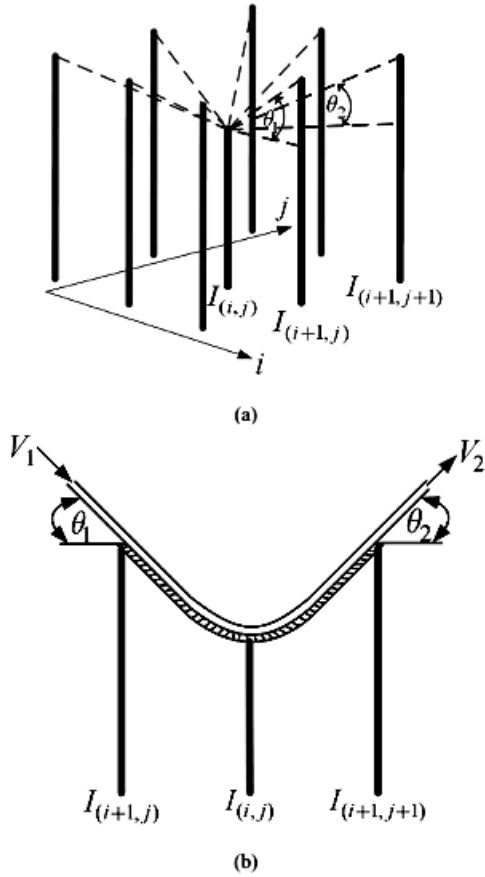
Figure 1. Force on the fluid in a static vane.



(a)



(b)

Figure 2. (a) Angle from intensity gradient. (b) Fluid flow direction in force estimation.

### C. Application of the DFESV to Image Segmentation

Fig. 3 shows a flow chart of cell image segmentation based on the DFESV. The algorithm is composed of two main parts: Image preprocessing and image segmentation. In image preprocessing part, RGB image is converted to gray-level image. Subsequently, anisotropic diffusion is applied to smooth region of object in the image while still preserve object edge and sharp intensity gradient [7].

In image segmentation part, we apply the DFESV algorithm and binary thresholding with the threshold value from Otsu's algorithm to the gray-level image after smoothing. While binary thresholding separates the cells from background as an object in the form of multiple attached cells, the DFESV algorithm divide the cells into many smaller parts of a larger whole cell. However, after we perform morphology operator, marking boundary segment, angle image operator, and merging with angle relation, we can separate multiple attached cells to single distinct cells. Details of the stated algorithms are given below.

### D. Morphology Operator

Morphology operator is a processing of the spatial form or structure. We apply erosion and dilation operators to eliminate noise in the binary image [10]. In addition, we apply thinning operation [11] and boundary finding to extract boundary of a binary cluster.

### E. Marking Boundary Segment

The DFESV algorithm gives many disconnected smaller parts of a larger whole cell. Thus, we have to build the process to make the smaller parts of the whole cell connect together. This process is called *Marking boundary segment*. Input images in this process are gray-level image after smoothing filter, binary image from morphology operator, and binary image from Otsu's thresholding.

### F. Angle Image Operator

Angle image operator is a processing to measure direction of image surface. Input of this process is the image from marking boundary segment. We calculate angle in each pixel with respect to the x axis and the y axis to obtain the direction of image surface. Angle values in both axes are calculated from inverse tangent of intensity image gradient.

### G. Merging with angle relation

This process determines the relationship of angles and regions. Direction angle and center co-ordinate data of each region are employed. We apply inverse cosine of dot product to find relation angles between connected regions. Each region locates in difference co-ordinate thereby we use the reference vector in this calculation. For example, relation angle between main region A and connected region B can be calculated by finding vector $\overline{BA}$ from center co-ordinate of region A and region B and then use this vector as a reference to compute angle direction of region B, which can be expressed as

$$\theta_{diff} = \cos^{-1}\left(\frac{\vec{B}\cdot\overline{BA}}{\left|\vec{B}\right|\left|\overline{BA}\right|}\right), \tag{5}$$

where $\vec{B}$ is direction vector of connected region and $\overline{BA}$ is vector of center co-ordinate from connected region to main region.
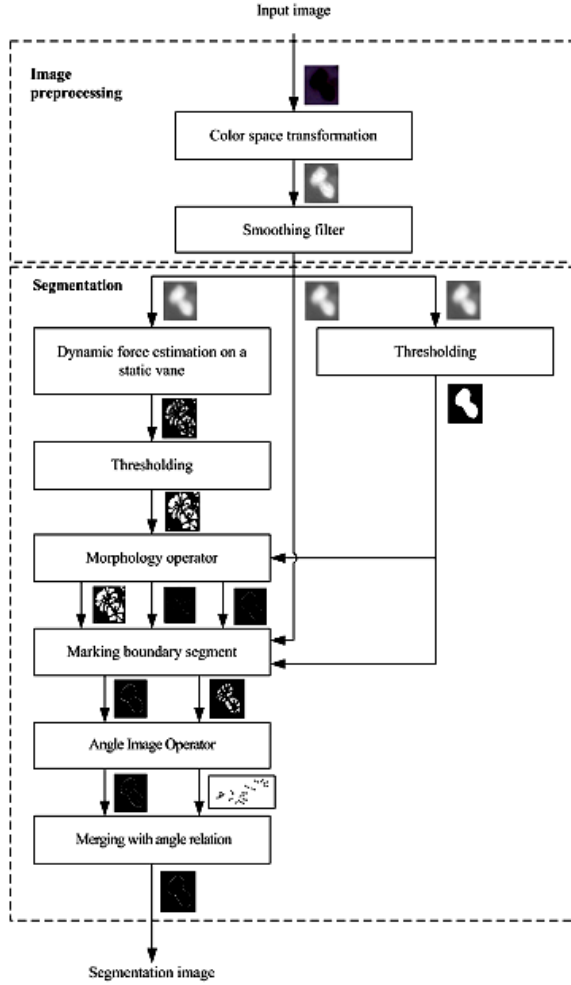
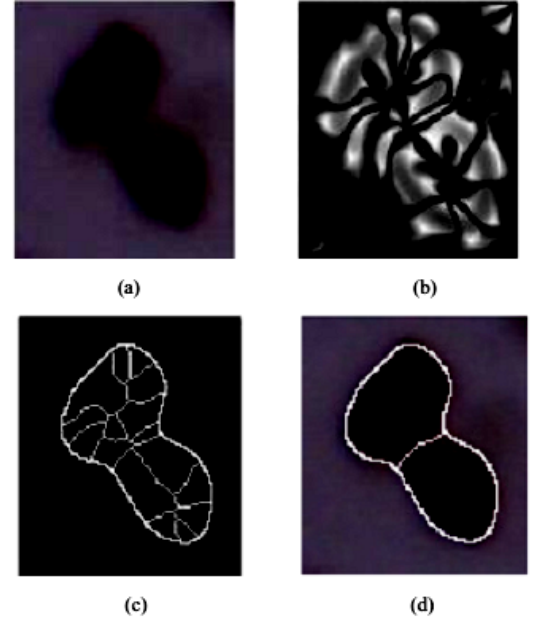Figure 3. Flow diagram of cell image segmentation based on the DFESV.



Figure 4. (a) Original image. (b) Force estimation on cell image. (c) Partition image. (d) Segmented image superimposed on the original image.
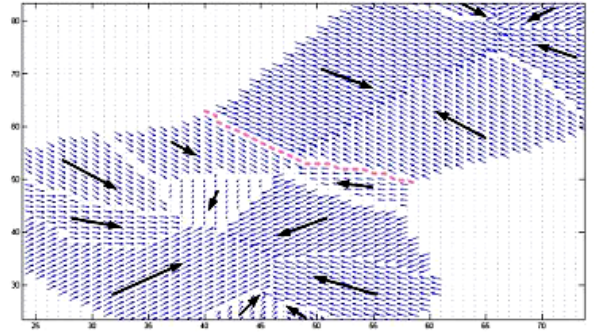


Figure 5. Direction of surface in gray-level image after averaging angle in each region and expand angle within boundary.

We compute angle relations of all regions and keep the set of angle relations. Then, we select the angle value to threshold connected region member. If angle member in each set has value more than specified angle threshold, this connected region member is cut off. In case of all members are removed on a selected threshold, the connected region member which has minimum angle is chosen. Then, we apply union operator to find relation of all set. At this time sets of connected region member represent region of the same object. We can merge each region by using set to identify label and then use $3 \times 3$ mask to delete boundary of region in the same object.

## III. MATERIALS AND METHODS

### A. Acquisition of the Images

The cell images used in this research were obtained from breast cancer cell tissue. The tissue slices were scanned by microscope (Eclipse 80i Advanced Research Microscope, Nikon Instech Co., Ltd., Japan) with a magnifying factor of 200. Contrast and brightness were adjusted by a specialist. The obtained color images were 2560x3200 JPEG format [12].

### B. Cell Image Segmentation Method

We apply cell segmentation algorithm based on the DFESV as described in Section II to breast cancer images. Parameters used in the algorithm are as follows. Parameter $\kappa$ and iteration number in anisotropic filter process were defined as 15 and 20, respectively. Parameter $\alpha$ in force estimation process was defined as 3 to adjust angle of inlet vane. The defined threshold angle value used in merging with angle relation process was 36 degree. Two images are tested to demonstrate performance of our proposed algorithm. The first image consists of two overlapping cell. This image was used to explain results in all details of the algorithm. The second image is composed of many multiple attached cells. Result of this image was used to demonstrate the performance of algorithm in a more realistic situation.
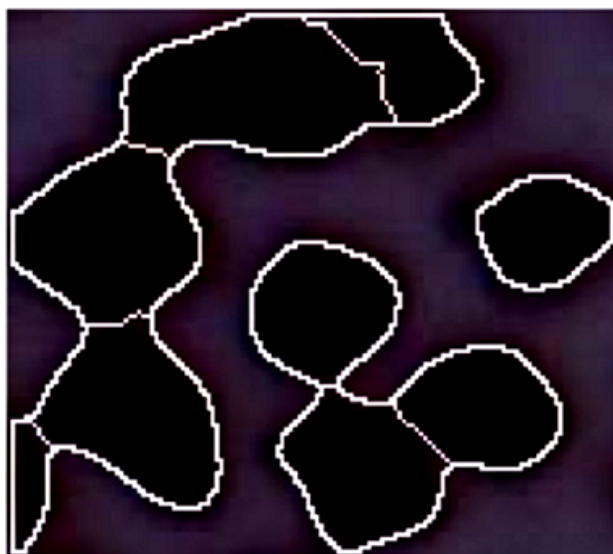
(a)
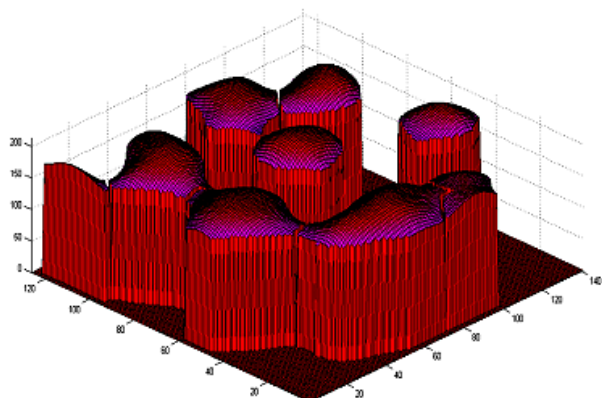


(b)

Figure 6. (a) Segmented images from the DFESV superimposed on the original image. (b) Perspective intensity plot.

## IV. RESULTS AND DISCUSSION

Fig. 4(a) shows an original RGB image consisting of a pair of overlapping cells. After RGB to gray-level conversion and the application of anisotropic diffusion, the DFESV algorithm was performed and its output was shown in Fig. 4(b). One can see that the cell image was divided into many disconnected smaller parts of a larger whole picture. In order to connect all smaller parts in the larger whole image, morphology operator and marking boundary segment are operated. Connected image result is shown in Fig. 4(c).

Fig. 5 shows direction of surface in gray-level image after averaging angle in each region and expands the angle within boundary. Finally, we utilized the merging with angle relation process to combine all related regions. The merging result superimposed on the original image is shown in Fig. 4(d). It is

shown that the two overlapping cells are successfully separated into two distinct single cells by the DFESV approach. Fig. 6 shows the segmented image superimposed on the original image consisting of many attached cells and the perspective intensity plot of segmented image. The result confirms performance of cell image segmentation algorithm based on the DFESV.

## V. CONCLUSION

We introduce an algorithm for segmenting multiple attached cells using dynamic force estimation on a static vane (DFESV). Preliminary results of investigation show that overlapping cells are segmented with satisfactory boundary. In order to develop a more complete system, we will improve algorithm to automatically adjust parameters, i.e. $\alpha$ in force estimation process and the threshold angle value used in merging. Then, we will apply the approach to more images for validation and also apply to other categorized cell images such as neuroblastoma images. Results will be reported in the near future.

## REFERENCES

[1] H.-S. Wu, J. Barba, and J. Gil, "A parametric fitting algorithm for segmentation of cell images," *IEEE Trans. Biomed. Eng.*, vol. 45, no. 3, pp. 400-407, Mar. 1998.

[2] H.-S. Wu, J. Gil, R. Jeremiah and J. Barba, "Unsupervised approach for segmentation of textured cytologic images," *Electron. Lett.*, vol. 35, no. 8, pp. 630-631, Apr. 1999.

[3] T. Jiang and F. Yang, "An evolutionary tabu search for cell image segmentation," *IEEE Trans. Syst., Man, Cybern. B, Cybern.*, vol. 32, no. 5, pp. 675–678, Oct. 2002.

[4] J. Park and J. M. Keller, "Snakes on the watershed," *IEEE Trans. Pattern Anal. Mach. Intell.*, vol. 23, no. 10, pp. 1201–1205, Oct. 2001.

[5] L. Yang, P. Meer and D. J. Foran, "Unsupervised segmentation based on robust estimation and color active contour models," *IEEE Trans. Inf. Technol. Biomed.*, vol. 9, no. 3, pp. 475-486, Sep. 2005.

[6] K. Z. Mao, P. Zhao and P.-H. Tan, "Supervised learning-based cell image segmentation for p53 immunohistochemistry," *IEEE Trans. Biomed. Eng.*, vol. 53, no. 6, pp. 1153-1163, Jun. 2006.

[7] P. Perona and J. Malik, "Scale-space and edge detection using anisotropic diffusion," *IEEE Trans. Pattern Anal. Mach. Intell.*, vol. 12, no. 7, pp. 629-639, Jul. 1990.

[8] E. J. Finnemore and J. B. Franzini, *Fluid Mechanics with Engineering Applications*, McGraw-Hill, Inc., 1997.

[9] N. Otsu, "A threshold selection method from graylevel histograms," *IEEE Trans. Syst., Man, Cybern*, vol. SMC-9, no. 1, pp. 62–66, 1979.

[10] R. C. Gonzalez and R. E. Woods, *Digital Image Processing*, Prentice-Hall, Inc., 2002.

[11] L. Lam, S.-W. Lee and C. Y. Suen, "Thinning methodologies-a comprehensive survey," *IEEE Trans. Pattern Anal. Mach. Intell.*, vol. 14, no. 9, pp. 869–885, Sep. 1992.

[12] P. Phukpattaranont and P. Boonyaphiphat, "Automatic classification of cancer cells in microscopic image: preliminary results," in *Proc. 21st Int. Conf. ITC-CSCC.*, 2006, pp.113-116.

**The 2<sup>nd</sup> Biomedical Engineering International Conference**

**(BMEiCON 2009), Phuket, Thailand**

# UNSUPERVISED BACKGROUND ELIMINATION FOR NEUROBLASTOMA MICROSCOPIC IMAGES

Y. Surut[1], P. Phukpattaranont[1], and S. Shuangshoti[2]

[1]Department of Electrical Engineering, Faculty of Engineering, Prince of Songkla University, Thailand
[2]Department of Pathology, Faculty of Medicine, Chulalongkorn University, Thailand

## ABSTRACT

*The objective of this article is to separate cell boundaries out of the background in the neuroblastoma microscopic images using the unsupervised operation. Two algorithms i.e., the Intensity thresholding and the K-means clustering, are applied in the RGB color space. The grouping of the RGB color space is also utilized to evaluate result comparison. The images in this paper contain the various properties such as cell compactness, multilevel color distribution and entire cell texture. The results were validated using sensitivity and average operation time. The appropriate approach agrees on the one hand, the intensity thresholding (Otsu's algorithm) on the R channel images from the sensitivity and the average operation time are 96.49% and 7.60 sec per image. On the other hand, the K-means clustering on the R channel images from the sensitivity and the average operation time are 96.53% and 8.89 sec per image. The appearance boundaries of the obtained images are also considered. The resultants of appropriate approach show that the cell boundaries satisfy constraint.*

## 1. INTRODUCTION

Neuroblastoma is a nerve cancer which is commonly found in embryo, infant and children [1]. The treatment planning of this disease obtains from histology diagnosis of cancer cell invasion. Pathologists investigate cancer invasion under tissue strained with haematoxylin and eosin (H&E) and capture image with microscope. However, disadvantage of human inspection system such as time consumption, cost and tedious may occur. So, computer-aid analyzer is become more and more significance to gain diagnosis performance and reduce time consumption.

According to computer-aid analyzer of neuroblastoma research, outcome is still sparse. The existed analysis system for the neuroblastoma images aim to grade neuroblastoma histology to stroma-rich and stroma-poor with an offline feature selection and K-nearest neighbor classifier (KNN) [1]. Besides the mention approach, multi resolution and existed classify approach such as KNN, LDA, Bayesian and SVM are applied to extract feature and classify the neuroblastoma microscopic images [2]. The above-mentioned researches almost utilize supervised classification. The goal of this research

is the application of color image in each spectrum component to extract object information which is cell boundaries. In addition, the proposed classifier in this research is the existed unsupervised approach such as intensity thresholding (Otsu's algorithm) and *K*-means clustering.

## 2. THEORY

### 2.1 Intensity thresholding

The classical of prevalent *global thresholding* is Otsu's algorithm [3]. Based on the statistical theory, the intensity histogram shows the separate intensity cluster of object and background. The level of histogram which gives the maximum of class mean is the finest point to threshold objects in the image. The maximum of class mean can be formulated as

$$\sigma_B^2(k) = \max_{1 \le k < L} \left( \frac{\left[ \mu_T \omega(k) - \mu(k) \right]^2}{\omega(k)\left[ 1 - \omega(k) \right]} \right),$$

where $\mu_T$ is the total mean intensity level of the image, $\omega(k)$ is the *zero*[th]-order cumulative moments up to the $k^{th}$ histogram level and $\mu(k)$ is the first-order cumulative moments up to the $k^{th}$ histogram level.

### 2.2 *K*-means clustering

The *K*-means clustering is the useful classification method where the data is normal distribution [4]. Definition of the centroids and grouping with the nearest distance between data points and centroid coordinate are the major notion of this approach. The convenient formalization can be expressed as

$$S = \sum_{j=1}^{J} \sum_{k=1}^{K} r_{nk} \left\| \mathbf{x}_n - \boldsymbol{\mu}_k \right\|^2,$$

where $r_{nk}$ is the set of cluster indicator, represented as binary value 0 or 1, $\mathbf{x}_n$ is the selected feature data and $\boldsymbol{\mu}_k$ is the data points which is represented as cluster. To find
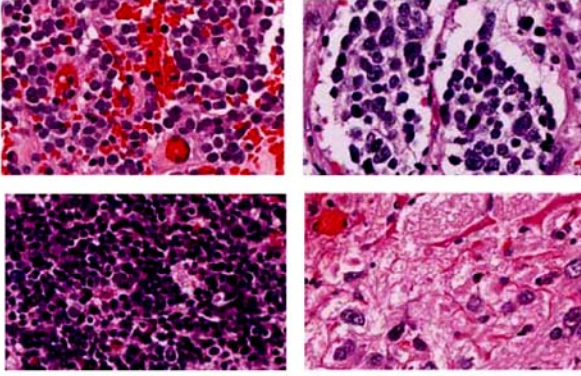
**Figure 1.** The various cell characteristics of the neuroblastoma microscopic images.
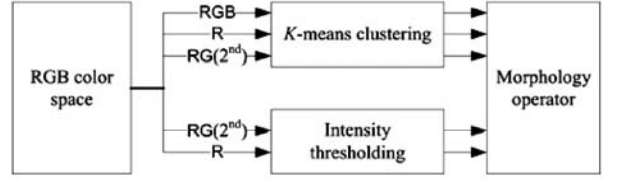


**Figure 2.** The flow diagram of unsupervised background elimination approach.
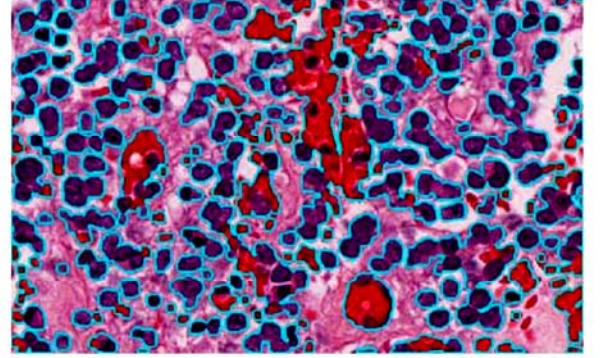


**Figure 3.** The segmented image from the *K*-means clustering on the RGB group.

the minimization of *S*, the iterative procedure is utilized. The first stage, the initial value of $\boldsymbol{\mu}_k$ is defined. Then, the minimization of *S* is determined which is that consider $r_{nk}$ and fix $\boldsymbol{\mu}_k$. Afterward, the minimization of *S* is also determined which is that consider $\boldsymbol{\mu}_k$ and fix $r_{nk}$. The approach is then repeated until set of group is stabilized. In the consideration of $r_{nk}$, binary number is assigned to determine group label by set value $r_{nk}$ to 1 in group *k* if summation of distance is minimum. The formalization of $r_{nk}$ assignment can be expressed as

$$r_{nk} = \begin{cases} 1 & \text{if } k = \arg\min_j \left\| \mathbf{x}_n - \boldsymbol{\mu}_k \right\|^2 \\ 0 & \text{otherwise} \end{cases}.$$

From the quadratic function in *S* evaluation, the optimization of $\boldsymbol{\mu}_k$ can be easily solved as

$$\boldsymbol{\mu}_k = \frac{\sum_n r_{nk} \mathbf{x}_n}{\sum_n r_{nk}}$$

where *n* is the number of the selected feature data and *k* is number of cluster indicator.

### 2.3 Morphology operator

The mathematical morphology is the function of set theory. Morphology operator is applied in object description such as edge detection, shape identification, image rotation, etc [5]. The basic morphology operators such as erosion and dilation, are subsequently defined as

$$A \ominus E = \left\{ z \middle| \left( E \right)_z \subseteq A \right\}$$

and

$$A \oplus E = \left\{ z \middle| \left[ \left( \widehat{E} \right)_z \cap A \right] \subseteq A \right\}$$

where *E* is the structuring element. In this research, we apply erosion and dilation in the closing and opening operators to eliminate the undesirable objects and connect the fragmented object in the binary image from unsupervised background elimination. The formalization of closing and opening operators can be subsequently expressed as

$$A \bullet E = \left( A \oplus E \right) \ominus E$$

and

$$A \circ E = \left( A \ominus E \right) \oplus E.$$

### 3. MATERIALS AND METHODS

#### 3.1 Acquisition of the images

The neuroblastoma images in this research were obtained from tissue strained with haematoxylin and eosin (H&E). The neuroblastoma images were acquired using the Eclipse 80i advanced research microscope (Nikon Instech Co., Ltd., Japan) with 40x magnifying factor. The contrast and intensity of the images were adjusted by a specialist. The storage images from microscope were cropped with $944 \times 742$ pixels. The 152 cropped images were compressed as JPEG files. The neuroblastoma cells in obtained images were marked by pathologist. The total 26003 cells from the five image sets were used in the approach evaluation. The structures of the tissue-stained images consist of the different characteristic, such as blue-purple color of nuclei and cytoplasm, neuropil and
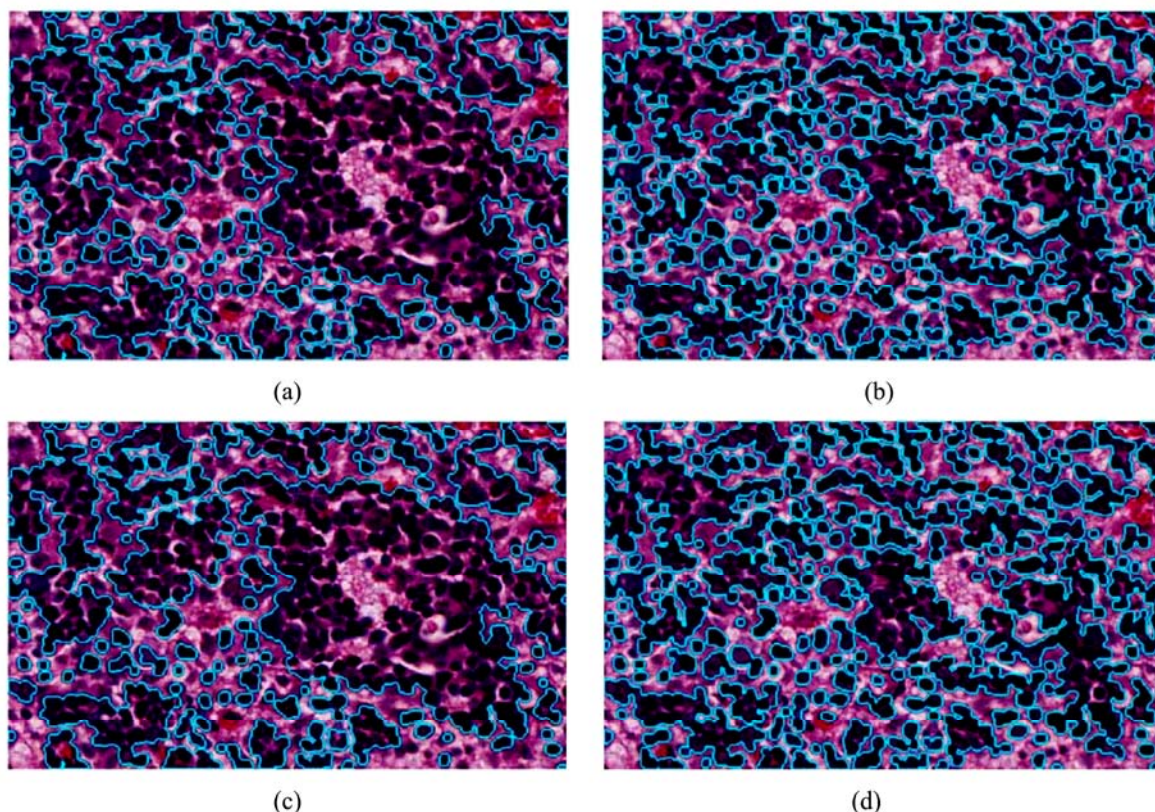
**Figure 4.** The segmented image from the approach. (a) The 2$^{nd}$ Otsu's algorithm on the RG group. (b) The Otsu's algorithm on the R group. (c) The 2$^{nd}$ $K$-means clustering on the RG group. (d) The $K$-means clustering on the R group.

red blood cells. The different characteristic of the cell images are illustrated in the Fig. 1.

### 3.2 Unsupervised background elimination

The approach of unsupervised background elimination based on the color space understanding extraction. The RGB color space is prepared to provide to unsupervised classification method in the name of Otsu's algorithm and $K$-means clustering. The observation of each image plane in RGB color space exposes the contrasting ability to separate cells out of background. The input image data were prepared in different group such as RGB group, RG group and G group for propose of image understanding extraction.

In this research we proposed five methods which are grouped with color space data as flow diagram in Fig. 2. First we prepared the groups of color space data such as RGB group, RG group and R group. Then we used $K$-means clustering and Otsu's algorithm to classify cells out of background. Especially the approach for RG group, in the name of the 2$^{nd}$ approach, were first classified the image on R channel image and then estimated the mean intensity of each group. The lowest mean intensity of any group was selected and the pixels of G channel in the same positions were classified again. The final clusters for all proposed methods were also selected same as the mentioned approach.

Almost the segmented images from the clustering approach have the fragmented area. The morphology operator is used to connect successfully the fragmented area and remove tiny pieces. We first connected fragmented area with the closing operator and then fill hole. Finally the opening operator was utilized to remove tiny piece. In the morphology operator, the structure element object was a flat disk shape where the radius equals six.

### 3.3 Evaluation of system performance

Sensitivity (SS) and average time operation are used as the measurement of performance evaluation. Sensitivity is the probability of the system detection on cells which is marked by the experts. The sensitivity evaluation is expressed as

$$SS = \frac{TP}{TP + FN},$$

where $TP$ (true positive) are the number of cell nuclei which are identical to the expert marker and $FN$ (false negative) are the number of cell nuclei which are identified by the expert but the system can not detect.

**Table 1.** The resultants of the evaluation on the sensitivity estimation and the average operating times.

| Set No. | Cell Number | K-means(RGB) | | K-means(R) | | 2nd K-means(RG) | | Otsu(R) | | 2nd Otsu(RG) | |
|---|---|---|---|---|---|---|---|---|---|---|---|
| | | TP | FN | TP | FN | TP | FN | TP | FN | TP | FN |
| 1 | 1772 | 1746 | 26 | 1656 | 116 | 1597 | 175 | 1653 | 119 | 1596 | 176 |
| 2 | 5893 | 5816 | 77 | 5746 | 147 | 5480 | 413 | 5745 | 148 | 5475 | 418 |
| 3 | 3967 | 3809 | 158 | 3706 | 261 | 3377 | 590 | 3702 | 265 | 3373 | 594 |
| 4 | 12128 | 11993 | 135 | 11895 | 233 | 11320 | 808 | 11894 | 234 | 11314 | 814 |
| 5 | 2243 | 2191 | 52 | 2098 | 145 | 2078 | 165 | 2096 | 147 | 2078 | 165 |
| Sum | 26003 | 25555 | 448 | 25101 | 902 | 23852 | 2151 | 25090 | 913 | 23836 | 2167 |
| Sensitivity (%) | | 98.28 | | 96.53 | | 91.73 | | 96.49 | | 91.67 | |
| Avg. Times (s) | | 10.85 | | 8.89 | | 12.10 | | 7.60 | | 10.29 | |

Due to the fact that the approach could not completely segments the overlapping and touching cells, the evaluation to measurement accuracy was based on background sensitivity and visual investigation. In addition, the time consumption of operation was considered to also determine the approach performance case for the approach yielded the close resultant.

## 4. RESULTS AND DISCUSSION

In the table 1, the proposed approaches were applied and evaluated with background sensitivity. The maximum sensitivity from the RGB group on the K-means clustering was not optimized yield because the cells and background data from RGB color data produce more indistinct objects. Thus we can see the disadvantage of this approach shown in Fig. 3 which the red blood cells were assembled in the cell boundaries. In case of the K-means clustering and Otsu's algorithm on R group, the sensitivities were 96.53% and 96.49%, respectively and the average operating times were 8.89 sec and 7.60 sec, respectively. In the remaining approach, the 2nd segmentation on both K-means and Otsu's algorithm, the sensitivities were 91.73% and 91.67%, respectively and the average operating times were 12.10 sec and 10.29 sec, respectively. When we compared the mentioned approaches, we found that performance of the first segmentation algorithm prevailed over the second segmentation algorithm in the meaning of the background sensitivity and the average operating times. From the Fig. 4, the obtained images from the second segmentation algorithm reveal the predomination over the first segmentation algorithm when the microscopic images were the compact cell distribution. Thus we selected the first segmentation algorithm, the K-means clustering and Otsu's algorithm on R group, to consider in the next comparison.

Finally, we considered the performance of the selected approaches, the K-means clustering and the Otsu's algorithm on R channel, found that the approaches were close performance. The Otsu's algorithm operated faster but less sensitivity than the K-means clustering.

## 5. CONCLUSION

In this research, we introduce the unsupervised background elimination for the neuroblastoma microscopic images. The approach proposes the Otsu's algorithm and the K-means clustering on the multi group of RGB color space. The morphology operator is applied to fulfill the boundary extraction. The results of performance evaluation show the significant outcome. On the one hand, the Otsu's algorithm on the R channel images is selected if precedence to time consumption is required. On the other hand, the K-means clustering on the R channel images is chosen if priority to the sensitivity is needed.

## 6. ACKNOWLEDGEMENT

## REFERENCES

[1] O. Sertel, J. Kong, H. Shimada, U. V. Catalyure, J. H. Salt, and M. N. Gurcan, "Computer-aided prognosis of neuroblastoma on whole-slide images: classification of stromal development," *Journal Pattern Recognition,* vol. 42, issue. 6, pp. 1093-1103, June. 2009.

[2] J. Kong, O. Sertel, H. Shimada, K. L. Boyer, J. H. Saltz, and M. N. Gurcan, "Computer-aided evaluation of neuroblastoma on whole-slide histology images: classifying grade of neuroblastic differentiation," *Journal Pattern Recognition,* vol. 42, issue. 6, pp. 1080-1092, June. 2009.

[3] N. Otsu, "A threshold selection method from graylevel histograms," *IEEE Trans. Syst., Man, Cybern*, vol. SMC-9, no. 1, pp. 62–66, Jan. 1979.

[4] C. M. Bishop, *Pattern Recognition and Machine Learning*, Springer Science+Business Media, USA, 2006.

[5] R. C. Gonzalez and R.E. Woods, *Digital Image Processing*, Prentice-Hall, Inc., 2002.

**Proceedings of the Second APSIPA Annual Summit and Conference, Biopolis, Singapore**

# Overlapping Cell Image Segmentation using Surface Splitting and Surface Merging Algorithms

Yunyong Surut and Pornchai Phukpattaranont

Faculty of Engineering, Prince of Songkla University, Songkhla, Thailand, 90110

E-mail: pornchai.p@psu.ac.th  Tel: +66-074-287243

*Abstract*— This paper presents a novel method for overlapping cell image segmentation. The approach is based on surface splitting and surface merging algorithm applied to medical image processing problems. While the surface splitting algorithm divides the overlapping cell image into pieces of different shapes, the surface merging algorithm correctly joins them together to form the separating cell image. The surface splitting approach operates based on clustering of gradient directions of split surface angles. Then, surface merging is applied to combine each fragment with a specific condition in order to find individual cells. Microscopic images from breast cancer tissue are used for evaluation of the approach. Results show that cell image segmentation based on surface splitting and surface merging algorithms can successfully separate multiple attached cells into distinct single cells.

## I. INTRODUCTION

Pathologists carry out cell image analysis by visual inspection on cell appearances such as sizes, shapes, textures, and colors. However, the task is time consuming, costly, and tedious. In addition, visual inspection yields only subjective results. Recently, a computer-aided image analysis gains more interest due to the developments in computer capabilities and the advancement in image processing algorithms. Benefits resulting from a computer-aided analysis include an acceleration of time, a reduction in cost, and a decrement in a false inspection due to fatigue. Additionally, it provides a quantitative description of each particular cell in the image. Consequently, variations in image analysis resulting from human can be reduced.

An important step in cell image analysis is cell segmentation, the process of separating cell from background. There have been many algorithms aiming to improve performance of automatic cell image segmentation process. Based on geometric point of view, features of cell images are extracted to segment homogenous cell boundary [1]-[6]. Elliptical shape and texture of cell images are utilized to find boundary [1]-[3]. Besides, geometry of cell images is used in segmentation based on active contour and watershed [4]-[6]. Benefit and performance of each algorithm depend on various factors such as cell type, cell image acquisition, cell compactness, and cell image quality.

In this paper, we present a novel idea on cell image segmentation, which is able to inherently separate overlapping cells. As a result, accurate number of cells and accurate cell boundary in the image can be obtained. Based on image
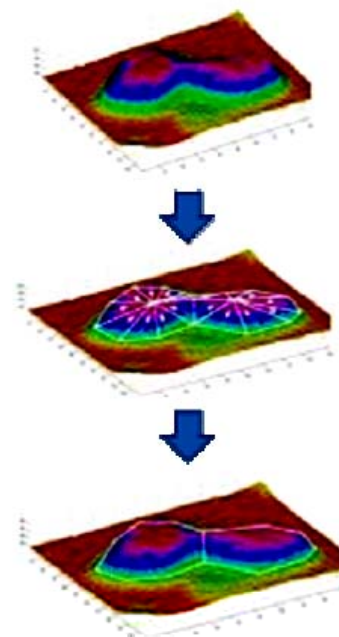


Fig.1 Principle of overlapping cell segmentation based on splitting and merging algorithms.

surface consideration, we apply two main approaches to split cell surface and then merge them with specific condition called surface splitting and surface merging algorithm, respectively.

The organization of this paper is as follows. Section II presents the methodology of proposed algorithm, its implementation, and its applications to cell segmentation problem. Section III describes materials used in experiment. Section IV provides the preliminary results and discussion. Finally, the conclusion is drawn in Section V.

## II. MEDTHODOLOGY

Fig. 1 shows a principle of overlapping cell segmentation based on splitting and merging algorithms. Overlapping cell surfaces in Fig. 1(Top panel) are divided into pieces of different shapes according to their gradient directions as shown in Fig. 1(Middle panel) by the splitting algorithm. Subsequently, they are joined together to form the two separating single cells as shown in Fig. 1(Bottom panel) by the merging algorithm. Details of the algorithm are as follows.

## A. Surface Splitting

Because the overlapping cell surface can be viewed like a mountain range, this behavior reveals some significance in the gradient direction. That is, for the individual cell, its gradient direction tends to direct to the same region, i.e., the top of the mountain. Thus, we use this behavior to split cell surface by clustering the gradient direction of each point into the angle range. So, we first calculate gradient direction of each point. Let $I_{i,j}$ is the intensity in spatial coordinates of the intensity image. We calculate image gradient $\left(\nabla I(x,y)\right)$ with approximation function $\partial I_{i,j}/\partial x \approx (I_{i+1,j} - I_{i-1,j})/2$ and $\partial I_{i,j}/\partial y \approx (I_{i,j-1} - I_{i,j+1})/2$. The magnitude in y-direction is reversed because the angle calculation employs gradient direction in Cartesian coordinates. Then, we exploit gradient of intensity image $\left(g_{i,j}, h_{i,j}\right)$ to calculate the angle value compared with the x-axis using an inverse tangent operator. However, the derived angle values are only range $0 - \pi/2$. We have to correct them to cover all angle range $0 - 2\pi$. Thus, the quadrant examination is applied in this task as following:

$$\omega_{i,j} = \begin{cases} \text{abs}\left(\theta_{i,j}\right) & \text{If } Q_{i,j} = 1 \\ \text{abs}\left(\theta_{i,j}\right) + \pi/2 & \text{If } Q_{i,j} = 2 \\ \text{abs}\left(\theta_{i,j}\right) + \pi & \text{If } Q_{i,j} = 3 \\ \text{abs}\left(\theta_{i,j}\right) + 3\pi/2 & \text{If } Q_{i,j} = 4 \\ & \text{If sign}\left(g_{i,j}\right) = 0 \text{ and sign}\left(h_{i,j}\right) < 0, \\ 3\pi/2 & \text{If sign}\left(g_{i,j}\right) = 0 \text{ and sign}\left(h_{i,j}\right) > 0 \\ \pi/2 & \text{If sign}\left(g_{i,j}\right) < 0 \text{ and sign}\left(h_{i,j}\right) = 0 \\ \pi & \text{If sign}\left(g_{i,j}\right) > 0 \text{ and sign}\left(h_{i,j}\right) = 0 \\ 0 \end{cases} \quad (1)$$

where $Q_{i,j}$ is the function of quadrant identification from gradient magnitude, and $\theta_{i,j}$ is the angle from the inverse tangent operator. Then, the $\omega_{i,j}$ can be used to cluster pixel into splitting surfaces by defining the number of cluster. Fig. 2(b) shows an example of splitting surface image where the defined clustering number is 8. Subsequently, the background is eliminated by the image from thresholding algorithm [7], The small pieces of splitting surface image, which are considered as noises, are removed using a morphology operator. Then, the single pixel boundary is obtained with a thinning operator [8]. The result of the approach in this step is shown in Fig, 2(c).

However, in some cases, the branch of splitting surface boundary occurs as illustrated in Fig. 2(c). Thus, De-branch algorithm is applied to eliminate them before surface merging. This approach determines member of labeled split surface in 3x3 mask, and then remove pixel which is judged to be branch. Let $b_{i,j}$ is the splitting surface image, $lb_{i,j}$ is the label image of $b_{i,j}$. We use average of $lb_{i,j}$ by 3x3 mask $\left(W_{i,j}\right)$ as $m_{i,j}$ to detect different members in $W_{i,j}$. In order to identify the threshold value $(T_{i,j})$, the equation is given by
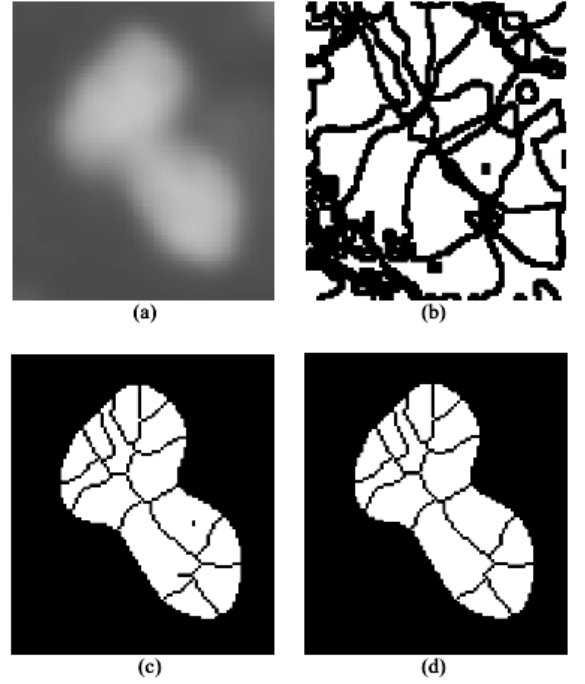


Fig.2 (a) The overlapping cell image. (b) The splitting image from clustering by angles. (c) The splitting surface image of overlapping cell. (d) The splitting surface image after de-branch approach.

$$T_{i,j} = \sum_{x=1}^{3}\sum_{y=1}^{3} \text{abs}\left(\left(Wlb_{x,y} - m_{i,j}\right)\cdot Wb_{x,y}\right), \quad (2)$$

where $Wlb_{x,y}$ is label value of $W_{i,j}$ from $b_{i,j}$, and $Wb_{x,y}$ is binary value of $W_{i,j}$ from $lb_{i,j}$. Finally, we set $b_{i,j} = 1$ when $T_{i,j} = 0$. The example of the obtained splitting surface image is illustrated in Fig. 2(d).

## B. Surface Merging

After surface splitting, we obtain the splitting surface, which can be used to merge with a specific condition. That is, their gradient directions are convergent to same region. Fig. 3(a) shows the gradient direction of each split surface represented with a vector. The convergence and divergence between neighborhood vectors indicate that they are from the same individual cell surface or not. On the one hand, if the vector relationship have convergent characteristic, the surfaces are from the same individual cell. On the other hand, if the vector relationship have divergent characteristic, the surfaces are not from the same individual cell. In numerical calculation, the convergent and divergent characteristics are determined based on a linear equation $y = mx + b$.

From Fig. 3(a), let $\mathbf{a}$ and $\mathbf{b}$ are the gradient vectors, which are from two connected splitting surface. The linear equation can be determined using their representing vectors. Thus, we can obtain $y = m_1 x + b_1$ and $y = m_2 x + b_2$,
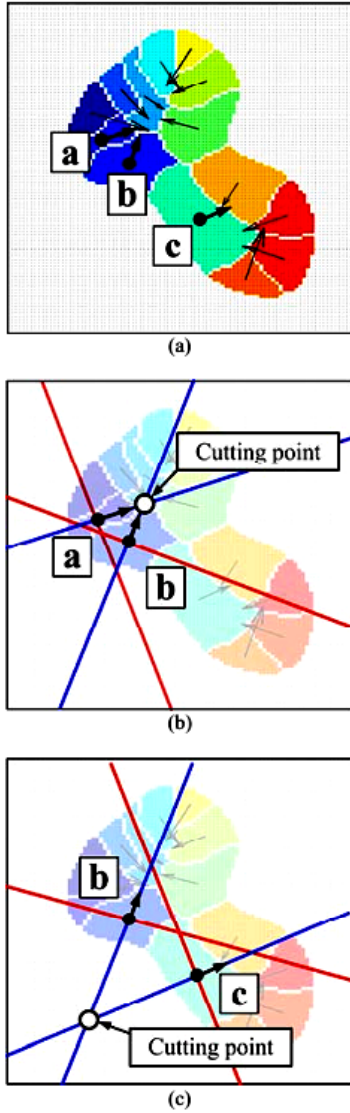
(a)

(b)

(c)

Fig.3 (a) Splitting surface image and their gradient vectors. (b) Convergent behavior. (c) Divergent behavior.
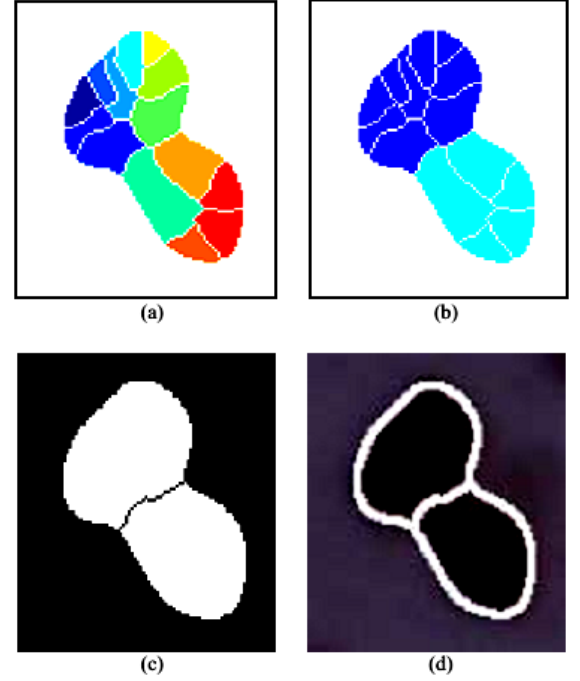


(a)

(b)

(c)

(d)

Fig.4 (a) Splitting surface image. (b) Splitting surface image after surface merging algorithm. (c) The obtained binary image after de-branch algorithm is applied. (d) Segmented image superimposed on the original image.

$$s_1 = \text{sign}\left(b_1 - (y_1 - m_1 x_1)\right),$$
$$s_2 = \text{sign}\left(b_1 - (y_3 - m_1 x_3)\right),$$
$$s_3 = \text{sign}\left(b_2 - (y_2 - m_2 x_2)\right),$$
$$s_4 = \text{sign}\left(b_2 - (y_3 - m_2 x_3)\right),$$

(3)

where point $(x_1, y_1)$, point $(x_2, y_2)$, and point $(x_3, y_3)$ are direction of **a** and **b**, and cutting point. Finally, if $s_1 = s_2$ and $s_3 = s_4$, we judge to the convergent characteristic. Otherwise, we classify it to the divergent characteristic. For implementation, we first find the property of each splitting surface as centroid, splitting surface neighbor, and average gradient. The algorithm can be expressed as following:

**Algorithm surface merging**
Calculate split surface property
Loop all split surface neighbor
      Find cutting point
      Find perpendicular linear equation
      Calculate $s_1$, $s_2$, $s_3$, and $s_4$
      If $s_1 = s_2$ and $s_3 = s_4$,
         Merge both split surfaces
      End
End loop

which represent the linear equations of **a** and **b**, respectively. Then, the cutting point of both lines is calculated. We use the obtained cutting point to classify the convergent characteristic from divergent characteristic. The rule is declared that if cutting point, direction of **a** and **b** are in the both areas of perpendicular linear equation of **a** and **b** as illustrates in Fig. 3(b), both vectors are judged to the convergent characteristic. Otherwise, they are judged to the divergent characteristic as illustrates in Fig. 3(c). To use this rule, we first calculate perpendicular linear equation of **a** and **b** . We obtain $y = -m_1 x + b_1$ and $y = -m_2 x + b_2$ , which represent the perpendicular linear equations of **a** and **b**, respectively. The implementation can be expressed by the following:

Fig. 3(b) shows the splitting surfaces, which are merged from detecting condition. The splitting surfaces that are not merged are shown in Fig. 3(c). When entire splitting surface neighbors in Fig. 4(a) are determined, the result can be illustrated as Fig. 4(b). We apply de-branch algorithm for this task. The result can be shown in Fig. 4(c). Finally, the extracted boundary is superimposed on the original image as illustrated in Fig. 4(d).

## III. MATERIALS AND METHODS

### A. Acquisition of the Images

The cell images used in this research were obtained from breast cancer cell tissue. The tissue slices were scanned by a microscope (Eclipse 80i Advanced Research Microscope, Nikon Instech Co., Ltd., Japan) with a magnifying factor of 200. Contrast and brightness were adjusted by a specialist. The obtained color images were 2560x3200 JPEG format.

### B. Cell Image Segmentation Method

We apply cell segmentation algorithm based on surface splitting and surface merging to breast cancer images. The organization of the method is illustrated in Fig. 5. It consists of image preprocessing, surface splitting, and surface merging. For image preprocessing, we exploit anisotropic diffusion filter [9] to smooth image surface. Parameter $\kappa$ and iteration number were defined as 50 and 40, respectively. The number of clustering angle and the area considered to be an object in surface splitting were defined as 8 and 50, respectively.

## IV. RESULTS AND DISCUSSION

Fig. 6 shows the experimental results of the segmented boundary obtained from surface splitting and surface merging. The splitting surface images are shown in the top row and the segmented images superimposed on the original images
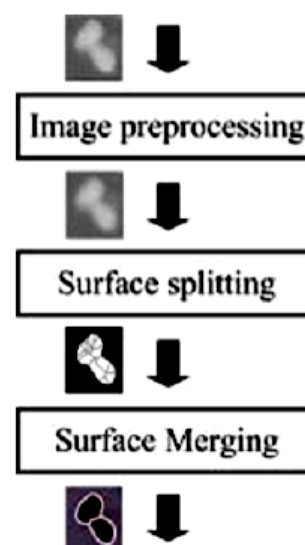


Fig.5 Flow diagram of cell segmentation algorithm based on surface splitting and surface merging.

are shown in the bottom row. For the splitting surface image, each individual cell consists of less than eight pieces of fragments because the number of cluster angle is defined as 8. It affects to the accuracy of merging if overlapping and individual cell surfaces are not split sufficiently.

Fig. 6(a)-(b) show the complete segmented boundary. One can see that the cell image was divided into many disconnected smaller parts of a larger whole picture using the surface splitting as illustrated in the top row. In order to connect all smaller parts in the larger whole image, surface merging was applied as illustrated in the bottom row.

Fig. 6(c)-(d) show the case of insufficient surface splitting. It affected to accuracy of the surface merging with over segmentation. This effect occurred to the individual cell,
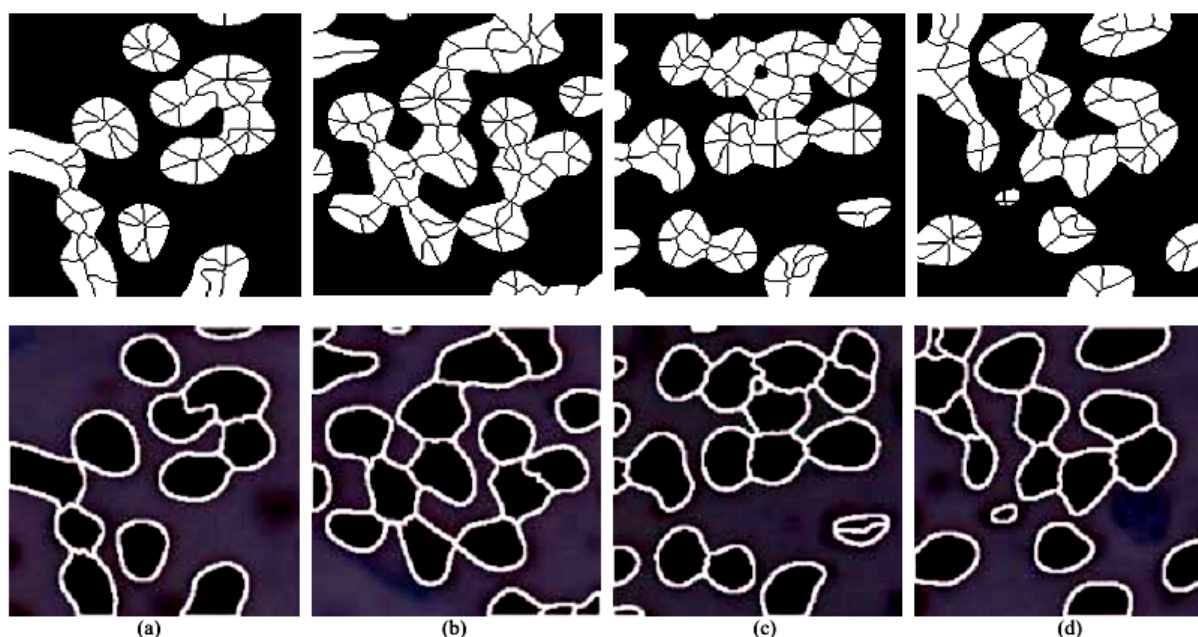


| (a) | (b) | (c) | (d) |

Fig. 6 The top row illustrates split surface image from surface splitting approach. The second row illustrates segmented image superimpose on the original image from surface merging approach. (a)-(b) The results from complete cell segmentation. (c)-(d) ) The results from incomplete cell segmentation.

which was small area, or attached to the rim of image. The over-segmentation can be alleviated by increasing the number of clustering angle, or allowing the larger split surface area in the surface splitting approach.

## V. Conclusions

We introduce an algorithm for segmenting multiple attached cells using surface splitting and surface merging algorithms. Preliminary results of investigation show that overlapping cells are segmented with satisfactory boundary. In order to develop a more complete system, we will improve algorithm to eliminate over-segmentation and improve the surface merging approach for increasing in performance and accuracy. Then, we will apply the approach to more images for validation and also apply to other categorized cell images such as neuroblastoma images. Results will be reported in the near future.

## References

[1] H.-S. Wu, J. Barba, and J. Gil, "A parametric fitting algorithm for segmentation of cell images," *IEEE Trans. Biomed. Eng.*, vol. 45, no. 3, pp. 400-407, Mar. 1998.

[2] H.-S. Wu, J. Gil, R. Jeremiah and J. Barba, "Unsupervised approach for segmentation of textured cytologic images," *Electron. Lett.*, vol. 35, no. 8, pp. 630-631, Apr. 1999.

[3] T. Jiang and F. Yang, "An evolutionary tabu search for cell image segmentation," *IEEE Trans. Syst., Man, Cybern. B, Cybern.*, vol. 32, no. 5, pp. 675–678, Oct. 2002.

[4] J. Park and J. M. Keller, "Snakes on the watershed," *IEEE Trans. Pattern Anal. Mach. Intell.*, vol. 23, no. 10, pp. 1201–1205, Oct. 2001.

[5] L. Yang, P. Meer and D. J. Foran, "Unsupervised segmentation based on robust estimation and color active contour models," *IEEE Trans. Inf. Technol. Biomed.*, vol. 9, no. 3, pp. 475-486, Sep. 2005.

[6] K. Z. Mao, P. Zhao and P.-H. Tan, "Supervised learning-based cell image segmentation for p53 immunohistochemistry," *IEEE Trans. Biomed. Eng.*, vol. 53, no. 6, pp. 1153-1163, Jun. 2006.

[7] N. Otsu, "A threshold selection method from graylevel histograms," *IEEE Trans. Syst., Man, Cybern*, vol. SMC-9, no. 1, pp. 62–66, 1979.

[8] L. Lam, S.-W. Lee and C. Y. Suen, "Thinning methodologies-a comprehensive survey," *IEEE Trans. Pattern Anal. Mach. Intell.*, vol. 14, no. 9, pp. 869–885, Sep. 1992.

[9] P. Perona and J. Malik, "Scale-space and edge detection using anisotropic diffusion," *IEEE Trans. Pattern Anal. Mach. Intell.*, vol. 12, no. 7, pp. 629-639, Jul. 1990.

**The 2nd International Conference on Information Engineering and Computer Science, Wuhan, China**

# Preliminary Results of Connected Object Segmentation using Gradient Direction

Yunyong Surut and Pornchai Phukpattaranont
Department of Electrical Engineering, Faculty of Engineering
Prince of Songkla University
Songkhla, Thailand

*Abstract*—This paper presents a novel algorithm based on the gradient direction to separate the multiple attaching and overlapping objects. The idea is based on the fact that the gradient directions of north, east, south, and west neighbourhood pixels are divergent when the gradient direction of the pixel located in the boundary region is used as a reference line. The proposed algorithm is composed of three steps: image denoising, pixel classification, and boundary extraction. The performance of the proposed approach is evaluated using the correctness of connected object counting and boundary accuracy measurement. Both evaluation results are compared with those from the traditional watershed algorithm. The evaluation results show that the proposed method provide better performance compared to the traditional watershed algorithm.

*Keywords-image segmentation; gradient direction; pixel classification; boundary extraction*

## I. INTRODUCTION

Image segmentation is an important step in image analysis for object classification or recognition. Its categorization based on image intensity operation can be classified into edge-based and region-based approaches [1]. On the one hand, the edge-based approach employs the discontinuities in the image intensity between an object and a background for identifying an object boundary. On the other hand, the region-based approach divides the image area using the defined condition.

In the region-based approach, watershed method is one of the most popular algorithms. Its operation can be carried out by flooding method into the intensity image surface to extract segmented boundaries. The reinforced method for the object feature can be included as either pre-processing of post-processing procedures. In the case of pre-processing procedure, the image surface can be reconstructed based on image information such as the distance transformation of binary image [2], the smoothing image surface [3], and the image surface from size and shape information [4]. Another approach in pre-processing watershed is to identify initial markers. The markers can be identified using the prior knowledge related to the target objects. There are many techniques to achieve this task. Based on morphology analysis, the region minima of distance transformed image can be used to indicate the individual object [5]. For more complex analysis when the object image surface is rough, the wrong marker needs to be suppressed using a pattern classification approach [6].
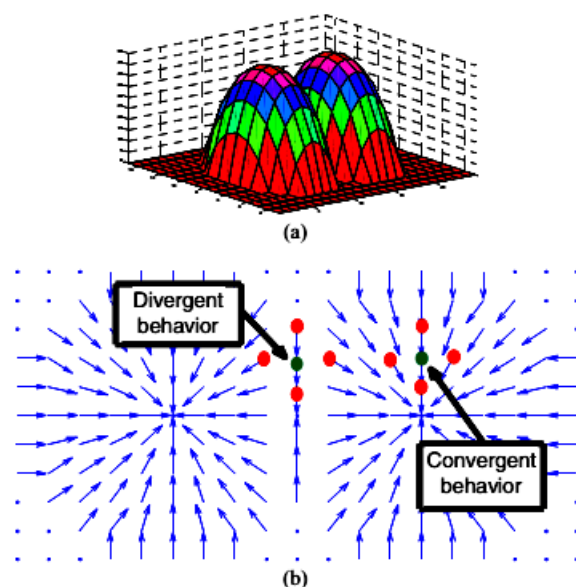


Figure 1. The divergent and convergent behaviors.

After watershed segmentation with pre-processing procedure, over-segmentation and under-segmentation problems are still existed. Thus, the post-processing procedure is employed in order to solve the problems. For example, the morphology operator is a simple choice to operate so that the over-segmented object can be combined using the hole-filling operator [7]. In [8], the feature of segmented object is extracted and used as an input to a pattern classifier in order to reconstruct the segmented boundary from the desirable object only. In addition, the co-operation between man and machine can increase accuracy of the object segmentation [9].

In this paper, we propose an alternative choice for separating multiple attached objects. From the previous research, all approaches exploit image intensity information. Nevertheless, there are some features, which can be used to separate overlapping or attaching object. We propose a novel algorithm, which extracts the object boundary based on the behaviour of gradient direction. The rest of this paper is organized as follows. We present the details of the proposed methodology in Section II. The experiments and results are given in Section III and Section IV, respectively. Finally, we conclude all obtained results in Section V.
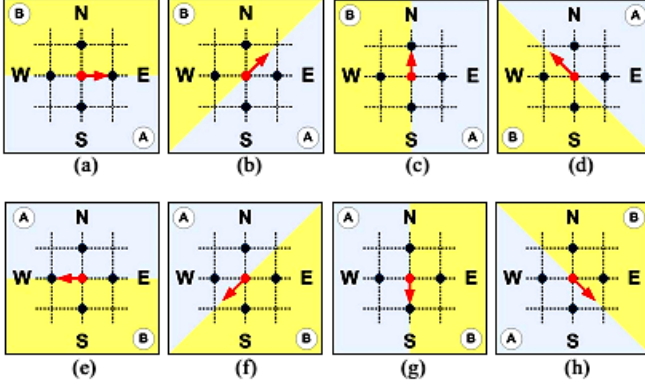
Figure 2. The possible cases of sign operators are identified by gradient direction reference, where areas A are the positive side; areas B are the negative side.

Figure 3. (a) The original image. (b) The binary image from the binarization of $\Delta\omega(x,y,v=x)$. (c) The binary image from the binarization of $\Delta\omega(x,y,v=-x)$. (d) The corrected binary image.

## II. METHODOLOGY

In this section, we propose the method to identify the pixel located at the boundary for separating the connected objects. Motivation of the proposed algorithm is from the employment of image gradient as shown in Fig. 1. Fig. 1(a) shows the image surface of attached objects, whose the boundary region is obviously observed. Another form of image, i.e, a gradient direction, is used for detecting boundary region. In Fig. 1(b), we can see that if the direction of central point gradient is used as a referent line, the directions of neighborhood gradient are divergent from this line. On the other hand, if a pixel does not locate in the boundary region, the directions of neighborhood gradient are convergent to the reference line. Based on this observation, we have developed an algorithm to classify the pixel in boundary region from the pixel in other areas of the image. Subsequently, the results from pixel classification are used for identifying the boundary of connected objects. Details of our proposed algorithm are as follows.

### A. Pixel Classification

*1) Angle estimation:* This step is used to estimate the angle of gradient direction in the Cartesian coordination. Let $I(x,y)$ be the intensity image in spatial coordination. The gradient magnitude of $I(x,y)$ is given by

$$G_x = \frac{1}{2}\left(I(x+1,y)-I(x-1,y)\right),$$
$$G_y = \frac{1}{2}\left(I(x,y-1)-I(x,y+1)\right). \quad (1)$$

Then, the gradient magnitude is used to estimate an angle $\omega(x,y,v)$ where $v$ is a reference axis. $v=x$ and $v=-x$ are used in this paper. The angle of gradient where $\theta(x,y)$ $=\arctan\left(G_y/G_x\right)$ can be expressed as

$$\omega(x,y,v)=\begin{cases}\theta(x,y), & G_x(x,y)>0 \text{ and } G_y(x,y)>0 \\ \theta(x,y)+\pi/2, & G_x(x,y)<0 \text{ and } G_y(x,y)>0 \\ \theta(x,y)+\pi, & G_x(x,y)<0 \text{ and } G_y(x,y)<0 \\ \theta(x,y)+3\pi/2, & G_x(x,y)>0 \text{ and } G_y(x,y)<0 \\ 3\pi/2, & G_x(x,y)=0 \text{ and } G_y(x,y)<0 \\ \pi/2, & G_x(x,y)=0 \text{ and } G_y(x,y)>0 \\ \pi, & G_x(x,y)<0 \text{ and } G_y(x,y)=0 \\ 0, & G_x(x,y)>0 \text{ and } G_y(x,y)=0 \end{cases} \quad (2)$$

*2) Sign identification:* The objective of this step is to divide four neighbourhood pixels into two groups separated by the reference line. Subsequently, the positive and negative signs are assigned to two members of each group. The sign identification in a vector form can be expressed as

$$s(x,y)=\begin{cases}\begin{bmatrix}-1 & 1 & 1 & -1\end{bmatrix}^T, & G_x(x,y)>0 \text{ and } G_y(x,y)>0 \\ \begin{bmatrix}1 & 1 & -1 & -1\end{bmatrix}^T, & G_x(x,y)<0 \text{ and } G_y(x,y)>0 \\ \begin{bmatrix}-1 & 1 & 1 & -1\end{bmatrix}^T, & G_x(x,y)<0 \text{ and } G_y(x,y)<0 \\ \begin{bmatrix}-1 & -1 & 1 & 1\end{bmatrix}^T, & G_x(x,y)>0 \text{ and } G_y(x,y)<0 \\ \begin{bmatrix}0 & -1 & 0 & 1\end{bmatrix}^T, & G_x(x,y)=0 \text{ and } G_y(x,y)<0 \\ \begin{bmatrix}0 & 1 & 0 & -1\end{bmatrix}^T, & G_x(x,y)=0 \text{ and } G_y(x,y)>0 \\ \begin{bmatrix}1 & 0 & -1 & 0\end{bmatrix}^T, & G_x(x,y)<0 \text{ and } G_y(x,y)=0 \\ \begin{bmatrix}-1 & 1 & 1 & 0\end{bmatrix}^T, & G_x(x,y)>0 \text{ and } G_y(x,y)=0 \end{cases} \quad (3)$$

*3) Angle differential measurement:* An angle differential measurement gives the difference in angle between pixels from different sides of the reference line. The sign of the angle differential measurement can be used as an indicator to classify that the gradient directions of four neighborhood pixels are divergent or convergent. The angle differential measurement can be expressed as
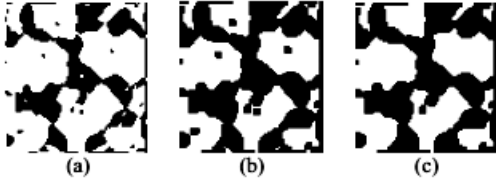
Figure 4. (a) The binary image from the pixel classification. (b)The image after erosion with 3x3 square-shaped structuring element. (c) The image after holes filling and fragmented object elimination.
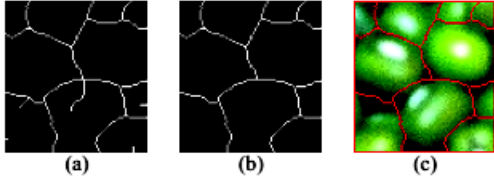


Figure 5. (a) The obtained boundary from thinning operator. (b) The boundary after de-branching. (c) The resulting boundary superimposed on the RGB image.

$$\Delta\omega(x,y,v) = \sum_{k=1}^{4}\left(s^{k}(x,y)\cdot\omega^{k}(x,y,v)\right), \qquad (4)$$

where $k$ is the index number 1, 2, 3, and 4, which is corresponding to the neighborhood pixel in north, east, south, and west directions, respectively. The obtained differential angle measurement is classified into the binary image as shown in Fig. 3. However, the error in binary image occurs when $v = x$ is used as a reference axis as shown in Fig. 3(b). The cause of this error is from the separating angle that is in the first quadrant and the fourth quadrant. When $v = -x$ is used as a reference axis, the error still occurs as shown in Fig. 3(c). This error can be corrected by adding of decision condition. The decision condition employs the different angle of both $v = x$ and $v = -x$, and then correct the out of range of $v = x$ with $v = -x$. The function can be expressed as

$$\Delta\omega(x,y) = \begin{cases} \Delta\omega(x,y,v=x), & -\pi < \omega(x,y,v=x) < \pi \\ \Delta\omega(x,y,v=-x), & \text{Otherwise} \end{cases}.$$

$$(5)$$

*4) Binarization:* The final step of pixel classification is the transformation of the obtained angle into the binary image. The threshold value needs to be defined to separate any pixel based on its angle. In this task, we can easily define the threshold value as zeros, which is formulated as

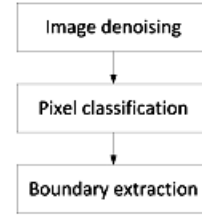$$B(x,y) = \begin{cases} 0, & \Delta\omega(x,y) < 0 \\ 1, & \text{Otherwise} \end{cases}. \qquad (6)$$



Figure 6. The workflow of the proposed algorithm.

From the example, the obtained binary image is shown in Fig. 3(d).

### B. Boundary Extraction

Components in the binary image resulting from the behavior of gradient direction consist of connected area, local minima region, local maxima region, and fragmented objects. These are considered to be noise in binary form, and must be eliminated before extracting the single pixel boundaries. The basic operator of morphology can handle this task with the selection of the proper operator for each case.

Let $B$ is the binary image from the pixel classification as shown in Fig. 4(a). We first apply an erosion operator with 3×3 square-shaped structuring element to separate the connected area. The obtained binary image shown in Fig. 4(b) illustrates the resulting individual objects and eliminated local minima area. Next, holes from local maxima region are removed with filling algorithm in binary image. Finally, the elimination of fragmented objects is operated on identifying removed area in pixel number. The obtained binary image with holes filling and fragmented object elimination is illustrated in Fig. 4(c).

Next step, the single pixel boundary can be extracted using thinning algorithm. However, in some cases, the branch boundary appears as shown in Fig. 5(a). To eliminate them, we use the trimming operator in loop operation with defined condition as procedure in [10]. The complete boundary from de-branch algorithm is shown in Fig. 5(b), and then it is superimposed on the original image to show resulting boundary in Fig. 5(c).

### III. EXPERIMENTS

### A. Materials and Methods

Fig. 6 shows the workflow of our proposed method consisting of image denoising, pixel classification, and boundary extraction. In image denoising, we utilized the anisotropic diffusion filter to hold the contrast of object boundary. Parameter $K$ and iteration number in anisotropic filter process were defined as 80 and 30, respectively. The experimental image used in this paper was captured from the green beans to demonstrate the connected objects. It was used in the evaluation of method compared with the tradition algorithm, i.e. watershed. The boundary of the experimental image containing 587 green beans was manually marked for quantitative evaluation and boundary accuracy evaluation.
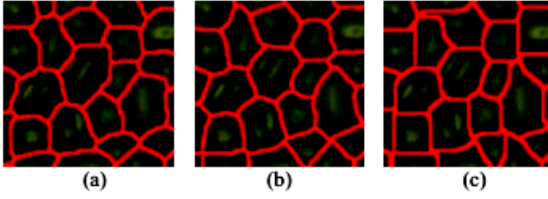
Figure 7. The resulting boundary from (a) manual marking, (b) proposed algorithm, and (c) watershed algorithm.

## B. Evaluation

In the paper, we evaluated the algorithm efficiency using the value of correct, over and under segmentation to describe quantitative performance. Another evaluation presented in this paper is boundary accuracy, which can be expressed as the difference between boundary from algorithm and manual marking. Thus, we applied the relative distance error (RDE) [10] to find distance between them. The RDE evaluation was calculated by

$$RDE = \frac{1}{2}\left( \sqrt{\frac{1}{n_e}\sum_{i=1}^{n_e} d_{e_i}^2} + \sqrt{\frac{1}{n_t}\sum_{i=1}^{n_t} d_{t_i}^2} \right), \quad (7)$$

where $d_{e_i}$ is the minimum Euclidean distance from a boundary pixel $i$ of the resulting boundary to the target boundary of the manual marking boundary, and $d_{t_i}$ is the minimum Euclidean distance from a target boundary pixel $i$ of the manual marking boundary to the resulting boundary. The RDE evaluation in this paper gave value for only one object. Thus, in the final stage, we calculated the average RDE for all objects, which have the same number of objects as the manual marking boundary, the boundary from proposed algorithm, and the boundary from watershed algorithm.

## IV. RESULTS

Table 1 shows segmentation performance of the proposed algorithm compared to the watershed algorithm. The numbers shown in the table are the number of correct segmentation, over-segmentation, and under-segmentation. With the same image from denoising method, the quantitative evaluation indicates that the proposed algorithm has the better performance in correct segmentation, and under-segmentation. However, it has less performance in over-segmentation.

Fig. 7 shows the boundary superimposed on the original image which is cropped from the large image. It illustrates the boundary from the manual marking, the proposed algorithm, and the watershed algorithm as shown in Fig. 7(a)-(c), respectively. It is shown that the boundary from the proposed algorithm is closer to the boundary from manual mark compared to that from the watershed. This observation is guaranteed by the RDE evaluation. In other words, the average

TABLE I. COMPARISON ON ACCURACY OF SEGMENTATION

| Methods | Correct | Over | Under |
|---|---|---|---|
| Proposed algorithm | 531 | 31 | 54 |
| Watershed | 526 | 27 | 58 |

RDE from the proposed algorithm and the watershed algorithm are 22.82 and 24.13, respectively.

## V. CONCLUSIONS

We introduce an algorithm for segmenting multiple connected objects using the behavior gradient direction. Preliminary results of investigation show that overlapping objects are segmented with satisfactory boundary. The resulting evaluation shows the better performance of the proposed algorithm compared to the tradition algorithm.

## ACKNOWLEDGMENT

## REFERENCES

[1] R. C. Gonzalez and R. E. Woods, Digital image processing. Upper Saddle River, NJ: Prince-Hall, 2002.

[2] J. Cheng and J. C. Rajapakse, "Segmentation of clustered nuclei with shape markers and marking function," IEEE Trans. Biomed. Eng., vol. 56, no. 3, pp. 741-748, Mar. 2009.

[3] Q. Yang and B. Parvin, "Harmonic cut and regularized centroid transform for localization of subcellular structures," IEEE Trans. Biomed. Eng., vol. 50, no. 4, pp. 469-475, Apr. 2003.

[4] O. Schmitt, M. Hasse, "Radial symmetries based decomposition of cell clusters in binary and gray level images," Pattern Recogn., vol. 41, pp. 1905-1923, 2008.

[5] X. Yang, H. Li and X. Zhou, "Nuclei segmentation using marker-controlled watershed, tracking using mean-shift, and kalman filter in time-lapse microscopy," IEEE Trans. Circuits Syst. I, Reg. Papers, vol. 53, no. 11, pp. 2405-414, Nov. 2006.

[6] K. Z. Mao, P. Zhao, and P.-H. Tan, "Supervised learning-based cell image segmentation for p53 immunohistochemistry", IEEE Trans. Biomed. Eng., vol. 53, no. 6, pp. 1153-1163, June 2006.

[7] H. Masmoudi, S. M. Hewitt, N. Petrick, K. J. Myers and M. A. Gavrielides, "Automated quantitative assessment of her-2/neu immunohistochemical expression in breast cancer," IEEE Trans. Med. Imag., vol. 28, no. 6, pp. 916-925, June 2009.

[8] X. Zhou, F. Li, J. Yan and S. Wong, "A novel cell segmentation method and cell phase identification using markov model," IEEE Trans. Inf. Technol. Biomed., vol. 13, no. 2, pp. 152-157. Mar. 2009.

[9] Y. Al-Kofahi, W. Lassoued, W. Lee, and B. Roysam, "Improved automatic detection and segmentation of cell nuclei in histopathology images," IEEE Trans. Biomed. Eng., vol. 57, no. 4, pp. 841-852, Apr. 2010.

[10] S.-F. Yang-Mao, Y.-K. Chan, and Y.-P. Chu, "Edge enhancement nucleus and cytoplast contour detector of cervical smear images," IEEE Trans. Syst., Man, Cybern. B, Cybern., vol. 38, no. 2, pp. 353-366, Apr. 2008.

**IEEJ Transactions on Electrical and Electronic Engineering, vol. 8, no. 4, 2013**

Paper

# Overlapping Nuclei Segmentation Using Direction-Based Flow Tracking

Yunyong Surut[a], Non-member
Pornchai Phukpattaranont, Non-member

In medical image processing, the segmentation of overlapping nuclei is one of the challenging topics, which relates to its application in diagnostic pathology. To achieve the quantification accuracy (ACC) of the diagnosis, we propose an overlapping nuclei segmentation algorithm using the principle of direction-based flow tracking (DBFT). The DBFT, which consists of direction field preparation and direction field tracking, is performed to provide the direction field and the labeled distinct single nucleus. Its performance is validated with 6375 nuclei from 29 images and compared with two popular overlapping objects segmentation methods, i.e., traditional watershed (TWS) and marker-controlled watershed (MCWS). While the sensitivity (SS) of the DBFT, TWS, and MCWS is 0.981, 0.990, and 0.966, respectively, and the corresponding positive predictive value (PPV) is 0.948, 0.831, and 0.910. The ACC values and $F_1$ measures obtained from the combination of SS and PPV are used as the total performance measures. While the ACC values from DBFT, TWS, and MCWS are 0.930, 0.824, and 0.882, respectively, the corresponding $F_1$ measures are 0.964, 0.904, and 0.937. The results clearly show that the DBFT is the best among three methods because it provides the maximum numbers on both ACC and $F_1$ values. © 2013 Institute of Electrical Engineers of Japan. Published by John Wiley & Sons, Inc.

## 1. Introduction

Nuclei image analysis in quantification is a key step in diagnostic pathology. By manual operation, lacking performance often makes it more time consuming, costly, and infeasible [1–3]. To alleviate these disadvantages, image analysis algorithms are introduced to handle the segmentation accuracy (ACC) for quantitative evaluation. For this task, performance of overlapping nuclei segmentation is very important because it directly affects to quantification ACC. Most of overlapping nuclei segmentation algorithms can be categorized into direction-based and intensity-based considering the provided input.

From the literature of overlapping nuclei image segmentation based on intensity application, the traditional watershed (TWS) algorithm is widely implemented for several classes of nuclei [1,2,4–12]. This traditional scheme has been developed to be used with various nuclear characteristics and alleviate over and undersegmentation that usually result from its application. Their additional improvements can be grouped into preprocessing and postprocessing by the proposed strategies. On one hand, the preprocessing attempts to prepare an accurate catchment basin provided to the flooding step of the watershed algorithm. To extract the accurate catchment basin from nuclear binary image, a marking function [2] is introduced to construct the precise dam among the catchment basins, except the distance transformation, in general [5]. Also, the direct development of distance transformation [11] and the radial symmetry decomposition technique [12] are investigated to fulfill this watershed requirement. In case the applied nuclear surface that is determined is disturbed by noise, surface reconstruction by harmonic cut and regularized centroid transform [4] also are endeavored to achieve an accurate catchment basin.

Another technique is marker-controlled watershed (MCWS) working under initial marker identification before the flooding step. This technique can restrict the oversegmentation if the marker can represent the individual nuclei. So, the next consideration is how to mark only one marker per one nucleus. Under this requirement, the minima utilizations of nuclei shape [2,5,8] are proposed as the marker generator. Also, the modified morphology procedure [7] can respond to the mentioned marker requirement. On the other hand, postprocessing deals with the over- and undersegmentation problem resulting from the watershed algorithm. The selected features of segmented nuclei are provided to the merging algorithm which determines merging decision among connected regions [6,7,10]. Moreover, hole-filling is applied to remove imperfect segmented nuclei [9].

Besides the watershed algorithm, active contour methods are also employed for carrying out overlapping nuclei segmentation [13–18]. According to its concept, based on region-based and edge-based manner [19], the segmented boundary approaches the expectation accurately. The contour deformation process is begun by the initial contour, and then the deformation is controlled by the minimization process based on internal and external forces. The modified external force field by repulsion [13,18] generates a split contour for close nuclei segmentation. Also, the coupled parametric active contour [15] solves the overlapping contours in multiple overlapping nuclei. In addition, the determination of knot of the contour [17] and the cooperation between watershed and active contour [14] are also available strategies. On the accurate segmented boundary and the uncomplicated operation from the active contour method and the watershed algorithm, we attempt to combine their advantages together for improving the segmentation ACC. To achieve this goal, our observation on the active contour method reveals that the external force field can be sufficient information to extract the individual nucleus by its direction, in which the moving contours become the movement of all nuclei pixels.

In the concept of overlapping nuclei segmentation, the pixels from an individual nucleus, which are tracked on the direction

[a] Correspondence to: Yunyong Surut. E-mail: yunyongsurut@yahoo.com

Department of Electrical Engineering, Faculty of Engineering, Prince of Songkla University, 15, Karnjanavanit Road, Hat Yai, Songkhla 90110, Thailand
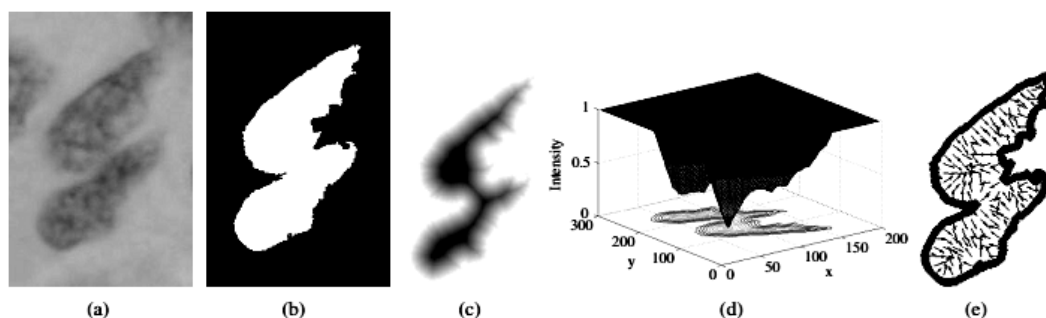
Fig. 1. Characteristics of the overlapping nuclei image. Note that all direction field images are shown using a down sampling rate of 0.2. (a) Intensity image. (b) Binary image from background elimination. (c) Complement of distance image. (d) Intensity surface plot of (c). (e) Direction field from gradient estimation

field, try to direct to the same area or nearby. Then, the individual nucleus is extracted by these grouped pixels. Based on this concept, two steps of algorithms are developed. These are the approach of direction arrangement to meet the direction field requirement, and the method of pixel tracking on the direction field. Consequently, we separate the proposed algorithms into two steps: 'direction field preparation' and 'direction field tracking'. The proposed algorithm is thoroughly described in Section 2, and its application to overlapping nuclei image is demonstrated in Section 3. With comparison to the TWS and MCWS algorithms, the interesting evaluation results are discussed in Section 4. Finally, we give conclusions in Section 5.

## 2. Direction-Based Flow Tracking Method

As mentioned earlier, our proposed algorithm for segmenting overlapping cells, which is based on the direction-based flow tracking (DBFT) method, consists of two steps, i.e., direction field preparation and direction field tracking. First, the direction field of an individual nucleus is constrained to direct to the same area or nearby. It is an important factor in the direction environment for ACC segmentation, which is similar to the preprocessing step in other segmentation algorithms. Second, the provided direction field is employed to guide a pixel moving to the destination. Therefore, the gathering of pixels is able to be labeled as the same group number, and then be extracted as the segmented boundary finally.

### 2.1. Direction field preparation
According to concave shape of overlapping nuclei, the segmentation algorithm can employ it to provide segmentation information using image transformation. As shown in the examples in Fig. 1(a)–(c), the reconstructed image intensities are sequentially extracted from the intensity image to the distance image. These distance values from the distance transformation give the minima region in each individual nucleus, and continually yield the direction field from their gradient estimation as illustrated in Fig. 1(d) and (e), respectively. This information can be provided to the watershed algorithm and active contour methods. However, in practice, based on concave shape application, the irregular nuclei shape usually makes the local minima region and continually yields confusing direction field as shown in the examples in Fig. 1(d) and (e). Certainly, the oversegmentation from its application to segmentation algorithm cannot be avoided.

In this paper, we employ the nuclei shape information to segment overlapping cells. Therefore, direction field preparation must be sufficient to handle the shape defect and maintain the direction field requirement. To achieve these goals, we propose the integration of the distance transformation, gradient direction

estimation, and basic morphology operators in an iterated process. Let $A$ be a binary image consisting of overlapping nuclei. The initial direction field is obtained by

$$\mathbf{V} = \frac{\nabla (d (A))}{\|\nabla (d (A))\|} \qquad (1)$$

where $d (.)$ is the distance transformation function, and the operator $\|\nabla (.)\|$ is the normalization of gradient that yields the direction field by normalized vector in matrix $\mathbf{V}$. Therefore, (1) represents the direction estimation from the obtained distance. However, it still provides the confusing direction from the irregular shape of overlapping nuclei as shown in the example in Fig. 1(e). To constrain $\mathbf{V}$ to support the direction requirement, two factors are needed to the direction field. These are the contrasting direction and the smoothing direction abilities. On one hand, the smoothing direction ability is the ability of direction field in the individual nuclei that can be tracked to the same area. On the other hand, the contrasting direction ability is the difference direction at the boundaries among the individual nuclei. By constraining these factors, the perfect direction field can be obtained as the example shown in Fig. 2(a).

To gain these factors, initially the smoothing direction ability can be controlled by the nuclei shape input to the distance
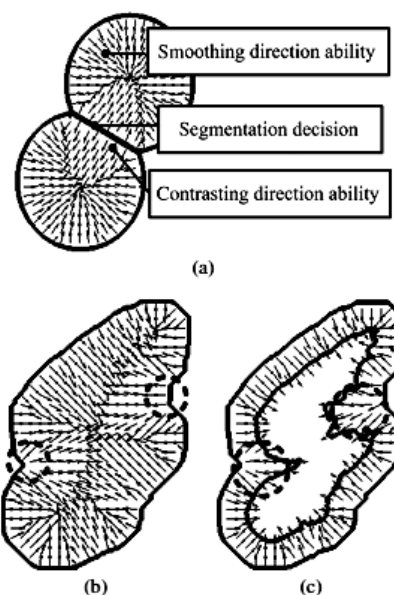


Fig. 2. Direction field preparation concept. (a) Direction field characteristics. (b) Direction field from dilation operator. (c) Local direction field from the DBFT
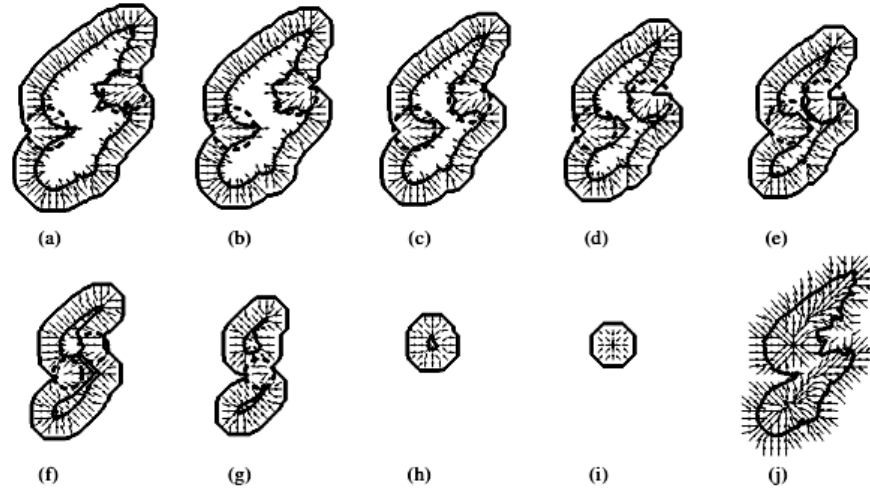
Fig. 3. (a)–(i) Illustration of the local direction field at $i = 1, 5, 10, 15, 20, 25, 30, 35, 40$. (j) The final direction field

transformation function in (1). It means that, if the irregularity of nuclei shape is reduced, the derived direction field is smoother. The simple solution as the dilation operator and the obtained direction field are used to achieve this task as shown in Fig. 2(b). By smoothing the irregular shape directly, however, the obtained direction field flows smoothly but the contrasting direction ability gets lost. To solve this problem, we modify (1), which is the global operation to local process. The concept can be seen in Fig. 2(b), in which the black dashed circles mark the remaining contrasting direction after the dilation process. This local process aims to keep both the remaining contrasting and existing smoothing directions. To succeed in this task, the co-operation of the dilation operator and the complement of $A$ is performed to produce the local direction field as shown in Fig. 2(c). Now, (1) is transformed to

$$\mathbf{V}_{local} = \frac{\nabla\left(d\left(A \oplus E_d\right)\right)}{\|\nabla\left(d\left(A \oplus E_d\right)\right)\|} \cdot \overline{A} \qquad (2)$$

where $E_d$ is a structuring element for the dilation operator, and $\frac{\nabla(d(A \oplus E_d))}{\|\nabla(d(A \oplus E_d))\|}$ is the initial direction field from the dilation operator. Because it involves a local calculation, extending it to all pixels is necessary for completing the contrasting direction among individual nuclei. The shrinking process by the erosion operator is selected to this task as an added procedure in the iterated process, which is given by the following:

**Direction field preparation:**
**Define** $E_d$, $E_{sh}$
$\mathbf{V} = 0$
$i = 0$
**While $A$ is not empty**
    **Find** $\mathbf{V}_{local}^i$
    $\mathbf{V} = \left(\mathbf{V} + \mathbf{V}_{local}^i\right)/2$
    $A = A \ominus E_{sh}$
    $i = i + 1$
**End while**
**End**

where $\mathbf{V}_{local}^i$ is a local direction field at loop $i$, and $E_{sh}$ is the structuring element of the erosion operator for the shirking process. At a loop $i$, the direction field preparation produces the local direction field, as the examples shown in Fig. 3(a)–(i). It is clearly observed that the local contrasting and smoothing directions are obtained for all results. Thus, the average of all $\mathbf{V}_{local}^i$ illustrated in Fig. 3(j) gives the desired direction field, which keeps both the smoothing and contrasting direction abilities. The example shows the extended contrasting and smoothing directions among nuclei

that are able to guide a pixel to the same area for each individual nucleus.

**2.2. Direction field tracking** The segmentation algorithm is further processed by tracking a pixel based on the direction field from the direction field preparation step. The segmentation results are obtained when the movement of a pixel tracking on an individual nucleus finishes and the group number is labeled. A tracking operator like gradient flow tracking [20] is able to assign a pixel tracking on the gradient direction while the segmented boundary is produced simultaneously. It is similar to our tracking strategy but different in the objective. In other words, our proposed direction field cannot be tracked because of contrasting direction behavior. However, based on this scheme, the modification can be done by assigning all pixels in the nuclei to be tracked. Let $\mathbf{p}$ be the position $(x, y)$ of a pixel in nuclei. The gradient flow tracking [20] is formed as

$$\mathbf{p}\prime = \mathbf{p} + \text{round}\{\mathbf{V}(\mathbf{p})\} \qquad (3)$$

where $\mathbf{V}(\mathbf{p})$ yields the direction through the normalized vector $\mathbf{V}$ at the position $\mathbf{p}$. In practice, the pixel position $\mathbf{p}$ is moved to the next position by rounding off its direction. This model moves $\mathbf{p}$ continuously if the direction field is available to track. However, from the existing direction field, the end of movement can be achieved by measuring the convergence behavior of the neighboring directions of $\mathbf{p}$. This is established by modifying (3) to the neighbor direction determination. The modification is formulated as

$$\mathbf{p}\prime = \mathbf{p} + \text{round}\{(\mathbf{V}(\mathbf{p}_N) + \mathbf{V}(\mathbf{p}_E) + \mathbf{V}(\mathbf{p}_S) + \mathbf{V}(\mathbf{p}_W))/4\} \quad (4)$$

where $\mathbf{V}\left(\mathbf{p}_{[N,E,S,W]}\right)$ represents the direction of a neighboring pixel of $\mathbf{p}$ at North, East, South, and West. In this way, the pixel $\mathbf{p}$ will be held when it moves the position that the round of average $\mathbf{V}\left(\mathbf{p}_{[N,E,S,W]}\right)$ is less than 1. In some cases, $\mathbf{V}\left(\mathbf{p}_{[N,E,S,W]}\right)$ cannot hold $\mathbf{p}$ to finish movement due to the over round of average $\mathbf{V}\left(\mathbf{p}_{[N,E,S,W]}\right)$. The loop process number $n$ is applied to terminate the repeated movement except the holding function from $\mathbf{V}\left(\mathbf{p}_{[N,E,S,W]}\right)$. Thus, this step can be processed as follows:

**Direction field tracking:**
$i = 0$
**Define** $n$
**While** *all* $(\mathbf{p} \neq \mathbf{p}\prime), i < n$
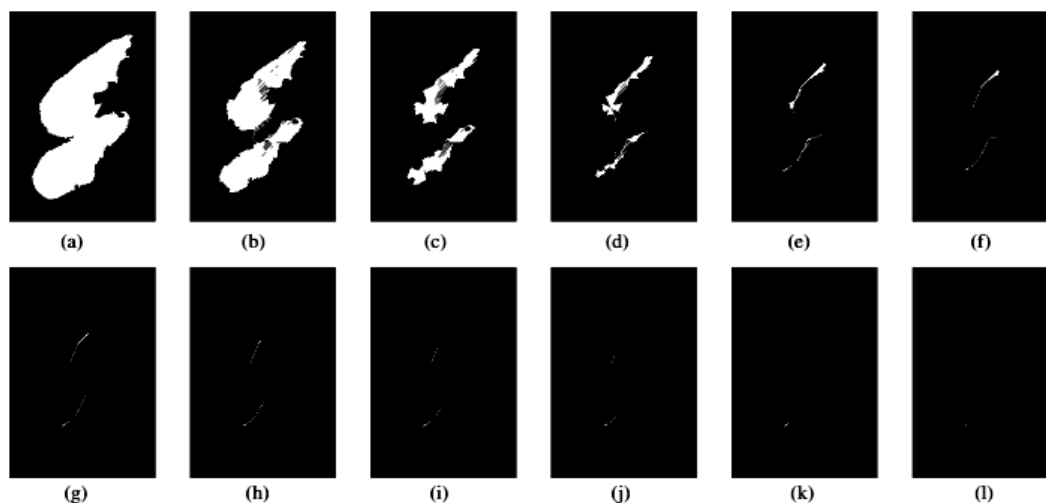    **Find $\mathbf{p}\prime$ to all pixel in nuclei**

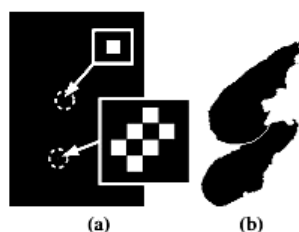Fig. 4. (a)–(j) Captured scenes of pixel tracking at $i = 1, 10, 20, 30, 40, 50, 60, 70, 80, 90, 100$, and $107$



Fig. 5. Individual nuclei extraction. (a) Pixel groups after the tracking process. (b) Separation of nuclei after retrieving pixel position



Fig. 6. Experimental workflow

**Update p**
$i = i + 1$
**End while**
**Label grouping pixel**
**Retrieve labeled pixel to original p**
**End**

Figure 4 shows the movement of pixels in the overlapping nuclei. In each iteration, the pixels flow to the destination by tracking on the direction field in Fig. 3(j). We can see that, when the number of iteration increases, grouped pixels are attracted to the area where the directions are convergent. The final scene in Fig. 4(j) indicates the finished movement where the pixels of an individual nucleus are grouped inside. Subsequently, the final step of DBFT uses these pixel groups to extract the individual nuclei. By labeling and then retrieving the grouped pixels, the labeled pixels in the white dashed circles of Fig. 5(a) are retrieved to the original position. Thus, the final results of the proposed algorithm are formed in the labeled image, which indicates the individual nucleus by the labeling number as the example shown in Fig. 5(b).

## 3. Experiments

**3.1. Materials** To validate the performance of the proposed algorithm, we applied the DBFT to the nuclei images and evaluated the quantification ACC compared to the TWS and MCWS. Their appearances obviously present a variety of shapes on both individual and overlapping nuclei. The twenty-nine images applied to this task have size $3600 \times 2880$ pixels formed in JPEG color image format.
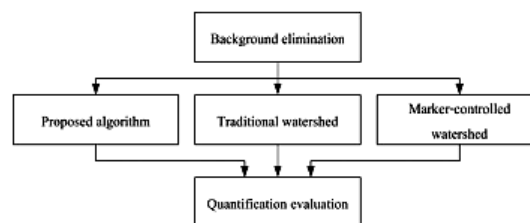
**3.2. Methods** The experimental methodology is set as the workflow shown in Fig. 6. The background elimination in the initial step is assigned to prepare the binary image to extract the nuclei area. This step uses the Otsu thresholding [21], which is performed on the intensity image from color space transformation. The tiny pieces in the obtained binary image are removed. Then, the resulting objects are performed with a hole-filling operation to complete the nuclei area. To avoid the segmentation error from the background elimination, the binary images provided to segmentation algorithms will not consider the binary nuclei which are not marked by the expert. This prevents the error of the incorrect foreground from the background elimination step.

In segmentation step, our approach initially prepares the direction field by the direction field preparation step. The operation range of the $\mathbf{V}_{local}^i$ is defined by the structuring element $E_d$, which has a disk shape. When identifying the radius parameter of the selected $E_d$, it will be a significant factor in smoothing the irregular shape and maintaining the concave shape. In this test, we approximate this parameter by varying its radius to the desired overlapping nuclei. As shown in Fig. 7, the derived direction fields are formed variously, but the smoothing and contrasting direction abilities can be observed obviously. Let $r$ be a radius parameter of the selected $E_d$, and $r = 30$ grants the direction abilities for the segmentation boundary. Thus, this obtained value will be employed throughout this experiment. In some cases, the incomplete tracking of pixels causes oversegmentation, as shown in Fig. 8(a). This error can be eliminated by the dilation operator which is applied before the labeling process. In this test, this additional operator is assigned by the structuring element of disk shape with $r = 10$. Figure 8(b) illustrates the connected tracking pixels from dilation operator, which finally yields the correctly labeled pixel.

For assessment, we choose the TWS [22] for comparing with our algorithm. Even though its oversegmentation problem mainly reduces the segmentation ACC, it is usually implemented
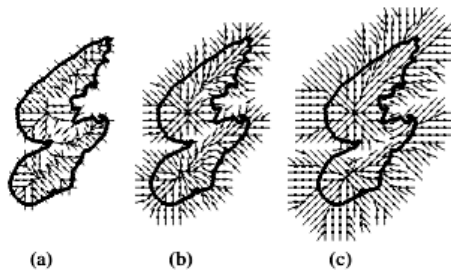
Fig. 7. Direction field from varying the radius of the disk-shaped structuring element. (a) $r = 10$. (b) $r = 30$. (c) $r = 50$



Fig. 8. Incomplete tracking pixel solution using dilation operator. (a) Incomplete tracking pixels. (b) Results from applying the dilation process

because of its simple adaptation. By preparing the catchment basin accurately, oversegmentation can be reduced. In this experiment, the Euclidean distance transformation is initially performed to build the catchment basin. Certainly, the local minima from the irregular shape of nuclei are a source of oversegmentation. To alleviate this problem, an intensity image filter is assigned to wipe out local minima before its operation. Moreover, the MCWS [23] is another selection to be compared with our approach from its advantage in oversegmentation control. Its marker identification is performed on the basis of the co-operation of morphology operators. It yields the markers, which are adopted to build the catchment basins for the watershed process.

The final step of this experiment is the quantification evaluation. This assessment yields the correct and over and undersegmentation resulting from the comparisons with the markers by an expert. In addition to the general assessment, we validate the performance of DBFT, TWS, and MCWS using sensitivity (SS) [24–28], positive predictive value (PPV) [24–28], ACC [29], and $F_1$-measure ($F_1$) [26]. These values are used to describe the performance outcome in the detection system. SS indicates the possibility that the system can correctly detect nuclei compared with the gold standard. SS calculation is given by

$$SS = TP/(TP + FN) \quad (5)$$

where TP is the number of correct segmentations by the algorithm, and FN is the number of nuclei that are not marked by the algorithm but marked by the gold standard. On the other hand, PPV is the probability that the detection of a nucleus is actually associated with a nucleus marked by the expert, which is given by

$$PPV = TP/(TP + FP) \quad (6)$$

where FP is the number of nuclei that are not marked by the gold standard but are detected in the segmented nuclei from the algorithm. Furthermore, the combination of SS and PPV yields the summarized performance evaluation where the ACC [29] and $F_1$-measure [26] are determined in the following forms:

$$ACC = \frac{TP + TN}{TP + TN + FP + FN} \quad (7)$$

and

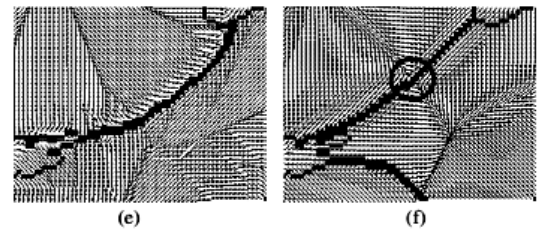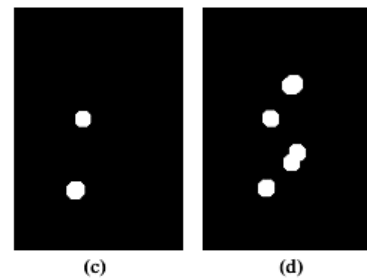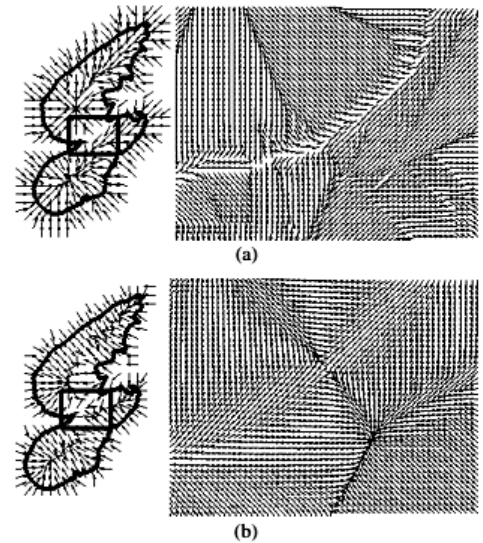$$F_1 = 2/\left(\frac{1}{PPV} + \frac{1}{SS}\right). \quad (8)$$



Fig. 9. Comparisons of direction field characteristics from the DBFT with those of the gradient direction of smoothed distance image. (a) Direction field from the DBFT technique. (b) Direction field from gradient direction of smoothed distance image. (c) Pixel groups using direction field in (a). (d) Pixel groups using direction field in (b). (e) Segmentation boundary from the tracking process of (a). (f) Segmentation boundary from the tracking process of (b)

Note that the TN is set to zero when ACC is determined.

## 4. Results and Discussion

In this section, we first describe the characteristics of the derived direction field resulting from the DBFT. The description on smoothing and contrasting direction abilities is observed from the direction fields of both the DBFT and the gradient direction of smoothed distance image. Second, the quantification ACC is presented to validate the performance of the DBFT compared to other techniques, i.e. TWS and MCWS.

**4.1. Direction characteristics** According to the direction requirement, the smoothing and contrasting direction abilities are the keys that determine the segmentation boundary. In the direction environment, both abilities are obviously observed by the direction field shown in Fig. 9. The direction field from the DBFT in Fig. 9(a) is compared with the gradient direction of smoothed

Table I. Comparison of quantification accuracy

| Image | DBFT | | | TWS | | | MCWS | | |
|---|---|---|---|---|---|---|---|---|---|
| no. | Correct | Over | Under | Correct | Over | Under | Correct | Over | Under |
| 1 | 212 | 13 | 3 | 214 | 57 | 1 | 206 | 24 | 7 |
| 2 | 236 | 16 | 4 | 240 | 55 | 3 | 236 | 23 | 6 |
| 3 | 261 | 10 | 5 | 268 | 38 | 1 | 261 | 24 | 7 |
| 4 | 240 | 10 | 9 | 243 | 67 | 6 | 232 | 17 | 17 |
| 5 | 188 | 13 | 3 | 190 | 39 | 0 | 183 | 15 | 7 |
| 6 | 262 | 11 | 2 | 263 | 32 | 2 | 258 | 12 | 6 |
| 7 | 224 | 4 | 2 | 228 | 17 | 1 | 224 | 9 | 2 |
| 8 | 225 | 7 | 3 | 228 | 33 | 2 | 225 | 12 | 4 |
| 9 | 196 | 10 | 6 | 202 | 47 | 4 | 198 | 19 | 8 |
| 10 | 284 | 15 | 8 | 288 | 50 | 5 | 280 | 22 | 13 |
| 11 | 198 | 8 | 2 | 203 | 35 | 1 | 200 | 21 | 3 |
| 12 | 237 | 12 | 3 | 240 | 33 | 2 | 235 | 20 | 6 |
| 13 | 196 | 13 | 5 | 201 | 34 | 2 | 191 | 21 | 13 |
| 14 | 231 | 11 | 2 | 232 | 44 | 1 | 229 | 20 | 4 |
| 15 | 162 | 12 | 4 | 165 | 43 | 2 | 149 | 17 | 17 |
| 16 | 204 | 13 | 6 | 207 | 45 | 3 | 196 | 25 | 11 |
| 17 | 263 | 4 | 2 | 264 | 55 | 3 | 258 | 31 | 9 |
| 18 | 260 | 10 | 15 | 280 | 64 | 3 | 267 | 27 | 12 |
| 19 | 250 | 11 | 7 | 258 | 50 | 1 | 246 | 26 | 8 |
| 20 | 175 | 25 | 1 | 174 | 59 | 1 | 170 | 26 | 6 |
| 21 | 219 | 16 | 6 | 221 | 67 | 4 | 213 | 31 | 11 |
| 22 | 158 | 4 | 7 | 162 | 20 | 6 | 154 | 12 | 9 |
| 23 | 200 | 7 | 1 | 201 | 32 | 0 | 196 | 20 | 2 |
| 24 | 168 | 12 | 3 | 173 | 21 | 0 | 166 | 17 | 5 |
| 25 | 134 | 9 | 5 | 137 | 17 | 3 | 135 | 16 | 4 |
| 26 | 239 | 6 | 2 | 239 | 38 | 2 | 240 | 9 | 1 |
| 27 | 251 | 19 | 1 | 251 | 53 | 1 | 248 | 24 | 4 |
| 28 | 224 | 11 | 2 | 226 | 66 | 1 | 223 | 26 | 3 |
| 29 | 105 | 31 | 2 | 106 | 70 | 1 | 99 | 41 | 8 |
| Sum | 6202 | 343 | 121 | 6304 | 1281 | 62 | 6118 | 607 | 213 |
| Percent | 97.29 | 5.38 | 1.90 | 98.89 | 20.09 | 0.97 | 95.97 | 9.52 | 3.34 |

distance image in Fig. 9(b) on both abilities. The decision area for the segmentation of overlapping objects is located in the rectangular box. In addition, it is zoomed out and shown in the right image.

For the smoothing direction ability, the direction field of the DBFT seems to be more confusing than the gradient direction of smoothed distance image. Nevertheless, it can be still tracked by a pixel to the area representing the individual nucleus as shown in Fig. 9(c). This means that the direction smoothness from the DBFT can maintain the tracking ability that guides all pixels in an individual nucleus to the same area or nearby. This behavior illustrates the characteristics of direction field corresponding to the definition of the proposed concept sufficiently. On the other hand, the direction field from the gradient direction of smoothed distance image cannot achieve the correct tracking as illustrated in Fig. 9(d).

In the case of the contrasting direction ability, it is important for the tracking process since the segmentation decision is initially formed by this factor. From Fig. 9(a), our approach responds to this requirement very well as can be seen by distinct divergent directions. Its contrast directions are throughout on the segmentation decision continuously. This ensures that the initial tracking process can extract the segmentation line. Figure 9(e) shows the boundary pixels after completing the segmentation on the direction field. The segmentation boundary throughout appears at the contrasting direction. Figure 9(f) shows the segmentation boundary resulting from the direction field of the gradient direction of the smoothed distance image. Although it looks similar to the DBFT, some areas yield locally convergent and divergent direction fields as shown in the black dashed circle of Fig. 9(f). This may cause the wrong tracking of pixels.

Table II. Comparison of segmentation accuracy with respect to SS (sensitivity), PPV (positive predictive value), ACC (accuracy), and $F_1$ ($F_1$-measure)

| | DBFT | TWS | MCWS |
|---|---|---|---|
| SS | 0.981 | 0.990 | 0.966 |
| PPV | 0.948 | 0.831 | 0.910 |
| ACC | 0.930 | 0.824 | 0.882 |
| $F_1$ | 0.964 | 0.904 | 0.937 |

**4.2. Quantitative evaluation** Table I shows the comparison of quantification ACC among the experimented segmentation algorithms. Twenty-nine images consisting of 6375 nuclei were tested. The nuclei number of correct, over, and undersegmentation are shown and summarized as the total number and the percent in each column. The ideal numbers for correct, over, and undersegmentation percent are 100, 0, and 0, respectively. The correct segmentation from the DBFT, TWS, and MCWS are 97.29%, 98.89%, and 95.97%, respectively. The TWS give the highest percent of correct segmentation at the expense of significant loss in oversegmentation number. In other words, the oversegmentation given by TWS is 20.09%, which is worse than the others. The result from the MCWS, which is the watershed improvement for oversegmentation problem, is 9.52%. However, the DBFT provides the best oversegmentation of 5.38%. The TWS gives the best undersegmentation at 0.97% due to its oversegmentation characteristics. The undersegmentation from the DBFT is 1.90%, which is better than that from the MCWS at 3.34%.

Table II shows more quantitative comparisons on SS, PPV, ACC, and $F_1$ values resulting from all algorithms. The DBFT has

Table III. Comparison of segmented overlapping nuclei



| No. | DBFT | TWS | MCWS |
|-----|------|-----|------|
| 1 | | | |
| 2 | | | |
| 3 | | | |

high detection performances on both SS and PPV values at 0.981 and 0.948, respectively. These values are better than those from the MCWS, which are 0.966 and 0.910, respectively. For TWS, it gives a very good SS value at 0.990 with the trade-off in low PPV value at 0.831. By the combination of SS and PPV, the ACC of DBFT is the highest at 0.930 while the ACC of MCWS and TWS are 0.882 and 0.824, respectively. Similarly, the $F_1$ value of DBFT is also highest at 0.964 compared to those from the MCWS and TWS at 0.937 and 0.904, respectively.

Table III shows the segmentation characteristics of all algorithms using the labeled objects compared to the square dots, which are marked by the expert. Image set No. 1 shows the incomplete segmentation from the MCWS. This undersegmentation is the effect of oversegmentation controlling under failed marker identification. Image set No. 2 illustrates the oversegmentation of the TWS, which is generally caused by the imperfect catchment basin generation. In addition, the segmentation results of irregular shape nuclei in the image set No. 3 represent the disturbance to both the TWS and MCWS.

For the direction application on overlapping nuclei segmentation, the proposed approach requires the direction characteristics, which are the smoothing direction ability on individual nucleus area and the contrasting direction ability on overlapping nuclei area. The quantitative results show that the percent of correct, over, and undersegmentation from the DBFT are better than those from the MCWS. Based on the ACC and $F_1$ values, the DBFT can be considered as the best among three methods because it provides the highest numbers. Moreover, the DBFT is more robust when applied to the irregularly shaped nuclei.

## 5. Conclusions

In this paper, we have proposed the utilization of direction information for segmenting overlapping nuclei. Our method provides the direction field by the direction field preparation algorithm and segments those overlapping nuclei using the direction field tracking algorithm. The performance of the proposed method is validated and compared with those of the TWS and MCWS algorithms. Results show that our approach provides very good quantification ACC. Uncomplicated implementation also is its advantage while maintaining a high ACC. By direction-based calculation, further implementation of our approach can be applied on any two-dimensional object segmentation in which the direction field is provided correspondingly.

## Acknowledgments

## References

(1) Jung C, Kim C. Segmenting clustered nuclei using h-minima transform-based marker extraction and contour parameterization. *IEEE Transactions on Biomedical Engineering* 2010; **57**(10): 2600–2604.
(2) Cheng J, Rajapakse JC. Segmentation of clustered nuclei with shape markers and marking function. *IEEE Transactions on Biomedical Engineering* 2009; **56**(3):741–748.
(3) Jung C, Kim C, Chae SW, Oh S. Unsupervised segmentation of overlapped nuclei using Bayesian classification. *IEEE Transactions on Biomedical Engineering* 2010; **57**(12):2825–2832.
(4) Yang Q, Parvin B. Harmonic cut and regularized centroid transform for localization of subcellular structures. *IEEE Transactions on Biomedical Engineering* 2003; **50**(4):469–475.
(5) Raimondo F, Gavrielides MA, Karayannopoulou G, Lyroudia K, Pitas I, Kostopoulos I. Automated evaluation of her-2/neu status in breast tissue from fluorescent in situ hybridization images. *IEEE Transactions on Image Processing* 2005; **14**(9):1288–1299.
(6) Chen X, Zhou X, Wong STC. Automated segmentation, classification, and tracking of cancer cell nuclei in time-lapse microscopy. *IEEE Transactions on Biomedical Engineering* 2006; **53**(4): 762–766.
(7) Yang X, Li H, Zhou X. Nuclei segmentation using marker-controlled watershed, tracking using mean-shift, and kalman filter in time-lapse microscopy. *IEEE Transactions on Circuits and Systems I, Regular Papers* 2006; **53**(11):2405–2414.
(8) Mao KZ, Zhao P, Tan P-H. Supervised learning-based cell image segmentation for p53 immunohistochemistry. *IEEE Transactions on Biomedical Engineering* 2006; **53**(6):1153–1163.
(9) Masmoudi H, Hewitt SM, Petrick N, Myers KJ, Gavrielides MA. Automated quantitative assessment of her-2/neu immunohistochemical expression in breast cancer. *IEEE Transactions of Medical Imaging* 2009; **28**(6):916–925.
(10) Zhou X, Li F, Yan J, Wong STC. A novel cell segmentation method and cell phase identification using markov model. *IEEE Transactions on Information Technology in Biomedicine* 2009; **13**(2):152–157.
(11) Svensson S. Aspects on the reverse fuzzy distance transform. *Pattern Recognition Letters.* 2008; **29**:888–896.
(12) Schmitta O, Hasseb M. Radial symmetries based decomposition of cell clusters in binary and gray level images. *Pattern Recognition* 2008; **41**:1905–1923.
(13) Zimmer C, LabruyÈre E, Meas-Yedid V, GuillØn N, Olivo-Marin J-C. Segmentation and tracking of migrating cells in videomicroscopy with parametric active contours: a tool for cell-based drug testing. *IEEE Transactions on Medical Imaging* 2002; **21**(10):1212–1221.
(14) Park J, Keller JM. Snakes on the watershed. *IEEE Transactions on Pattern Analysis and Machine Intelligence.* 2001; **23**(10):1201–1205.
(15) Zimmer C, Olivo-Marin J-C. Coupled parametric active contours. *IEEE Transactions on Pattern Analysis and Machine Intelligence* 2005; **27**(11): 1838–1842.
(16) Adiga PSU. Segmentation of volumetric tissue images using constrained active contour models. *Computer Methods and Programs in Biomedicine* 2003; **71**:91–104.
(17) Würflinger T, Stockhausen J, Meyer-Ebrecht D, Böcking A. Robust automatic coregistration, segmentation, and classification of cell nuclei in multimodal cytopathological microscopic images. *Computerized Medical Imaging and Graphics* 2004; **28**:87–98.
(18) Cai H, Xu X, Lu J, Lichtman JW, Yung SP, Wong STC. Repulsive force based snake model to segment and track neuronal axons in 3D microscopy image stacks. *Neuroimage* 2006; **32**:1608–1620.
(19) He L, Peng Z, Everding B, Wang X, Han CY, Weiss KL, Wee WG. A comparative study of deformable contour methods on medical image segmentation. *Image and Vision Computing* 2008; **26**:141–153.
(20) Li G, Liu T, Nie J, Guo L, Chen J, Zhu J, Xia W, Mara A, Holley S, Wong STC. Segmentation of touching cell nuclei using gradient flow tracking. *Journal of Microscopy* 2008; **231**:47–58.
(21) Otsu N. A threshold selection method from gray-level histograms. *IEEE Transactions on Systems, Man, and Cybernetics.* 1979; **9**(1): 62–66.
(22) Meyer F. Topographic distance and watershed lines. *Signal Processing* 1994; **38**:113–125.
(23) Phukpattaranont P, Boonyaphiphat P. Color based segmentation of nuclear stained breast cancer cell images. *ECTI Transactions on*

*Electrical Engineering, Electronics, and Communications* 2007; **5(2)**: 158–164.

(24) Schnorrenberg F, Pattichis CS, Kyriacou KC, Schizas CN. Computer-aided detection of breast cancer nuclei. *IEEE Transactions on Information Technology in Biomedicine* 1997; **1(2)**:128–140.

(25) Primkhajeepong C, Phukpattaranont P, Limsiroratana S, Boonya-phiphat P, Kayasut K. Evaluation of color based breast cancer cell image analysis. *Songklanakarin Journal of Science and Technology* 2010; **32(3)**:231–239.

(26) Fang B, Hsu W, Lee ML. On the accurate counting of tumor cells. *IEEE Transactions on NanoBioscience.* 2003; **2(2)**:94–103.

(27) Mosaliganti K, Cooper L, Sharp R, Machiraju R, Leone G, Huang K, Saltz J. Reconstruction of cellular biological structures from optical microscopy data. *IEEE Transactions on Visualization and Computer Graphics* 2008; **14(4)**:863–876.

(28) Li K, Miller ED, Chen M, Kanade T, Weiss LE, Campbell PG. Cell population tracking and lineage construction with spatiotemporal context. *Medical Image Analysis* 2008; **12**:546–566.

(29) Olson DL, Delen D. *Advanced Data Mining Techniques*. Springer-Verlag: Berlin; 2008.

**Yunyong Surut** (Non-memeber) was born in Thailand, in 1979. He received the B.Ind. and M.S. degrees from King Mongkut's University of Technology North Bangkok, Thailand, in 2003 and 2007, respectively. He is currently working toward the Ph.D. degree in electrical engineering at Prince of Songkla University, Thailand. His research interests include medical image processing for image segmentation.

**Pornchai Phukpattaranont** (Non-member) was born in Songkhla, Thailand. He received the B.E. and M.E. degrees in electrical engineering from Prince of Songkla University in 1993 and 1997, respectively, and the Ph.D. degree in electrical engineering from the University of Minnesota, USA, in 2004. He is currently an Assistant Professor of electrical engineering, Prince of Songkla University. His research interests include ultrasound contrast imaging, ultrasound signal processing, medical image processing, and biomedical signal processing. Dr Phukpattaranont is a member of the IEEE.

# VITAE

**Name**          Mr. Yunyong Surut

**Student ID**    5110130009

**Education Attainment**

| Degree | Name of Institution | Year of Graduation |
|--------|---------------------|--------------------|
| Bachelor | King Mongkut's Institute of Technology North Bangkok | 2003 |
| Master of Science | King Mongkut's Institute of Technology North Bangkok | 2007 |

**Scholarship Awards during Environment**

The program Strategic Scholarships for Frontier Research Network for the Ph.D. Program Thai Doctoral degree, the Commission on Higher Education, Thailand.

**Work − Position and Address**

Lecturer − Princess of Naradhiwas University

Rangaemaraka Rd, Bangnak Sub-district , Amphur Muang ,

Narathiwat Province , 96000 , Thailand

**List of Publication and Proceeding**

[1] Y. Surut, and P. Phukpattaranont, "Preliminary results of cell image segmentation using dynamic force estimation on a static vane," in *Proceedings of 2009 ECTI International Conference (ECTI-CON 2009)*, Pattaya, Thailand, May 7-8, 2009, vol. 2, pp. 1090-1093.

[2] Y. Surut, P. Phukpattaranont, and S. Shuangshoti, "Unsupervised background elimination for neuroblastoma microscopic images," in *The 2$^{nd}$ Biomedical Engineering International Conference (BMEiCON 2009)*, Phuket, Thailand, August 13-14, 2009, pp. 61-64.

[3] Y. Surut, and P. Phukpattaranont, "Overlapping cell image segmentation using surface splitting and surface merging algorithms," in *Proceedings of the Second APSIPA Annual Summit and Conference*, Biopolis, Singapore, December 14 – 17, 2010, pp. 662-666.

[4] Y. Surut and P. Phukpattaranont, "Preliminary results of connected object segmentation using gradient direction," in *The 2nd International Conference on Information Engineering and Computer Science*, Wuhan, China, December 25 - 26, 2010, pp. 61-64.

[5] Y. Surut and P. Phukpattaranont, "Overlapping nuclei segmentation using direction-based flow tracking," *IEEJ Transactions on Electrical and Electronic Engineering*, vol. 8, no. 4, pp. 387–394, 2013.